Ulm University
Institute of Applied Physiology
Prof. Dr. Birgit Liss

Expression analysis of mitochondrial and plasmalemmal calcium transporters in individual hypoglossal motor neurons of endstage superoxide dismutase 1 transgenic mice

Dissertation in partial fulfillment of the requirements for the degree of Doctor of Medicine at Ulm University

Tobias Mühling
*** 28.9.1985 in Schrobenhausen**

Submitted in 2016

Dean:

Prof. Dr. Thomas Wirth

First reviewer:

Prof. Dr. Birgit Liss

Second reviewer:

Prof. Dr. Albert C. Ludolph

Day of graduation:

13.7.2017

CONTENTS II

LIST OF ABBREVIATIONS IV

1 INTRODUCTION 1
1.1 Amyotrophic Lateral Sclerosis 1
1.2 Epidemiology and clinical features of ALS 2
1.3 Etiology of ALS 4
1.4 Phenomenon and proposed mechanisms of selective vulnerability of the motor system in ALS 13
1.5 Proposed mechanisms of differential vulnerability among different motor neuron populations in ALS 14
1.6 Contributors to physiological Ca^{2+} homeostasis in motor neurons 15
1.7 The $SOD1^{G93A}$ ALS mouse model 21
1.8 Altered activity-dependent $Ca2^{+}$ buffering capacity of highly vulnerable motor neurons in ALS $SOD1^{G93A}$ mice. 22
1.9 Aims of this work 24

2 MATERIALS AND METHODS 26
2.1 Instruments and software 26
2.2 Reagents and consumables 27
2.3 Buffers, master mixes and Kits 29
2.4 Primers for multiplex-nested-PCR, genotyping-PCR and RT-qPCR 31
2.5 Breeding and clinical assessment of $SOD1^{G93A}$ mice 34
2.6 Establishing a RNase free environment 34
2.7 Brain tissue preparation of $SOD1^{G93A}$ and WT mice 35
2.8 Cryosectioning and staining of murine coronal brain tissue 36
2.9 Identification of hMNs in murine brainstem cryosections 37
2.10 Contact-free UV-laser microdissection of individual hMNs of murine brainstem cryosections. 37
2.11 Reverse transcription (RT) of isolated total brainstem RNA 40
2.12 Combined cell lysis and cDNA synthesis of individual hMNs after UV-LMD 41
2.13 Precipitation of single cell cDNA for purification 41
2.14 Determination of nucleic acid concentrations 42
2.15 Analysis of RNA integrity number (RIN) 43

2.16 Nucleic acid isolation 45
2.17 Polymerase Chain Reaction (PCR) 46
2.18 qPCR Data acquisition and analysis 56

3 RESULTS 60
3.1 Standard curve generation for evaluation of suitable TaqMan assays for RT-qPCR based quantification of Ca^{2+} transporter mRNA levels in individual hMNs 60
3.2 Information on individual $SOD1^{G93A}$ and wildtype mice analyzed in this study 64
3.3 Determination of cell size of hypoglossal motor neurons in ethanol-fixed cresyl violet stain coronal brainstem sections 65
3.4 Chat and ND1 are suitable genes for normalization of UV-LMD RT-qPCR data from individual hMN from WT and $SOD1^{G93A}$ mice 68
3.5 Co-detection of GFAP in ChAT positive and GAD65/67 negative hMN from $SOD1^{G93A}$ but not from WT mice. 70

4 DISCUSSION 81
4.1 Methodological aspects 81
4.2 Implications of marker gene expression analysis 84
4.3 Quantification of mitochondrial genome copy numbers 85
4.4 Quantification of Ca^{2+} transporter genes in hMNs of $SOD1^{G93A}$ and WT mice 86
4.5 Outlook 89

5 SUMMARY 91

6 PUBLICATION BIBLIOGRAPHY 93

APPENDIX 111

ACKNOWLEDGEMENTS 117

CURRICULUM VITAE 118

List of Abbreviations

%	Percent
µM	Micromolar
AD	Alzheimer's disease
ALS	Amyotrophic lateral sclerosis
AMPA	α-Amino-3-hydroxy-5-methyl-4-isoxazolepropionic acid
ATP	Adenosine triphosphate
BHQ	Black hole quencher
C9ORF72	Hexanucleotide repeat expansion in *C9ORF72*
Ca^{2+}	Calcium-(2+)-ions
cDNA	Complementary DNA
ChAT	Choline-acetyltransferase
CNS	Central nervous system
C_t	Cycle at threshold
DAB	Diaminobenzidine
DENN	Differentially expressed in normal and neoplastic cells
DNA	Desoxyribonucleic acid
dNTP	Desoxyribonucleotide
dsDNA	Double stranded DNA
EAAT2	Excitatory amino-acid transporter 2
EMRE	Essential MCU regulator
ER	Endoplasmic reticulum
fALS	Familiar (hereditary) form of amyotrophic lateral sclerosis
FAM	Fluorescent dye, derivate of 6-carboxyfluorescein
FasL	Fas ligand
fMRI	Functional magnetic resonance imaging
FTLD	Frontotemporal lobar degeneration
FUS	Fused in sarcoma
GABA	γ-aminobutyric acid
GAD	L-glutamate-decarboxylase
GAPDH	Glyceraldehyde 3-phosphate dehydrogenase
GEF	Guanine nucleotide exchange factor

GFAP	Glial fibrillary acidic protein
GluR	Glutamate receptor
HE	Hematoxylin/eosin stain
hMN	Hypoglossal motor neuron
HSPB8	Heat shock protein beta-8
ID	Identification number
IMM	Inner mitochondrial membrane
IP3R	IP3 receptor
kDA	Kilo-dalton
LETM1	Leucine zipper EF hand-containing transmembrane protein 1
LMD	Laser microdissection
M	Molar
mCU	Mitochondrial calcium uniporter
MCU	Mitochondrial calcium uniporter (pore-forming subunit)
MCUR1	Mitochondrial calcium uniporter regulator 1
MICU1	Mitochondrial calcium uptake 1
MIQE	Minimum information for the publication of quantitative real-time PCR experiments
MN	Motor neuron
MNCX	Mitochondrial sodium-calcium exchanger
mPTP	Mitochondrial permeability transition pore
mRNA	Messenger RNA
mtDNA	Mitochondrial DNA
mV	Millivolt
NADPH	Nicotinamide adenine dinucleotide phosphate
NCX	Sodium-calcium exchanger
ND	NADH dehydrogenase
NME1	Nucleoside diphosphate kinase A
NMJ	Neuromuscular junction
NO	Nitric oxide
OMM	Outer mitochondrial membrane
OPTN	Optineurin
P	Postnatal day

PD	Parkinson's disease
PFN1	Profilin 1
PMCA	Plasma membrane calcium ATPase
qPCR	Quantitative PCR
RNA	Ribonucleic acid
ROX	Fluorescent dye, derivate of 5-carboxy-X-rhodamine
RCF	Relative centrifugal force (acceleration normalized to Earth's gravity)
RPS9	40S ribosomal protein S9
RT	Reverse transcription
RT-PCR	Reverse-transcription polymerase chain reaction
RyR	Ryanodine receptor
sALS	Sporadic (non-hereditary) form of amyotrophic laterals sclerosis
SEM	Standard error of the mean
SERCA	Sarco-endoplasmic reticulum calcium ATPase
siRNA	Small interfering ribonucleic acid
SOD1	Superoxide dismutase 1
SQSTM1	Sequestosome 1
TDP-43	43 kDA trans-activating response region DNA binding protein
TNF-alpha	Tumor necrosis factor alpha
UBQLN2	Ubiquilin 2
UCP	Uncoupling protein
UNG	Uracil-DNA glycosylase
UV	Ultraviolet
UV-LMD	Ultraviolet-laser microdissection
VCP	Valosin-containing protein
VEGF	Vascular endothelial growth factor
WT	Wildtype
Ψ_m	Mitochondrial membrane potential

1 Introduction

1.1 Amyotrophic Lateral Sclerosis

The term Amyotrophic Lateral Sclerosis (ALS) refers to the clinical picture of muscle atrophy ("a-myo-trophic" = latin for "not supporting/nourishing the muscles") and was coined by French neurologist Jean-Martin Charcot in 1869, who described clinical and pathological characteristics of ALS (Charcot and Joffroy 1869). It became well known during the 20th century, when famous US-american baseball player Lou Gehrig and physicist Stephen Hawking were affected, and recently gained wide public attention and support of the internet community through the "ice bucket challenge".

ALS is an adult-onset, progressive neurodegenerative disorder that is marked by the degeneration in particular of motor neurons in spinal cord, brain stem and motor cortex (Vucic et al. 2014). These neurons physiologically constitute the human motor system (Figure 1), enabling the initiation and control of movements by propagation of neural impulses via their transmitter acetylcholine to skeletal muscles. In the course of the disease, due to developing lack of innervation, patients gradually lose these movement abilities with considerable variations in site of onset, extent and time course (see 1.2) (Vucic et al. 2014). Most of the affected individuals die within two to four years after onset of the first symptoms, mainly due to respiratory failure and ventilation-associated recurrent pneumonia (Kiernan et al. 2011).

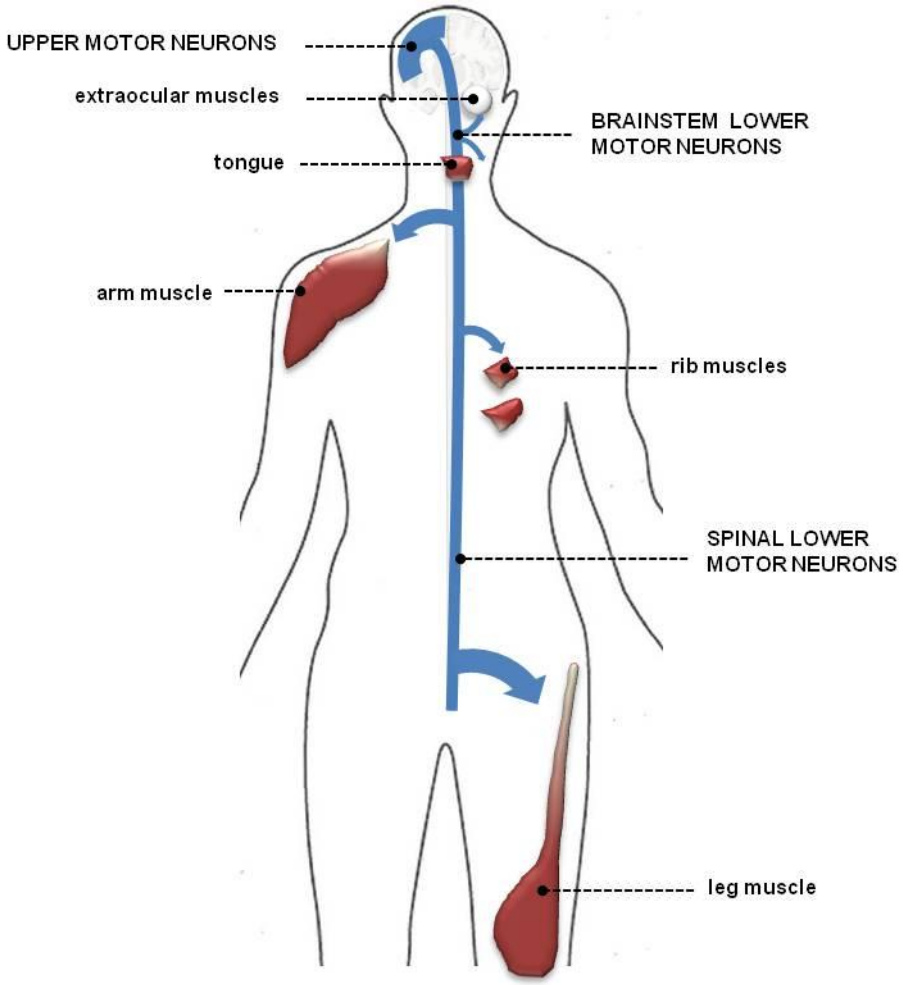

Figure 1: The human pyramidal motor system is crucial for movement initiation and control.
Motor impulses originate in the giant pyramidal cells of the precentral gyrus of the cerebral cortex (upper motor neurons). The axons of these cells descend through the brainstem and the spinal cord, where they terminate at different levels. At these sites, the bulbar and spinal lower motor neurons are located, carrying the motor impulses to the skeletal muscles.

1.2 Epidemiology and clinical features of ALS

In a systematic literature research of (Chiò et al. 2013), the authors report incidence rates for ALS that vary considerably among different countries, ranging e.g. in Europe from 0.5 to 3.6/100,000 individuals with a median of 2.08. The same analysis yielded a prevalence of 5.40/100,000 in Europe and 3.40/100,000 in North America. Thus, compared to other neurodegenerative disorders like Alzheimer's or Parkinson's disease, ALS is relatively rare. There is a family history in around 10% of ALS patients (referred to as fALS), which can be attributed to several monogenetic gene defects, while causes for neurodegeneration in most sporadic ALS (sALS) patients remain mostly unresolved. Peak age of onset for fALS is typically between 47 and 52, several years earlier than that of sALS cases, manifesting between 58 and 63

(Logroscino et al. 2010). Dependent on the degeneration pattern, clinical presentation varies, especially in the beginning: Limb-onset ALS patients (70%) show signs of upper and lower motor neuron degeneration in the limbs encompassing fasciculation, cramps, muscle weakness and atrophy as well as spasticity and pathological hyperreflexia. In contrast, bulbar-onset ALS (30%) presents mostly with speech and swallowing difficulties (Gordon 2013). Orolingual dysfunction is present as early symptom in around one third of ALS patients (Vucic et al. 2014). Regardless of the site of onset, the denervation extends progressively to adjacent muscle groups and ultimately leads to dysphagia with weight loss and malnutrition as well as respiratory compromise (Kiernan et al. 2011). Based on the *Revised El Escorial Criteria*, the clinical diagnosis is defined by progressive signs and symptoms of upper and lower motor neuron dysfunction confirmed by electromyography (Brooks et al. 2000). Detection rates for especially bulbar-onset ALS can be improved by applying the recently developed *Awaji ALS criteria*, that additionally involve neurophysiological assessment of fasciculation potentials (Noto et al. 2012). In general, limb-onset, younger age, higher motor functions and longer interval between symptom onset and diagnosis are associated with longer survival, although, due to variability of clinical presentations, it is difficult to predict survival time for an individual patient (Gordon et al. 2013).

There is an urgent need for new therapeutic agents as the exclusive approved pharmacological treatment to date is riluzole (2-amino-6-trifluoromethoxy benzothiazole). In a manner that is not yet fully understood, but possibly associated with lowering the detrimental effects of excitotoxicity (see also 1.3.2.4) and in turn increasing production of neurotrophic factors like Glial cell derived neurotrophic factor (GDNF) and Brain derived neurotrophic factor (BDNF), riluzole enhances neuronal survival (Bellingham 2011). By this means, it prolongs survival of ALS patients moderately by 3-6 months, when started after onset of disease (Vucic et al. 2014). Unfortunately, many promising results from pharmacological studies in animal models have not been translated effectively into human clinical trials (Mancuso and Navarro 2015). Progress in the use of biomarkers might provide a future opportunity for identification of responders to new agents (Bakkar et al. 2015). Moreover, markers that are measurable before symptom onset could allow earlier and more effective drug action. For example, downregulation of certain microRNAs in ALS mutation carriers occurs up to two decades before the estimated disease onset

(Freischmidt et al. 2014), potentially allowing administration of treatment before overt signs of neurodegeneration.

However, at present, besides riluzole treatment, the objective of clinicians is to maintain quality of life by multidisciplinary care, including evaluation of dietary needs, psychological assessment and therapy and, as disease advances, respiratory support and other measures of palliative care (Gordon 2013). Expert consensus guideline recommendations have been developed for these mentioned key care concerns in ALS (Miller et al. 2009).

1.3 Etiology of ALS

1.3.1 Genetic background of familial ALS and review of pathologic mutations

Although a concrete definition is lacking, in the general consensus the presence of ALS in either a first or a second degree relative of the index case constitutes the familial form of the disease (Leblond et al. 2014). A corresponding family constellation was recurrently reported over the last decades for about 10% of ALS cases. However, these estimates are questioned by a recent meta-analysis suggesting that only 4.1 to 6.1% of patients can be classified as familial (Byrne et al. 2011).

The first step in revealing the genetic background of ALS was taken in 1993, when (Rosen et al. 1993) found pathogenetic mutations of the superoxide dismutase 1 (SOD1) gene to be responsible for about 20% of familial cases (see below and 1.7). Especially in the past five years, advances in sequencing and genotyping dramatically increased the pace of gene discovery. Many authors now propose a risk-based classification for the numerous identified candidate genes where they separate causative genes with high risk for ALS from susceptibility factor genes associated with relatively low risk (Renton et al. 2013; Leblond et al. 2014). Table 1 illustrates the high risk genes carrying ALS causing mutations, of which the major candidates, *SOD1, FUS, TDP-43/TARDBP* and *C9ORF72* will be described in more detail below.

Table 1: Genes identified to carry amyotrophic lateral sclerosis (ALS) causing mutations, with their chromosomal location, inheritance, frequency among ALS patients and known function.
TARDBP/TDP-43: 43 kD trans-activating response element binding protein, *SQSTM1:* Sequestome 1, *C9ORF72*: Hexanucleotide repeat expansion in chromosome 9 open reading frame 72, *VCP*: Valosin-containing protein, *OPTN*: Optineurin, *FUS*: Fused in Sarcoma, *PFN1:* Profilin 1, *SOD1*: superoxide dismutase 1, *UBQLN2*: Ubiquilin 2. AD: autosomal dominant, AR: autosomal recessive, XD: x-linked dominant, fALS: famlilal ALS, sALS: sporadic ALS, DENN: Differentially expressed in normal and neoplastic cells (modified after Renton et al., 2013).

Gene/Protein	Location	Inherited	Percentage explained		Function
			fALS	sALS	
TARDBP/TDP-43	1p36	AD	4	1	RNA metabolism
SQSTM1	5q35	AD	1	<1	Ubiquitination; autophagy
C9ORF72	9p21	AD	40	7	DENN protein
VCP	9p13	AD	1	1	Proteasome; vesicle trafficking
OPTN	10p13	AR/AD	<1	<1	Vesicle trafficking
FUS	16p11	AD/AR	4	1	RNA metabolism
PFN1	17p13	AD	<1	<1	Cytoskeletal dynamics
SOD1	21q22	AD/AR	12	1–2	Superoxide metabolism
UBQLN2	Xp11	XD	<1	<1	Proteasome

1.3.1.1 Superoxide dismutase 1

The Cu/Zn superoxide dismutase 1 (SOD1) is a ubiquitous cytosolic enzyme detoxifying superoxide radicals (O_2-), i.e. generated in mitochondrial respiratory chain, to less oxidizing species (H_2O_2) (Rotunno and Bosco 2013). However, SOD1-mutations do not seem to initiate motor neuron degeneration by simply reducing enzyme activity (loss-of-function theory), since SOD1-Knockout mice did not display ALS-like symptoms and many of the disease causing mutations leave enzymatic activity nearly unaffected (Shibata 2001). Furthermore, wildtype SOD1 was unable to rescue motor neurons when coexpressed with mutant forms (Bruijn et al. 1998). Therefore it is widely accepted today, that pathologic effects are due to a novel neurotoxic property of mutant SOD1 (gain-of-function theory), which increases with transgene copy number. Most mutations cause structural disturbances (dimer dissociation with subsequent loss of stabilizing Zn^{2+} metal ions) resulting in misfolding and the formation of insoluble aggregates (see Figure 2), (Redler and Dokholyan 2012; Robberecht and Philips 2013). The severity of destabilization and aggregation might thus be determined by the exact localization of the mutation.

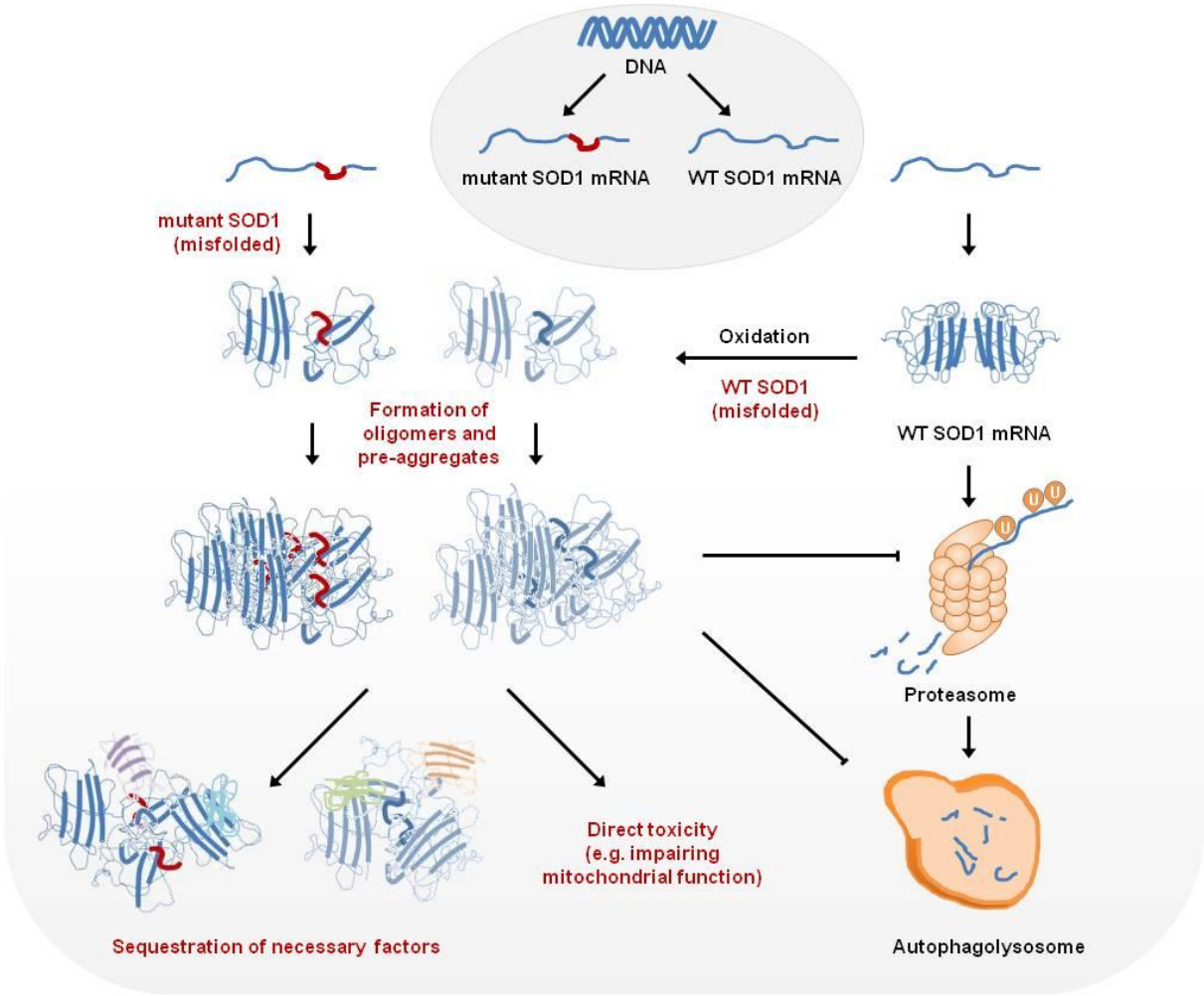

Figure 2: Proposed pathogenic mechanisms of misfolded superoxide dismutase 1 (SOD1).
Misfolded mutant or modified SOD1 escape the normal degradation machinery by proteasome and autophagy (right: illustrated for Wild-type SOD1) by formation of oligomers or aggregates and exert neurotoxic effects either directly by disturbing cellular homeostasis, e.g. mitochondrial respiration or axonal transport, or indirectly, by sequestering essential factors. For details see text. U: ubiquitin, WT: wildtype, SOD1: superoxide dismutase 1.

How these aggregates finally lead to motor neuron degeneration is still a matter of debate, although the impairment of mitochondrial function is assumed to be central. Following the observation, that mutant SOD1 localizes to the outer membrane and to the intermembrane space of mitochondria, it was shown by (Igoudjil et al. 2011), that mice overexpressing mutant human SOD1 selectively in the intermembrane space show many, but not all, ALS-like characteristics. Mutant SOD1 can affect mitochondrial function in multiple ways, including changes in motility, interfering with the apoptotic machinery (e.g. Bcl-2) and disturbing the mitochondrial electron-transport chain (for a review see (Cozzolino et al. 2013)). Interestingly, there is also a growing body of evidence suggesting that the primary site of dysfunction in ALS may not be the motor neuron itself and that mutant SOD1 exerts its detrimental effects, at

least partly, by altering the function of astrocytes (Ogawa and Furukawa 2014; Philips and Rothstein 2014).

1.3.1.2 TAR DNA-binding protein (TARDBP/TDP-43) and Fused in Sarcoma (FUS)

The 43-kDa trans-activating response region binding protein (TARDBP/TDP-43) is a nuclear protein containing both RNA/DNA and protein binding sites involved in transcription, RNA processing, RNA splicing and micro-RNA biogenesis (Lagier-Tourenne et al. 2010). TDP-43 was identified as a substantial component of ubiquitin-positive neuronal inclusions in ALS and frontotemporal lobar degeneration (FTLD) (Neumann et al. 2006) and mutations of this gene account for about 4% of fALS and 1% of sALS cases (Renton et al. 2013). This discovery strongly supported the hypothesis, that both clinical disease entities share similar pathogenetic mechanisms affecting different populations of CNS neurons. There is emerging evidence for prion-like properties of TDP-43, including template directed misfolding and seeded cell-to-cell propagation via physical contacts between nerve cells ((Braak et al. 2013)). Mutated TDP-43 is abnormally processed and sequestered to the cytosol already in early stages, suggesting, that pathogenesis is driven, at least in part, by loss of the nuclear function (Lagier-Tourenne et al. 2010). However, transient shift of TDP-43 to cytosol has been described in response to stress, so that a predominantly cytosolic localization might also represent a typical cellular response rather than a pathological event (Moisse et al. 2009).

Mutations in fused in sarcoma (FUS), another RNA/DNA binding protein, account for a limited number of ALS/FTLD cases similar to that of TDP-43 (Renton et al. 2013). A recent study identified de novo FUS mutations as a frequent genetic cause in early-onset (<35 years) ALS patients in a German cohort (Hübers et al. 2015). FUS-immunoreactive cytoplasmic inclusions with the absence of ubiquitin-positive and TDP-43-positive aggregates are the pathological hallmark of FUS ALS cases (Vance et al. 2009).

1.3.1.3 Hexanucleotide repeat expansion in C9ORF72

Responsible for about 40% of familial and 7% of sporadic ALS cases as well as 25% of familial FTLD cases, the repeat mutation in open reading frame 72 of chromosome 9 (C9ORF72) now constitutes the most common genetic cause of the ALS/FTLD spectrum (DeJesus-Hernandez et al. 2011);(Renton et al. 2011). The mutation is a prolonged hexanucleotide-repeat $(GGGGCC)_n$ in the first intron of the gene, with a median of n = 2 repeats in the general population, which is expanded in pathogenic alleles of ALS patients up to n > 1000 (DeJesus-Hernandez et al. 2011). Structural analysis of C9ORF72 unraveled strong homology to DENN (differentially expressed in normal and neoplastic cells) domain proteins, that function as guanine nucleotide exchange factors (GEF) in the regulation of membrane trafficking (Levine et al. 2013). Although the repeat expansion is localized in the non-coding region of the gene, translation might be possible via so called repeat-associated non-ATG dependent translation leading to extremely large and potentially toxic proteins (Ash et al. 2013). Another study suggests a possible role for direct toxicity of RNA, as guanine-rich sequences have a strong tendency to form stable G-quadruplexes that might sequester proteins necessary for mRNA transport but also affect telomere stability (Fratta et al. 2012).

1.3.2 Mechanisms underlying neurodegeneration in familial and sporadic ALS

The discovery of fALS-associated genes and the creation of related animal models has dramatically expanded our knowledge about the factors contributing to ALS pathogenesis although it remains difficult to establish causal relationships among them (summarized in Figure 3). Besides cell-autonomous mechanisms of MN degeneration, where intrinsic pathophysiological properties lead to cell death and consequently denervation of motor endplates ("dying forward" model) (Kiernan et al. 2011), there is increasing evidence for the participation of surrounding cells: Interestingly, transgenic mice expressing mutant SOD1 under a neuron-specific promoter were lacking an ALS phenotype (Lino et al. 2002; Pramatarova et al. 2001). In contrast, mutant SOD1 expressing astrocytes were damaging motor neurons when cocultured (Nagai et al. 2007), and disease onset was delayed upon astrocyte-selective knockdown with siRNA or in Cre-Lox systems (Boillée et al. 2006; Yamanaka et al. 2008). Recent evidence not only speaks against cell-autonomous MN degeneration but suggests a "dying back" model where denervation is preceding

cell death at least in SOD1-linked ALS: Consistent with reports of muscular defects being the primary events in ALS (Miller et al. 2006), skeletal-muscle specific expression of SOD1 in mice caused early motor deficits, followed by dismantlement of the neuromuscular junction (NMJ) and late-onset motor neuron loss (Wong and Martin 2010). These reports underline the emerging role of non-MN cells and suggest a complex cellular interplay, in which the question of cause or consequence is far from being solved.

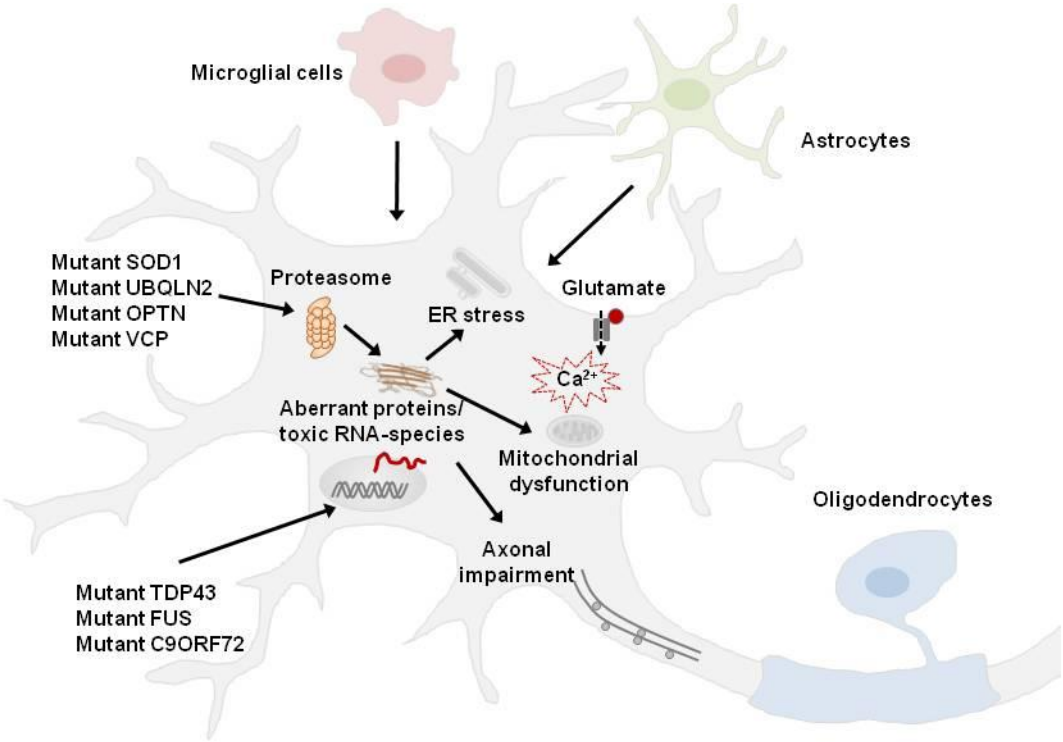

Figure 3: Overview on proposed converging pathophysiological mechanisms underlying neurodegeneration in amyotrophic lateral sclerosis.
Pathomechanisms are supposed to result from a complex interplay between molecular and genetic pathways in different cell types. Mutations in several proteins (superoxide dismutase 1 (SOD1), valosin-containing protein (VCP), ubiquilin 2 (UBQLN2), optineurin (OPTN) and, potentially, TAR DNA-binding protein 43 (TDP43) and fused in sarcoma (FUS)) cause interference with degradation and cause protein aggregation. Mutations in chromosome 9 open reading frame 72 (*C9ORF72*) and potentially *TARDBP*, which encodes TDP43, and *FUS* disrupt normal RNA metabolism. Both mechanisms favor protein aggregate formation, endoplasmic reticulum (ER) and Golgi stress as well as mitochondrial failure and disrupt axonal architecture and transport, leading to denervation of muscle cells and secondary motor neurons. Microglial cells and astrocytes might exert additional detrimental effects or lose their supportive functions. Altered calcium (Ca^{2+}) metabolism by increased glutamate concentrations in synaptic cleft and enhanced permeability of Ca^{2+} channels increases vulnerability to glutamate excitotoxicity and subsequent activation of Ca^{2+} dependent enzymatic pathways.

Pathological processes on a subcellular level comprise disturbances of most cellular compartments. Many of them also occur in other neurodegenerative disorders which raises the question whether they are secondary events or compensatory mechanisms for an initial dysfunctional trigger. The most important features that have

been consistently reported are summarized in Figure 3 and in the following paragraphs.

1.3.2.1 Protein aggregation

Progressive accumulation of protein aggregates is a leading histopathological feature of many neurodegenerative disorders, including abnormally phosphorylated tau in Alzheimer's disease (AD) (Lloret et al. 2015) and alpha-synuclein in Parkinson's disease (PD) (Barrett and Timothy Greenamyre 2015). Besides the causative role of mutated TDP-43 in ~4% of fALS cases, as discussed above, hyperphosphorylated TDP-43 was identified as the main constituent of the ubiquitinated neuronal inclusions (of so-called "skein-like" or granular appearance) shown in the vast majority of fALS/sALS cases (Neumann et al. 2006). Hyperphosphorylated TDP-43 from disease-associated tissue is less soluble than TDP-43 from normal tissue, however, inclusion formation might as well be promoted by mistakenly cleaved 25 kDa carboxy-terminal fragments of TDP-43, that are also detectable in pathological specimens (Neumann et al. 2006). Similar as described in 1.3.1.2, pathologic clearance from the nucleus might result in aberrant mRNA processing and sequestration of fundamental proteins in the cytosol. Even though cytosolic inclusions stain negative for several known binding partners of TDP-43, it is possible, that altered (e.g. hyperophosphorylated) TDP-43 disrupts cellular homeostasis through novel aberrant interactions (Neumann et al. 2007). Interestingly, while C9ORF72 ALS cases are consistently reported to be characterized by TDP-43 aggregation (Mackenzie et al. 2014), individuals with SOD1 mutations have ubiquitin-positive neuronal inclusions that are negative for TDP-43 immunoreactivity (Mackenzie et al. 2007). This finding indicates divergent pathophysiological mechanisms underlying MN degeneration for ALS linked to SOD1 mutations and raises questions about the role of SOD1 models in ALS research. Formation of SOD1 aggregates and related pathogenic events were subsumed in 1.3.1.1.

1.3.2.2 Mitochondrial dysfunction

Shortly after generation of the first SOD1-linked ALS mouse models, disorganization of mitochondrial cristae and mitochondrial vacuolization were found to appear in these mice, importantly, prior to clinical signs of motor dysfunction, suggesting an active involvement in disease pathogenesis (Dal Canto and Gurney 1994). Today,

there is ample evidence for substantial functional changes in mitochondria: Along with defective components of the mitochondrial respiratory chain and reduced ATP-synthesis that were reported through various SOD1 transgenic cell culture and animal models (Kawamata and Manfredi 2010), depolarization of the mitochondrial membrane potential (Ψ_m) was seen in isolated mitochondria of SOD1^{G93A} cell cultures (Carrì et al. 1997) and whole tissue CNS preparations of SOD1^{G93A} transgenic mice (Jaiswal and Keller 2009). These mechanisms eventually inhibit antiapoptotic (Bcl-2, Bax/Bak) or promote initiation of pro-apoptotic (activation of MPTP) pathways (Turner et al. 2013). Importantly, a recent analysis of human induced pluripotent stem cells of sporadic ALS patients yielded a large number of dysregulated mitochondrial genes, strongly implicating mitochondrial dysfunction as a key factor also in human ALS patients. The impact of mitochondrial disturbances on cytosolic calcium (Ca^{2+}) clearance will be reviewed later (1.4 and 1.6.1).

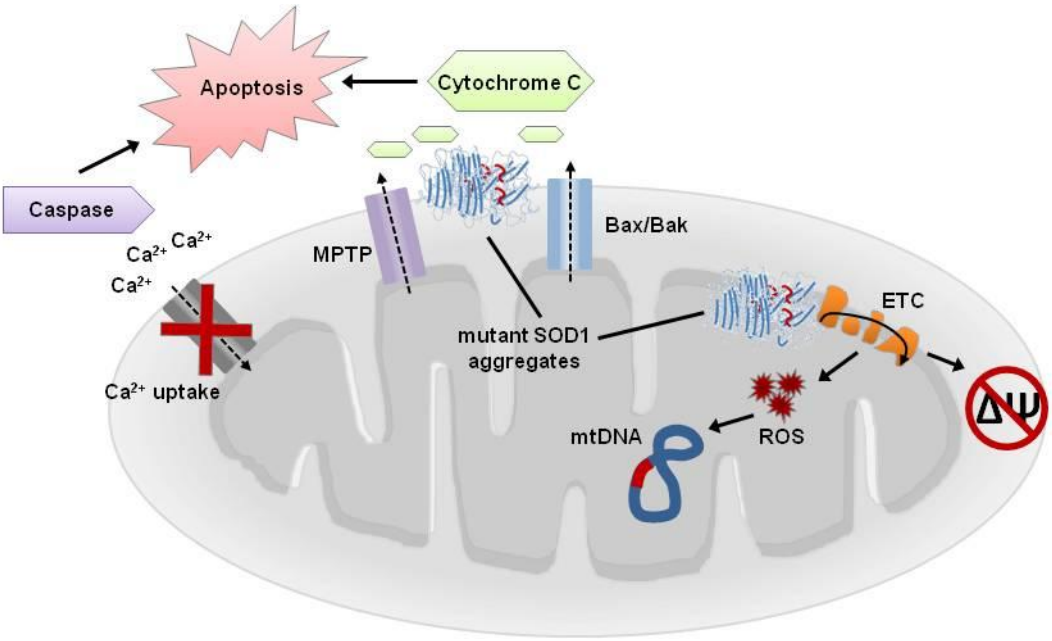

Figure 4: Amyotrophic lateral sclerosis associated mechanisms of mitochondrial dysfunction:
Mutant superoxide dismutase 1 (SOD1) aggregates at the outer membrane and intermembrane space of mitochondria, interfering with the (anti)apoptotic machinery (Bax/Bak) and the mitochondrial permeability transition pore (MPTP), resulting in the release of cytochrome c and initiation of apoptotic pathways. Impaired mitochondrial calcium (Ca^{2+}) buffering favors high cytosolic Ca^{2+} concentrations resulting in energy depletion and activation of proteases (e.g. caspases). Alterations in mitochondrial electron transport chain (ETC) increase production of reactive oxygen species (ROS), damaging nearby mitochondrial DNA (mtDNA) and proteins as well as impairing the mitochondrial membrane potential ($\Delta\Psi$). Bax: Bcl-2-associated protein, Bak: Bcl-2-homologous antagonist killer.

1.3.2.3 Increased oxidative stress

Reactive oxygen species are chemically reactive molecules containing oxygen (e.g. oxygen ions or peroxides), produced by endogenous processes, such as intracellular signaling cascades or the mitochondrial respiratory chain and, if not adequately scavanged and detoxified, can damage proteins, lipids and RNA/DNA. In ALS, free radical damage can be favored by MN-specific pathophysiological conditions, including mitochondrial damage and toxicity by excessive stimulation (excitotoxicity), and has been consistently reported in *post-mortem* tissue from patients with sALS (Kato et al. 2005; Barber and Shaw 2010). In addition, astrocytes and especially activated microglia in ALS release a host of inflammatory and proapoptotic factors that directly or indirectly aggravate oxidative stress, e.g. nitric oxide (NO), prostaglandins and programmed cell death signals such as the Fas ligand and tumor necrosis factor alpha (Zhao et al. 2004; Barber and Shaw 2010). In contrast to SOD1-linked ALS, where the mutant protein itself disrupts redox regulation of NADPH oxidase, allowing permanent production of harmful superoxide anions (Harraz et al. 2008), excitotoxic insults from microglia and astrocytes are assumed to more likely to be modifiers of disease progression rather than primary trigger events (Frank-Cannon et al. 2009).

1.3.2.4 Excitotoxiticy and calcium overload

One of the most approved theories of neurodegeneration in general and in particular of MN degeneration in ALS is that these cells, due to intrinsic properties, are more vulnerable to excitotoxic events. In this condition, excessive activation of glutamate receptors in the postsynaptic membrane leads to extensive Ca^{2+} influx. High intracellular Ca^{2+}-concentrations in turn provoke energy depletion and induce activation of proteases. Reduced transport capacity for glutamate in synaptosomes of *post-mortem* neuronal tissue of ALS patients was an early hint (Rothstein et al. 1992). Both, ALS patients and SOD1 transgenic mice show decreased levels of functional EAAT2 protein and increased circulating glutamate in the cerebrospinal fluid (Fray et al. 1998; Howland et al. 2002). Deletion of the EAAT2 gene is sufficient in spinal cord culture to induce characteristics of neurodegeneration and progressive paralysis (Rothstein et al. 1996). Ca^{2+} permeability of respective AMPA glutamate receptors in MNs is further increased by defective RNA editing of its GluR2 subunit so that elevated glutamate concentrations in the synaptic cleft can give rise to

prolonged hyperstimulation and chronic cytosolic Ca^{2+} overload (Kwak and Kawahara 2005). Cytosolic Ca^{2+} buffering proteins (like calbindin d28k or parvalbumin) are strongly diminished in vulnerable MNs (Vanselow and Keller 2000). Subsequently, excess Ca^{2+} enters mitochondria where, when rising above a certain threshold, opening of the mitochondrial permeability transition pore leads to cell death either by apoptosis or necrosis (Martin 2010). Vice versa, by increasing Ca^{2+} buffering protein levels through overexpression, vulnerable motor neurons could be protected from degeneration *in vitro* and *in vivo* (van Den Bosch et al. 2002). That the only so far approved drug for the treatment of ALS, riluzole, inhibits excitotoxic stress (among other effects, see below and 1.2) by slowing glutamate release and blocking AMPA receptors, further emphasizes the contribution of this pathogenic factor (Lamanauskas and Nistri 2008). Activity of voltage gated Ca^{2+} channels and thus presynaptic transmitter release is depressed by moderate doses (10-40 µM) of riluzole. The persistent Na^{+} current, that was reported to be increased in ALS animal models, is suppressed by low concentrations (<1-10 µM) of riluzole, which further reduces neuronal hyperexcitability (Bellingham 2011).

A link between Ca^{2+} overload and mitochondrial pathologies in ALS was drawn when several studies reported increased cytosolic Ca^{2+} transients together with significantly reduced mitochondrial Ca^{2+} uptake in cultured MNs and ALS mouse models (Grosskreutz et al. 2007; Jaiswal and Keller 2009; Coussee et al. 2011).

1.4 Phenomenon and proposed mechanisms of selective vulnerability of the motor system in ALS

Many of the common neurodegenerative disorders have their distinct "pathological footprint", meaning they particularly affect neuronal subpopulations in certain brain areas, while other neurons remain partly or totally spared. There might also be a characteristic pattern of spreading to other brain regions in the course of the disease. Identifying the molecular underpinnings of this "selective" or "differential vulnerability" can contribute to a better understanding of the disease itself and open avenues to cell-specific therapies. Explanations for the selective involvement of the motor system in ALS comprise the extraordinary size of MN cell bodies and their axons, implying high energy demands. To meet the requirements of long axonal processes,

correspondingly high expression of neurofilaments is required that might assemble abnormally in the presence of reactive oxygen species or mutated SOD1 protein (Shaw and Eggett 2000). Additionally, most (vulnerable) MN populations have low cytosolic Ca^{2+} buffering capacities, which is specified below in more detail.

It is important to note that there is also increasing recognition of clinical and pathological involvement outside the motor system, suggesting that other neurons might also be affected in course of the disease. Especially FTLD or more subtle cognitive deficits may affect patients with ALS, with ubiquitinated inclusions on dentate granule and neocortical cells (Mackenzie and Feldman 2005).

1.5 Proposed mechanisms of differential vulnerability among different motor neuron populations in ALS

Of strong clinical relevance in ALS is the sparing of eye movements and the function of external sphincters so that patients retain continence. This corresponds to histopathological findings in ALS patients and mouse models that show degeneration of vulnerable MN populations in motorcortex, spinal cord and most brainstem nuclei MNs but at the same time survival of resistant MN populations in the oculomotor, trochlear and abducens nuclei as well as Onuf's nucleus in the sacral spinal cord, which innervates external sphincters of the pelvic floor (Mannen et al. 1977; Nimchinsky et al. 2000; Haenggeli and Kato 2002). In this context, Ca^{2+} buffering capacities seem of particular relevance for defining differential vulnerability. Importantly, buffering capacities for Ca^{2+} are 5-6 times lower for vulnerable MN populations in spinal cord, hypoglossal and facial nucleus compared to resistant MNs of the oculomotor nucleus (Lewinski and Keller 2005). Enabling rapid changes in Ca^{2+} concentrations, and thereby a rapid firing pattern in functionally intact cells, these features likely add to the particular vulnerability of MNs to excitotoxic events in disease state (Lewinski and Keller 2005).

A further study using microarray analysis for examining vulnerable spinal and resistant oculomotor MNs of ALS patients reported, among other, a strongly decreased expression of most GABA receptor subunits and AMPA glutamate receptor subunit GluR2, limiting inhibitory neurotransmission and enhancing Ca^{2+} entry in vulnerable spinal MNs (Brockington et al. 2013). The growing number of

studies addressing global gene expression profiling of different MN populations in ALS has revealed a wide number of differentially expressed genes, whose significance and concrete pathophysiological contribution mostly remains to be established (also see *Discussion* section).

In the following paragraph, in view of the proposed role of Ca^{2+} homeostasis for differential vulnerability of MN neurons in ALS, that was the focus of this MD-thesis, the physiological Ca^{2+} homeostasis in motor neurons will be summarized.

1.6 Contributors to physiological Ca^{2+} homeostasis in motor neurons

Free intracellular Ca^{2+} is a highly versatile signaling molecule that contributes to a variety of characteristic neuronal features, including excitability, neurotransmitter release and gene transcription (Berridge et al. 2003). Ca^{2+} is released from internal sources (mitochondria and ER) or comes from the external medium, for example upon membrane depolarization or binding of extracellular agonists. Glutamate binding mediates Ca^{2+} entry via AMPA- and NMDA-receptor subtypes (Ionov 2007), and sets up an action potential during which Ca^{2+} enters the cell particularly via voltage-gated Ca^{2+} channels (Brini et al. 2014). Spatial and temporal dynamics of cytosolic Ca^{2+} signals are determined by Ca^{2+}-buffering proteins and uptake mechanisms into the above mentioned intracellular stores. Figure 5 illustrates the most important channel proteins involved in MN Ca^{2+} homeostasis, that are further described within the following chapters.

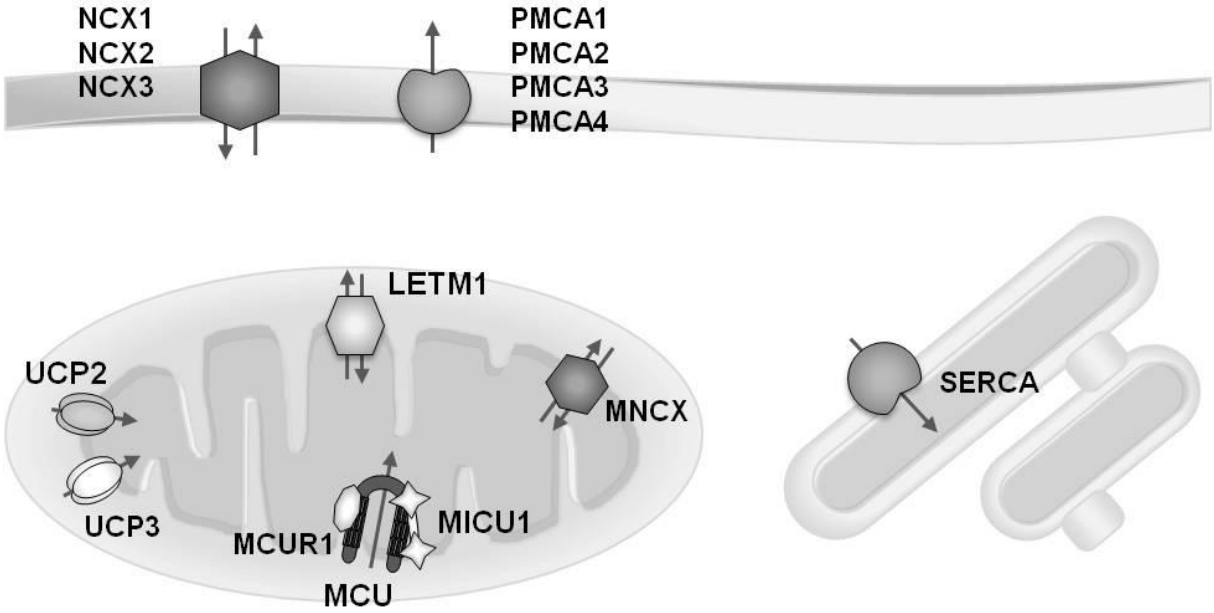

Figure 5: Illustration of calcium (Ca^{2+}) transporter proteins for plasmalemmal, mitochondrial, and endoplasmic reticulum Ca^{2+} transport in motor neurons, that shape cytosolic Ca^{2+} after entry through glutamate receptors and voltage dependent Ca^{2+} channels (not shown).
NCX: Plasmalemmal Na^{+}/Ca^{2+} exchanger, PMCA: Plasma membrane Ca^{2+} ATPase, UCP: Uncoupling protein, LETM1: Leucine zipper EF hand-containing transmembrane protein 1, MNCX: Mitochondrial sodium-Ca^{2+} exchanger, MCU: Mitochondrial Ca^{2+} uniporter, MICU1: Mitochondrial Ca^{2+} uptake 1, MCUR1: Mitochondrial Ca^{2+} uniporter regulator 1, SERCA: Sarco-endoplasmic reticulum Ca^{2+} ATPase.

1.6.1 Role and mechanism of Ca^{2+} uptake into mitochondria

Mitochondrial Ca^{2+} uptake is critical for cellular functions such as the regulation of aerobic metabolism and cell survival (Giorgi et al. 2012). The uptake of Ca^{2+} ions into the mitochondrial matrix is predominantly driven by the mitochondrial membrane potential ($\Delta\Psi$). This electrochemical gradient of about -180 mV is generated by pumping of protons through proteins of the respiratory chain towards the intermembrane space. While the outer mitochondrial membrane is generally regarded as permeable to Ca^{2+} ions (Gincel et al. 2001), a host of proteins achieves transport across the inner mitochondrial membrane (Drago et al. 2011).

1.6.1.1 The mitochondrial Ca^{2+} uniporter (mCU) and its role in MNs

The main uptake route of Ca^{2+} into mitochondria is the mitochondrial Ca^{2+} uniporter complex (mCU). Due to its low Ca^{2+} affinity, high cytosolic Ca^{2+} concentrations ($[Ca^{2+}]$) of approximately 5-10 µM are needed for a considerable mitochondrial influx via mCU (Rizzuto and Pozzan 2006). The group of Rizzuto demonstrated, that mitochondria form microdomains with the endoplasmic reticulum (ER) membrane,

where these high [Ca^{2+}] concentrations are reached (Rizzuto et al. 1998). Although functional characteristics of mCU (high selectivity and low affinity for Ca^{2+}, pharmacological inhibition by Ruthenium Red (Drago et al. 2011)) were firmly established for decades, the molecular identities of the channels remained elusive until very recently. Identification of the pore-forming constituent MCU (formerly CCDC109A) in 2011 (Baughman et al. 2011; Stefani et al. 2011; Chaudhuri et al. 2013; Tadic et al. 2014) has now forwarded the discovery of multiple regulatory molecules interacting with MCU, but reports concerning their function remain contradictory and await further clarification (Marchi and Pinton 2014). The two best-characterized regulatory subunits are mitochondrial Ca^{2+} uptake 1 (MICU1, formerly CBARA1) and mitochondrial Ca^{2+} uniporter regulator 1 (MCUR1, formerly CCDC90A). MICU1 is a 54 kDa single-pass membrane protein containing two highly conserved EF-hand Ca^{2+} binding domains and was first thought to be a positive regulator of mitochondrial Ca^{2+} entry (Perocchi et al. 2010). However, later work proposed an essential role for MICU1 as a gatekeeper, establishing a threshold that limits Ca^{2+}-entry via mCU under resting conditions to prevent mitochondrial Ca^{2+} overload and cell stress (Mallilankaraman et al. 2012b). Notably, rather than an intrinsic transporter property, this regulatory function was recently made responsible for the low Ca^{2+} affinity of the mCU complex (Foskett and Madesh 2014). How exactly MICU1 exerts its influence on mCU is still a matter of debate. Another modifier of mCU, seeming to execute the function that was originally attributed to MICU1, is MCUR1. While silencing of MCUR1 resulted in a dramatic reduction, overexpression yielded strong enhancement of mitochondrial [Ca^{2+}] (Mallilankaraman et al. 2012a). Concluding, to date, the mCU complex is regarded as the most important mitochondrial Ca^{2+} uptake mechanism and mice that lack its core component MCU show various deficits especially in situations that require a high expenditure of energy (Pan et al. 2013).

1.6.1.2 The mitochondrial Na^+/Ca^{2+} exchanger and its role in MNs

[Ca^{2+}] in mitochondria is set in the steady state by the balance of (mostly $\Delta\Psi$ driven) entry and efflux by Ca^{2+} extrusion. The mitochondrial sodium-calcium exchanger (MNCX), also known as sodium-lithium-calcium exchanger (NLCX, because it can either transport lithium or sodium in exchange for calcium), mediates Ca^{2+} efflux from the mitochondrial matrix powered by the electrochemical gradient for Na^+ entry

ubiquitously in most cell types and particularly robust in excitable tissuess (Palty et al. 2010). MNCX has considerable similarities to other members of the Na^+/Ca^{2+} or Na^+/K^+ exchanger superfamily (NCX 1-3 and NCKX 1-4), but presumably diverged earlier in evolution, explaining its unique functional properties like altered selectivity to monovalent cations (e.g. lithium) and distinct sensitivity to inhibitors (CGP-37157) (Palty et al. 2010). Approaches addressing the question of stoichiometry have so far yielded different results, favoring electrogenic exchange of 3 Na^+ ions for 1 Ca^{2+} ion over electroneutral 2:1 ratio (Boyman et al. 2013). As orientation of this passive transport mechanism is determined solely by the electrochemical gradient for Na^+ and Ca^{2+}, changes in ion concentrations or mitochondrial membrane potential (that can develop during ALS pathology) might lead to reverted operation mode of MNCX. In this situation, a failure of other Ca^{2+} uptake pathways is associated with a Na^+ dependent rise in mitochondrial [Ca^{2+}] (Kim and Matsuoka 2008). Accordingly, a reversal of MNCX was calculated for hyperpolarised $\Delta\Psi$ of -170 mV and cytosolic [Na^+] rising above 36 mM (Chinopoulos and Adam-Vizi 2010).

1.6.1.3 The mitochondrial Ca^{2+}/H^+ exchanger and its role in MNs

Leucine zipper EF hand-containing transmembrane protein 1 (LETM1) is a protein expressed through all mammalian tissues, residing at the inner mitochondrial membrane via one predicted transmembrane domain and was originally regarded as K^+/H^+ antiporter (Nowikovsky et al. 2004). This assumption was supported by the finding that LETM1 knockout could be rescued by addition of the H^+/K^+ ionophore nigericin (Dimmer et al. 2008). In 2009, a RNA knockdown screening and subsequent liposomal reconstitution found LETM1 to be the putative mitochondrial Ca^{2+}/H^+ exchanger (Jiang et al. 2009) and its knockdown reduced mitochondrial Ca^{2+} uptake and ATP generation (Jiang et al. 2013). Its role was later rendered more precisely to be a high-affinity but small-capacity uptake mode mainly for Ca^{2+} entering via plasma membrane (Waldeck-Weiermair et al. 2011), mediating electroneutral 1 Ca^{2+} / 2 H^+ antiport (Tsai et al. 2014). However, the role of LETM1 in mitochondrial Ca^{2+} homeostasis is questioned by some authors, arguing that a protein with only one transmembrane domain is unlikely to directly mediate ion transport and that the proposed stoichometry of 1:2 implies an electroneutral Ca^{2+} uptake that depends on the proton gradient. It is further argued, that such a mechanism - given the alkaline inside pH difference - cannot mediate Ca^{2+} uptake

unless cytosolic concentrations are more than 100 fold higher than mitochondrial matrix [Ca^{2+}] (Drago et al. 2011; Nowikovsky et al. 2012).

1.6.1.4 The mitochondrial uncoupling proteins UCP 2 & 3 and their role in MNs

The group of Wolfgang Graier implicated the isoforms 2 and 3 of the uncoupling proteins (UCPs) in the mitochondrial Ca^{2+} uptake machinery: First reported to be a component of the uniporter itself (Trenker et al. 2007), UCP 2 and 3 were later supposed by this group to operate independently of other Ca^{2+} uptake pathways, especially at high cytosolic Ca^{2+} concentrations of ER-derived intracellular Ca^{2+} release (Waldeck-Weiermair et al. 2011), but these data await further confirmation by other groups. Especially UCP3 was suggested by that group to account for different sensitivities corresponding to different Ca^{2+} uptake kinetics that were postulated earlier (Waldeck-Weiermair et al. 2010). In addition, UCPs act as sensors of mitochondrial oxidative stress and decrease the amount of reactive oxygen species produced by the respiratory chain via mild uncoupling (Donadelli et al. 2014).

1.6.2 Role and mechanism of Ca^{2+} uptake into the endoplasmic reticulum

The endoplasmic reticulum (ER) is a functionally diverse organelle encompassing protein synthesis, which is accomplished in the rough ER, and acting as a dynamic Ca^{2+} store due to concerted activity of ER-localized Ca^{2+} channels, transporters and intraluminal buffering proteins. While Ca^{2+} efflux from the ER is executed by two families of receptor-related channels, namely ryanodine receptors (RyR 1-3) and IP_3 receptors (IP_3R 1-3) (Amador et al. 2013), import into ER lumen is achieved by Ca^{2+} pumps of the sarco-endoplasmic reticulum Ca^{2+} ATPase (SERCA) family (Verkhratsky 2005). The isoform that is dominant in neuronal tissues, SERCA2b, exhibits the highest Ca^{2+} affinity and is tightly regulated by the Ca^{2+} binding protein calreticulin, that senses the actual level of luminal [Ca^{2+}] and activates Ca^{2+} pumping when detecting a decrease (Vangheluwe et al. 2005) All SERCA pumps can be blocked pharmacologically by nanomolar concentrations of thapsigargin, resulting in a relatively slow emptying of ER Ca^{2+} (Lytton et al. 1991).

1.6.3 Role and mechanism of Ca^{2+} extrusion via the plasma membrane

1.6.3.1 The plasmalemmal Na^+/Ca^{2+} exchanger and its role in MNs

One way to extrude Ca^{2+} across the plasma membrane is the use of the electrochemical gradient for Na^+ as a driving force. In this way, the plasmalemmal sodium-calcium exchanger family isoforms (NCX 1-3) couple the export of one Ca^{2+} ion with import of three Na^+ ions. While NCX 1 is universally distributed throughout mammalian tissues, NCX 2 and 3 have been found mainly in the brain and skeletal muscle (Philipson and Nicoll 2000). Although expression pattern and regulatory conditions vary, the Na^+/Ca^{2+} exchange system can generally be regarded as "low-affinity-high-capacity" system that can rapidly respond to transient changes in cytosolic [Ca^{2+}] (Khananshvili 2013). Allosteric activation of NCX by Ca^{2+} ions via Ca^{2+} binding regulatory domains is of particular importance for maintaining excitability of neuronal cells (Hilge et al. 2006). Concordantly, reduced expression or activity of NCX can aggravate neuronal damage under various pathophysiological conditions including cerebral ischemia (Molinaro et al. 2008). Although a great deal of interest has been devoted to this issue, pharmacologic targeting of NCX variants is still unavailable (Khananshvili 2013).

1.6.3.2 Plasma membrane Ca^{2+} ATPase and its role in MNs

Operating in a concentration range, in which the low affinity NCX system is relatively inefficient, high affinity (1 µM, see below) plasma membrane Ca^{2+} ATPases can be regarded as fine tuners of cytosolic Ca^{2+} levels (Brini and Carafoli 2011). PMCAs hydrolyze one molecule of ATP to extrude one Ca^{2+} ion, while a to date unknown number of H^+ ions enters the cell in return. A variety of agents can modulate Ca^{2+} affinity of PMCAs, the most important of them calmodulin, which can decrease the dissociation constant K_d from 10-20 µM to less than 1 µM by freeing the pump from autoinhibition (Brini and Carafoli 2009). However, unlike for SERCA Ca^{2+} pumps, no specific pharmacologic inhibitor exists for PMCAs. Similar to NCX, the PMCA isoforms show a tissue-specific expression pattern. PMCA 1 and 4 are ubiquitously expressed although isoform 1 is attributed a housekeeping role and isoform 4 is endowed with more tissue-related functions. PMCA 2 and 3 are tissue-restricted with high levels of expression in brain, striated muscles and the mammary gland (Brini

and Carafoli 2011). Accordingly, a PMCA 2 knockout mouse showed abnormalities in cerebellar Purkinje cells and spinal cord motor neurons (Kurnellas et al. 2005).

1.7 The SOD1^{G93A} ALS mouse model

Mutant SOD1 transgenic mice recapitulate most features of ALS including neuromuscular dysfunction, gliosis and motor neuron loss with phenotypes varying according to mutation and transgene expression level (Turner and Talbot 2008). In this MD-thesis, the SOD1^{G93A} ALS mouse model was analyzed. SOD1^{G93A} mice express (besides one copy of the wildtype murine SOD1) approximately 20-24 copies of human mutant SOD1 coding sequence with a glycine to alanine mutation at position 93 (SOD1^{G93A}), thus are heterozygous for the human mutant allele (Gurney et al. 1994). These mice develop hindlimb tremor and weakness around 3 months progressing to hyper-reflexia, paralysis and premature death after 4 months (Gurney et al. 1994). Proximal axonal loss is prominent by 80 days and at 100 days, ~50% of lower MNs are lost (Fischer et al. 2004). In addition, age-dependent changes in motor brain stem nuclei (including the hypoglossal nucleus that innervates and controls tongue movements) were demonstrated in fMRI to begin around day 90 (Angenstein et al. 2004) paralleled by a MN loss of 12% in 90-day-old mice and ~30% at disease endstage (between postnatal day 115 and 145) (Haenggeli and Kato 2002). A recent stereological analysis of choline-acetyltransferase (ChAT, key enzyme for production of acetylcholine) positive, immunostained hMNs yielded an average MN loss of 40% in endstage SOD1^{G93A} transgenic mice (Ferrucci et al. 2010). Importantly, the characteristics of differential vulnerability of MNs (see 1.4) remain preserved in this ALS mouse model, as e.g. the nuclei involved in eye movement are spared from degeneration (Haenggeli and Kato 2002). Due to limited translational success of SOD1 models and new insights in the genetical underpinnings of ALS, much effort has been put into the development of animal models based on different genetic background, of which the most important are discussed in 4.1.1. However up to now, SOD1^{G93A} mice are still the most widely used ALS model system.

1.8 Altered activity-dependent $Ca2^{+}$ buffering capacity of highly vulnerable motor neurons in ALS $SOD1^{G93A}$ mice.

Fuchs et al. used electrophysiology and Ca^{2+} imaging to compare highly vulnerable hypoglossal MNs and resistant oculomotor MNs *in vitro* in brainstem slice-preparations of presymptomatic or endstage $SOD1^{G93A}$ transgenic mice and controls (Fuchs et al. 2013). Notably, upon electrical stimulation to maximal firing frequency, hMNs of $SOD1^{G93A}$ mice showed impaired Ca^{2+} clearance at challenge to high firing frequencies (compared to oMN, Figure 6B) which was attributable to a mitochondrial Ca^{2+} uptake deficit selectively in these vulnerable hMNs at disease endstage (Figure 6C, left). By use of specific pharmacology (20 µM Ru360), the mitochondrial Ca^{2+} uptake deficit was most likely attributed to a reduced capacity of mitochondrial Ca^{2+} uniporter (mCU, not shown), the most important uptake route for Ca^{2+} into mitochondria (see 1.6.1.1). This deficit was accompanied by a (compensatory) increase in plasmalemmal Ca^{2+} extrusion, that was indirectly demonstrated by blocking both, mitochondrial and ER Ca^{2+} uptake (with 200 nM FCCP and 1 µM thapsigargin, respectively; Figure 6C, right) (Fuchs et al. 2013).

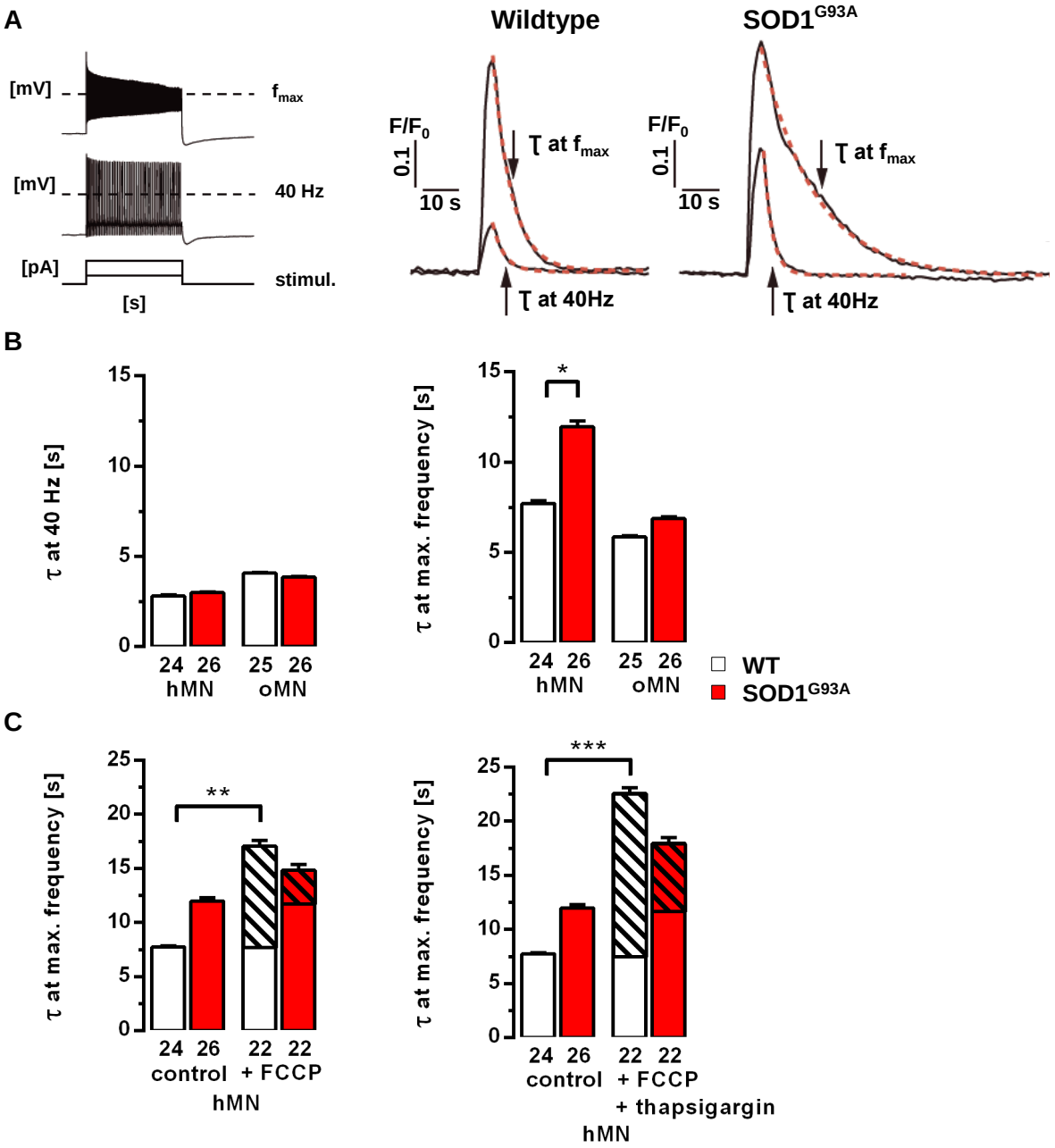

Figure 6: Hypoglossal motor neurons (hMNs) from endstage SOD1^{G93A} mice display activity dependent reduced cytosolic calcium (Ca^{2+}) clearance due to impaired mitochondrial Ca^{2+} buffering capacity.

(A) Left: electophysiological stimulation protocol and whole cell current clamp recordings of respective activity pattern in combined fura-2 Ca^{2+} imaging experiments. Stimulation in increasing current steps (2 s) evoked repetitive firing. Dashed lines = 0 mV. Right: Representative traces show ratiometric (fluorescence in relation to its baseline value, F/F_0) fura-2 Ca^{2+} signal of hMN in *in vitro* coronal brainstem slices after stimulation to 40 Hz or maximum firing frequency (f_{max}) for WT and SOD1^{G93A} mice. Signal decay was mono-exponentially fitted (1/e, red dashed line) to determine time constant Tau (τ, indicated by arrows). Note the slower decay in endstage SOD1^{G93A} at f_{max}. Representative traces were kindly provided by A. Fuchs.

(B) Shown are values for the respective time constant *τ,* given in seconds, in vulnerable hMNs and resistant oculomotor neurons (oMNs) of endstage (~P120) SOD1^{G93A} transgenic mice after stimulation to 40 Hz (left) and maximum firing frequency (right). While Ca^{2+} clearance at 40 Hz frequency did not show a difference neither in vulnerable, nor in resistant motor neurons, mean Ca^{2+} signal time constant *τ* at maximum frequency show significantly impaired Ca^{2+} clearance selectively in hMNs of endstage SOD1^{G93A} mice.

(C) Shown are values for respective time constant *τ,* given in seconds, in vulnerable hMNs undergoing selective pharmacologic inhibition of mitochondrial (left) and mitochondrial and endoplasmic reticulum (ER, right) Ca^{2+} clearance by the addition of carbonyl cyanide-*4*-(trifluoromethoxy) phenylhydrazone (FCCP) and FCCP as well as thapsigargin, respectively. In presence of the mitochondrial uncoupler FCCP (200 nM, left), no significant difference in Ca^{2+} clearance after mitochondrial uncoupling (indicated by diagonally striped boxes) is seen in endstage SOD1^{G93A} hMNs (in contrast to WT), which indicates reduced mitochondrial Ca^{2+} uptake of diseased hMNs. Endstage SOD1^{G93A} hMNs are less affected by blocking of both mitochondrial and ER Ca^{2+} uptake (with 200 nM FCCP and 1 µM thapsigargin, respectively) than WT controls (indicated by diagonally striped boxes), indicating a bigger transport capacity of Ca^{2+} across the plasma membrane.

Statistical significance as indicated. Bar graphs represent mean±standard error of the mean (SEM). WT: wildtype.

These functional data strongly suggest an activity-dependent cytosolic Ca^{2+} clearance defict, selectively in highly vulnerable hMN, due to altered mitochondrial and plasmalemma Ca^{2+} uptake/extrusion. However, the underlying molecular mechanisms are still lacking. Functional studies for dissection of these mechanisms e.g. of plasma membrane Ca^{2+} transporters (PMCAs/NCXs) or newly identified mitochondrial Ca^{2+} transporters (MCU, MICU1, MCUR1) are hampered by the lack of specific pharmacology. Consequently, in this MD-thesis, I have addressed the underlying molecular mechanisms of this functional phenotype in hMN of endstage $SOD1^{G93A}$ mice by cell-specific quantification of mRNA-levels of the respective candidate genes (mitochondrial and plasmalemmal Ca^{2+} transporters as described above), by combining UV-laser microdissection (UV-LMD) and quantitative reverse transcriptase polymerase chain reaction (RT-qPCR) techniques, as specified below.

1.9 Aims of this work

The overall aim of my medical doctoral project was to address the molecular mechanisms underlying the described functional, activity-dependent, Ca^{2+} clearance deficit in highly vulnerable hMN from endstage $SOD1^{G93A}$ ALS mice by analyzing the expression levels of respective candidate genes via UV-laser microdissection (UV-LMD) and reverse transcriptase quantitative polymerase chain reaction (RT-qPCR). Additionally, the validity of the obtained dataset should be maximized by accounting for the natural variations in cell size and number of mitochondria, respectively. For this purpose, the following strategy was chosen:

(1) Transfer the in our group well-established protocol for UV-laser microdissection and quantitative RT-PCR of individual neurons from mouse midbrain sections to a respective mouse brainstem preparation and hypoglossal motor neurons from adult WT and $SOD1^{G93A}$ mice

(2) Design, test and optimize suitable qPCR assays for reliable RT-qPCR based quantification of the following Ca^{2+} transporter genes and respective marker genes: MCU, MICU1, MCUR1, MNCX, LETM1, UCP2-3 (mitochondrial Ca^{2+} transporters), PMCA1-4, NCX1-3 (plasmalemmal Ca^{2+} transporters), ChAT, GFAP, ND1 (marker genes).

(3) Address and empirically identify suitable normalization strategies for stratification of UV-LMD RT-qPCR data derived from individual mouse hypoglossal motor neurons. The following normalization strategies were chosen to verify:

a) Normalization of RT-qPCR data for plasma membrane Ca^{2+} transporters to those of ChAT levels, as ChAT is the key enzyme of acetylcholine synthesis and as such highly abundant in MNs, but not in surrounding (neuronal) cells.

b) Normalization of RT-qPCR data for mitochondrial Ca^{2+} transporters to number of mitochondria represented by expression levels of the mitochondrially encoded ND1 gene.

c) Normalization of all RT-qPCR data to cell sizes of the respective UV-LMD sample to account for variations in cell size.

(4) Comparing mitochondrial and plasmalemmal Ca^{2+} transporter mRNA expression in individual hypoglossal motor neurons of endstage $SOD1^{G93A}$ and wildtype control mice, with and without normalization.

2 Materials and Methods

2.1 Instruments and software

The used technical equipment is listed in Table 2.

Table 2: List of used instruments and technical equipment.

Instrument	Manufacturer
-20°C Freezer	Liebherr, Biberach, GER
-80°C-Freezer	NationalLabs, Mölln, GER
Accuracy weighing machine CPA 124S	Sartorius, Goettingen, GER
Bioanalyzer 2100	Agilent, Böblingen, GER
CanonPowerShot G5 Digital Camera	Canon, Ōta, Tokyo, JP
Centrifuge 5804R	Eppendorf, Hamburg, GER
Centrifuge 5415R	Eppendorf, Hamburg, GER
Chip-Vortexer	Agilent, Böblingen/Waldbronn, GER
Galaxy Mini Centrifuge	VWR, West Chester, US
Gel documentation system BioDoc II	Biometra, Jena, GER
Gel electrophoresis chamber	University Workshop, Ulm, GER
GeneAmp 7900HT PCR System (quantitative PCR)	Applied Biosystems, Foster City, US
GeneAmp 9700 PCR System (qualitative PCR)	Applied Biosystems, Foster City, US
Leica DM 6500 Microscope	Leica, Wetzlar, GER
Leica LMD 7000 (Laser-Microdissection Setup)	Leica, Wetzlar, GER
Microtome Cryostat CM1850	Leica, Wetzlar, GER
Microwave Family I	Privileg, Munich, GER
MiniSpin Plus	Eppendorf, Hamburg, GER
Oven for heat sterilization MINO/50/F	Genlab, Widnes, UK
Picodrop Photometer	Biozym, Hessisch Oldendorf, GER
Pipet-Boy Pipetus	Hirschmann, Eberstadt, GER
Pipettes	Eppendorf, Hamburg, GER Gilson, Middleton, US
Power Supply for Gel Electrophoresis	Biometra, Jena, GER
Razor blade	Carl Roth, Karlsruhe, GER
Sterile bench with UV-C light source	Heraeus, Hanau, GER
Surgical Instruments (scissors and forceps)	Fine Science Tools, Heidelberg, GER
Techfreeze, -20°C compact incubator	Techne, Jahnsdorf, GER
Thermomixer comfort	Eppendorf, Hamburg, GER
ThermoStat	Eppendorf, Hamburg, GER
Tube-Strip Picofuge	Agilent, Böblingen/Waldbronn, GER
Vortex-Genie II	Scientific Industries, New York, US
Vortex mixer for Nano-Chips	Agilent, Böblingen, GER

A list of the used software is given in Table 3.

Table 3: List of used software.

Software	Purpose	Manufacturer
2100 Expert Software	Determination of RNA-quality	Agilent Böblingen/ Waldbronn, GER
BioDocII Analyze	Visualization of agarose gels	Biometra, Göttingen, GER
GraphPad Prism	Statistical analysis	GraphPad Software, San Diego, US
IM500	Archiving of images, LMD	Leica Microsystems, Wetzlar, GER
LMD7000	UV-Laser-Microdissection	Leica Microsystems, Wetzlar, GER
Microsoft Office 2010	Analysis, Statistics	Microsoft, Redmont, US
Microsoft Windows 7	PC Operating System	Microsoft, Redmont, US
Oligo6	Primer design	Molecular Biology Insights Inc., Colorado Springs, US
Picodrop Software	Determination of nucleic acid concentrations	Biozym, Hessisch Oldendorf, GER
SDS2.3	Realtime qPCR	Applied Biosystems, Foster City, US

2.2 Reagents and consumables

All chemicals and laboratory consumables were acquired RNase-free if available and are given in Table 4 and Table 5.

Table 4: List of used reagents and stock concentrations.

Reagent	Manufacturer
2-Mercaptoethanol	Sigma, Munich, GER
5x First-Strand-Buffer	Invitrogen, Carlsbad, US
Agarose	Lonza, Basel, Switzerland
Cresyl violet acetate powder	Sigma, Munich, GER
DEPC (diethylpyrocarbonate) stock [100%]	Sigma, Munich, GER
DNA off	MP Biomedicals, Santa Ana, US
dNTPs [20 mM, each]	GE Healthcare, Freiburg, GER
DTT [100 µM]	Invitrogen, Carlsbad, US
Ethanol absolute	Sigma, Munich, GER
Ethanol, anhydrous, denatured, HPLC Grade, 90%, 5% methanol, 5% isopropanol	Alfa Aesar, Karlsruhe, GER
Ethidium Bromide solution [10mg/ml]	Sigma, Munich, GER
GeneRuler™ 100bp DNA Ladder [0.5 µg/µl]	Fermentas, St.Leon-Rot, GER
Glycogen [5mg/ml]	Ambion, Huntingdon, UK
HCl [37%]	VWR, Radnor, US
Isoflurane [100%]	Abbott, Wiesbaden, GER
Isopropanol [99%]	Sigma, Munich, GER
Loading Dye Solution [6x]	Fermentas, St.Leon-Rot, GER
Molecular sieve, 0.3 nm, perlform	Merck, Darmstadt, GER
Nonidet P40 (NP40) 10% aqueous solution	Roche, Mannheim, GER
PCR Rxn Buffer [10x]	Invitrogen, Carlsbad, US
Polydesoxycytidine (PolydC)	Midland, Texas, US
Polyinosine (PolyI)	Sigma, Munich, GER
Primers for Genotyping (SOD wt/tg)	Metabion, Planegg, GER
Proteinase K recombinant, PCR grade solution [10mg/ml]	Roche, Mannheim, GER
Random hexamer primer [1 mM]	Roche, Mannheim, GER
RNase-ExitusPLUS	Applichem, Darmstadt, GER
RNaseZap-Wipes	Ambion, Huntingdon, UK
Silica gel with moisture indicator	Merck, Darmstadt, GER
Sodium Acetate, [3M]	Ambion, Huntingdon, UK
Stirrup-shaped blade	Roth, Karlsruhe, GER
SUPERaseIn™ RNase Inhibitor [20U/µl]	Ambion, Huntingdon, UK
SuperScript™ II Reverse Transcriptase (200U/µl)	Invitrogen, Carlsbad, US
TAE Buffer 50x (2M Tris-Acetate, 0.05M EDTA, pH 8.3)	Eppendorf, Hamburg, GER
Tissue Freezing Medium	Leica, Wetzlar, GER
Tris	Sigma, Munich, GER
TWEEN20 (polyoxyethylenesorbitan monolaurate) 10% aqueous solution	Sigma, Munich, GER
Water, Mol Bio grade	Eppendorf/5Prime, Hamburg, GER

The used consumables are summarized in Table 5. Standard laboratory consumables are not separately listed.

Table 5: List of used laboratory consumables.

Comsumable	Manufacturer
96-well reaction plate	ThermoFisher, Waltham, US
MicroAmp Optical Adhesive Film, PCR compatible	Applied Biosystems, Foster City, US
PCR SingleCap 8erSoftStrips 0.2 ml	Biozym, Hessisch Oldendorf, GER
PCR Tubes Thinwall Clear 0.5 ml	Axygen, Tewksbury, US
PEN (polyethylene naphthalat) membrane slides, 2 µm	MicroDissect, Mitenaar, GER
Pipette tips with filter	Kisker, Steinfurt, GER
Razor blades	Carl Roth, Karlsruhe, GER
Reaction tubes (0.5/1.0 ml), single sealed safe lock	Eppendorf, Hamburg, GER
Syringe Filter, 0.1 µm pore size	GE Healthcare Life Sciences, Freiburg, GER
Sieve inlay for falcon tubes	Workshop of Ulm University, Ulm, GER
Thermo-Fast 96-well PCR detection plates	ThermoFisher Scientific, Waltham, US
UVpette tip	Biozym, Hessisch Oldendorf, GER

2.3 Buffers, master mixes and Kits

The ingredients of all buffers and solutions that were used in this work are given below.

A Diethylpyrocarbonate (DEPC)-water

1 ml DEPC stock solution (100%) + 1 l H_2O deionized

B Cresyl violet (CV) staining solution (1% CV in 100% EtOH) for the staining of cryosections of murine brain tissue (50 ml stock solution):
0,5 mg cresyl violet-acetate
ad 50 ml ethanol absolute.

To reach a higher solubility of CV in ethanol, the CV staining solution was left for at least two weeks at 4°C after preparation. Before each use, the solution was sterile-filtered with a sterile filter syringe (0.1 µm pore size; Whatman).

C Ethanol dilutions for fixation of cryosections (50 ml falcon tubes each)
75% - 37.5 ml ethanol absolute (Sigma) + 12.5 ml RNase-free H_2O (Qiagen)

95% - 47.5 ml ethanol absolute (Sigma) + 2.5 ml RNase-free H_2O (Qiagen)
100% - 50 ml ethanol absolute (Sigma)

100% - 50 ml ethanol, anhydrous (Alfa Aesar)

D Ethanol andhydrous for fixation of cryosections:

1 l ethanol anhydrous (90% ethanol, 5% isopropanol, 5% methanol, Alfa Aesar) stored with 25 g/l molecular sieve (0.3 nm pore size)

E 1x TAE (Tris-Acetate-EDTA) buffer for gel electrophoresis and preparation of agarose gels
25 ml 50x TAE (2 M Tris-Acetate, 0.05 M EDTA, pH8.3)
ad 1 l Aqua dest. (from an ultrapure water system)

F 10x RTB (reverse transcription buffer):
dNTPs (20 mM each) (GE Healthcare)
random hexamers (1 mM) (Roche)
TrisHCl (100 mM, pH 8) (Sigma, VWR)
(aliquots stored at -20°C)

G 5x FSB (First-Strand-Buffer):
5x FSB was supplied together with the reverse transcriptase (ThermoFisher Scientific) and contains 250 mM TrisHCl (pH 8.3), 375 mM KCl and 15 mM $MgCl_2$ (aliquots stored at -20°C)

Table 6 shows all used master mixes and Kits.

Table 6: List of used master mixes and Kits.

Master mix / Kit	Application	Manufacturer
Agilent RNA 600 Nano Kit	RIN-Analysis of isolated RNA	Agilent, Böblingen, GER
HotStarTaq Master Mix Kit	Multiplex-PCR	Qiagen, Hilden, GER
QuantiTect Probe PCR Kit	realtime Taqman PCR	Qiagen, Hilden, GER
RedTaq ReadyMix PCR Reaction Mix	Nested-PCR	Sigma, Munich, GER
RNeasy Mini Kit	RNA-Isolation from tissue	Qiagen, Hilden, GER
DNA Micro Kit	DNA-Isolation from hMNs	Qiagen, Hilden, GER

2.4 Primers for multiplex-nested-PCR, genotyping-PCR and RT-qPCR

All used oligonucleotides (primers) for multiplex-nested-PCR, PCR-based genotyping and RT-qPCR are listed in Table 7, Table 8 and Table 9 respectively.

Table 7: List of used mouse primers for qualitative multiplex- and nested-PCRs.
Shown are respective multiplex (outer) and nested (inner) forward (F) and reverse (R) primers. Information comprises sequences in 5'-3' direction, accession numbers according to the National Center for Biotechnology Information (NCBI) as reference for sequence as well as position and length of the resulting PCR-amplicon in base pairs. Note that the nested-PCR for glutamate decarboxylase (GAD) involves two primer pairs (GAD65/67) thus is also a multiplex-PCR. amp. length: length of the resulting PCR-amplicon.

Gene	Primer	Primer sequence (5`-3`)	Accession No. (according to NCBI)	5`-Position	amp. length (bp)
Choline acetyl-transferase (ChAT)	mChAT-F (outer)	CCTGCCAGTCAACTCTAGCC	NM_009891	637	834
	mChAT-R (outer)	ACATTTCCACCTCAGCCTTCT		1471	
	mChAT-F (inner)	TTCTCATCATACCGGCTTCC		839	296
	mChAT-R (inner)	CCGGTTGGTGGAGTCTTTTA		1135	
Glial fibrillary acidic protein (GFAP)	mGFAP-F2 (outer)	AGAACAACCTGGCTGCGTAT	K01347	407	786
	mGFAP-R33 (outer)	GCTCCTGCTTCGAGTCCTTA		1192	
	mGFAP-F12 (inner)	AGAAAGGTTGAATCGCTGGA		472	517
	mGFAP-R8 (inner)	CCAGGGCTAGCTTAACGTTG		988	
Glutamate decarboxylase variant 65 kD (GAD65)	mGAD65-F15 (outer)	CATACGCAGACAGCACGTTT	NM_008078.1	166	905
	mGAD65-R15 (outer)	AAAAGATTCCATCGCCAGAG		1070	
	mGAD65-F1 (inner)	GGGATGTCAACTACGCGTTT		606	389
	mGAD-R11 (inner)	CACAAATACAGGGGCGATCT		994	
Glutamate decarboxylase variant 67 kD (GAD67)	mGAD67-F21 (outer)	TGACATCGACTGCCAATACC	Z49976	731	1105
	mGAD67-R12 (outer)	GGGTTAGAGATGACCATCCG		1835	
	mGAD67-F22 (inner)	CATATGAAATTGCACCCGTG		761	702
	mGAD67-R17 (inner)	CGGTGTCATAGGAGACGTCA		1462	

Primers for genotyping-PCR are listed in Table 8.

Table 8: Mouse primers for PCR-based genotyping of wildtype (SOD1 wildtype) and mutated (SOD1^{G93A}) SOD1 mice.
Information comprises sequences in 5'-3' direction of forward (F) and reverse (R) primers, accession numbers according to the National Center for Biotechnology Information (NCBI) as reference for sequence as well as position and length of the resulting PCR-amplicon in base pairs

Gene	Primer sequence (5‘-3‘)	Accession no. (NCBI)	Amplicon length [bp]
SOD1 wildtype-F **SOD1 wildtype-R**	CTAGGCCACAGAATTGAAAGATCT GTAGGTGGAAATTCTAGCATCATCC	NM_011434.1	324
SOD1 ^{G93A}-F **SOD1 ^{G93A}-R**	CATCAGCCCTAATCCATCTGA CGCGACTAACAATCAAAGTGA	NM_011434.1	236

TaqMan assays for RT-qPCR are listed in Table 9. Corresponding standard curve parameters are listed in the *Results* section.

Table 9: Mouse TaqMan quantitative PCR assays that were used in this work for quantificaton of calcium (Ca^{2+}) transporter as well as marker genes.
Information comprises probe sequences in 5'-3' direction, accession numbers according to the National Center for Biotechnology Information (NCBI) as reference for sequence and position, length of the resulting PCR-amplicon in base pairs (bp), spanned exons, (*) Primers did detect but not discriminate between described splice variants. For all other genes, no different splice variants are known to date. assayID: assay identification number at life technologies. amp. length: length of the resulting PCR-amplicon. NCX: plasmalemmal Na^{+}/Ca^{2+} exchanger, PMCA: plasma membrane Ca^{2+} ATPase, UCP: Uncoupling protein, LETM1: Leucine zipper EF hand-containing transmembrane protein 1, MNCX: Mitochondrial sodium-Ca^{2+} exchanger, MCU: Mitochondrial Ca^{2+} uniporter, MICU1: Mitochondrial Ca^{2+} uptake 1, MCUR1: Mitochondrial Ca^{2+} uniporter regulator 1, ChAT: Choline acetyltransferase, GFAP: glial fibrillary acidic protein, ND1: NADH dehydrogenase subunit 1.

assay ID	target gene / primer sequence	genbank accession no. (NCBI)	amp. length [bp]	exon
Mm01168774_m1	**MCU (Ccdc109a)** CACCAAAGAGAGACCTCCTAAGCCA	NM_001033259.3	92	4-5
Mm01173692_m1	**MICU1 (Cbara1)** AGACAGAAAAGTGATGGAGTATGAG	NM_144822.2	67	3-4
Mm01351581_m1	**MCUR1 (Ccdc90a)** AAAGCAACAAGTGATGGATGAAGTG	NM_001081059.3	98	5-6
Mm00522265_m1	**LETM1** GCCAGCTGAAACAGTGGCTGGACTT	NM_019694.1	74	7-8
Mm01197102_m1	**MNCX (Slc24a6) *** TAGTCAAGTTGCCTGTGGAGTTCTT	NM_133221.2 NM_001177594.1 NM_001177595.1	61	9-10/ 10-11
Mm01274107_g1	**UCP2** GGTCCGGCTGCAGATCCAAGGGGAG	NM_011671.4	82	3-4
Mm00494077_m1	**UCP3** GTCTCACCTGTTTACTGACAACTTC	NM_009464.3	69	5-6
Mm01245805_m1	**PMCA1 (Atp2b1)** GGGGACCTTACTCTGGGGCCAGCTT	NM_026482.2	77	19-20
Mm00437640_m1	**PMCA2 (Atp2b2) *** ATAGGCAAGGCGGGCCTGGTGATGT	NM_001036684.2 NM_009723.3	79	7-8
Mm00623641_m1	**PMCA3 (Atp2b3)** AGACAAGAAAGGCAAGCAGCAGGAT	NM_177236.3	71	6-7
Mm01285597_m1	**PMCA4 (Atp2b4) *** TGAAAACCTCCCCTATAGAAGGTCT	NM_213616.3, NM_001167949.1	86	1-2
Mm01232255_m1	**NCX1 (Slc8a1) *** ACTGTCAGCGCTGGGGAAGATGACG	NM_001112798.1 NM_011406.2	65	7-8/ 9-10
Mm00455836_m1	**NCX2 (Slc8a2)** AGGTGTAGTCCAGGTGTGGGAGGCA	NM_148946.2	100	2-3
Mm00475520_m1	**NCX3 (Slc8a3) *** CATCACTGTTAGTGCAGGAGGGGAT	NM_080440.3, NM_001167920.1	71	5-6/ 6-7
Mm01221882_m1	**ChAT** TAGCTGTGAGGAGGTGCTGGACTTA	NM_009891.2	67	3-4
Mm01253033_m1	**GFAP *** AGAAAACCGCATCACCATTCCTGTA	NM_001131020.1 NM_010277.3	75	6-7
Mm04225274_s1	**ND1** ACAACCATTTGCAGACGCCATAAAA	NC_005089_ND1.0	81	-

2.5 Breeding and clinical assessment of SOD1^{G93A} mice

Transgenic mice of the strain B6SJL-Tg(SOD1*^{G93A})1Gur/J (referred to as SOD1^{G93A}) carrying 20-24 copies of the mutant human SOD1 gene (see 1.7) were utilized. Hemizygous male SOD1^{G93A} mice and their wildtype littermates were kept in the ZFE Frankfurt (experiments performed in 2011, expression data for MCU/MICU1) and the TFZ Ulm (experiments performed in late 2012, all other expression data) in groups with a maximum of three animals in a 12 hours light/dark cycle and at a temperature of 21° C. Mice had ad libitum access to normal food and water. Two weeks before reaching the terminal stage of illness (around P110) mice kept in the ZFE Frankfurt were transferred to the University of Ulm, where they were held until preparation. During that time, all animals were subjected to daily control of physical health. Transgenic animals showing signs of disease, e.g. an unsteady gait or reduced limb splay (Leitner et al. 2009) were given soaked food on the cage floor to ensure adequate liquid intake. For analyses, SOD1^{G93A} mice between P115 and P145 (referred to as endstage) were used after they were no longer able to pass a paw grip endurance test (clinical score 4, (Solomon et al. 2011)) and results were compared to age-matched WT littermates. All animal procedures were approved by the German Regierungspräsidium Tübingen (AZ 35/9185.81-3 TV No. 1090, and O-147). Detailed information of all individual animals is given in 3.2.

2.6 Establishing a RNase free environment

To prevent contamination by RNA degrading enzymes, e.g. ubiquitous RNase A, prior to work, all laboratory surfaces, such as benchtops or centrifuges, were cleaned with RNase decontamination solution. Metal equipment and glassware were baked out over night at 220°C. Consumables and reagents (e.g. H_2O, Ethanol) were purchased certified RNase free. Reusable plastic ware (e.g. Eppendorf pipettes, Tube holders) was treated with UV-C light (λ=254 nm) for at least 45 min under a sterile workbench, and kept in that workbench in general.

2.7 Brain tissue preparation of SOD1^{G93A} and WT mice

Before use, all surgical instruments used for brain-preparation were pre-cooled on ice. Mice were deeply anaesthetized with Isoflurane by inserting them into an Isoflurane-saturated chamber. Deep anesthesia was verified by testing the absence of the eyelid closure reflex. Decapitation was performed while preserving the first cervical vertebra as safety distance to the brain stem. With fine scissors this remaining vertebral body was cut dorsally, thus entering the foramen magnum and following the sagittal suture of the calvarium until reaching Bregma. Now the bones were folded aside using a forceps. A coronal cut 2 mm rostral of the bregma enabled separation from the rostral part of the osseus skull. During brain removal, mechanical irritation of the nerves was avoided by their proper sectioning. With a stirrup-shaped blade, the brain was cut coronally at the transition zone from the cortex to the cerebellum. For sections of the hypoglossal nucleus, the caudal tissue block was glued with their rostral plane to the specimen holder - that was previously prepared with Tissue-Tec Medium - and immediately frozen by insertion into the snap freeze holder (-35°C) of a cryostat (Leica CM 1850).

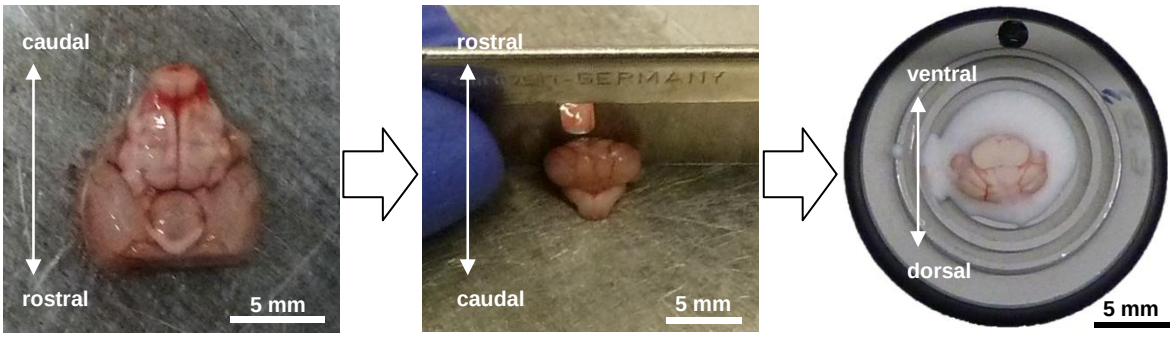

Figure 7: Preparation of tissue blocks containing hypoglossal nucleus.
(Left) shows the brain from ventral after it was removed out of the skull (after separation from the rostral skull by sectioning, see text). (Mid) the tissue block containing hypoglossal nucleus is separated from the forebrain. (Right) is a caudal view of the brainstem tissue block (cerebellum pointing downwards) containing the hypoglossal region, glued to the specimen holder with Tissue-Tec Medium. Scale bars as indicated.

2.8 Cryosectioning and staining of murine coronal brain tissue

After 10 minutes at -35°C in the snap-freeze holder, another 15 minutes at -27°C and 45 minutes equilibration at -18°C, 12 µm serial coronal brainstem sections were cut with a Leica cryotome (CM 3050 S) and mounted on 2 mm PEN -membrane slides. Following 2 minutes fixation in 75% ethanol at -20° C, sections were stained with 1% cresyl violet solution for 60 seconds. Fixation was carried out by dipping the slides shortly in an ascending series of 75%, 95% and 100% ethanol and inserting them for another 60 seconds in alcohol composed of 90% ethanol, 5% methanol and 5% isopropanol for complete dehydration. Before storing at -80°C, sections were dried for 30 minutes in a RNase free, silica gel-filled drying chamber.

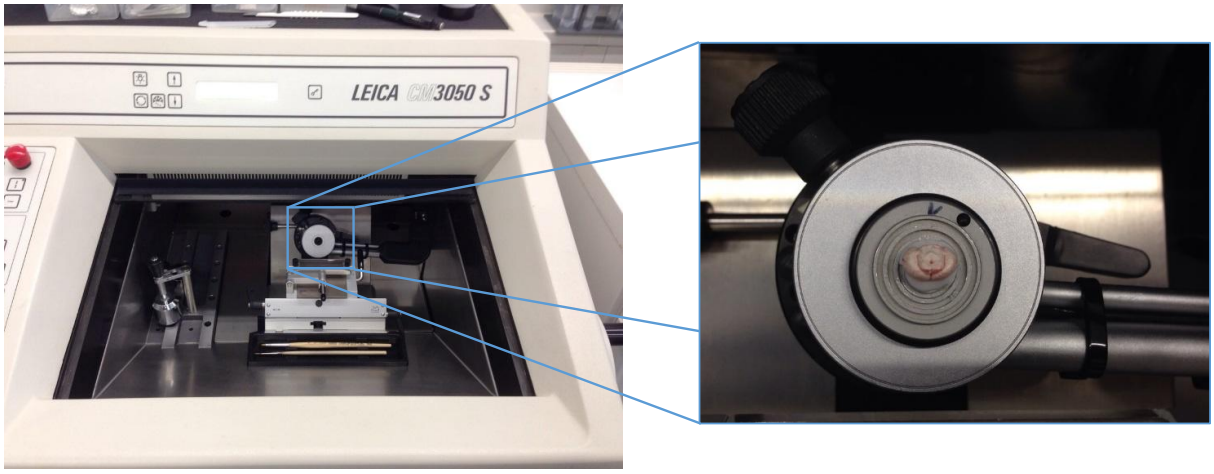

Figure 8: Cryotome and murine brain tissue fixed on cryostat holder.
Left: Internal sectioning set-up of a Leica Cryotome CM 3050 S which was used for cryosectioning.
Right: Detailed picture of fixed murine brain on a small cryostat holder.

2.9 Identification of hMNs in murine brainstem cryosections

Besides motor neurons, GABAergic neurons as well as glial cells have been described to be located within the hypoglossal nucleus. While GABAergic neurons are situated particularly near the midline (van Brederode et al. 2011), glial cells show abundance throughout the whole nucleus (Cova and Aldskogius 1985). Of these three cell types, motor neurons are the largest with a diameter ranging from 20-30 µm and a soma area of about 300 µm² (Ukabam 1988; Yasuda et al. 2002), that is roughly threefold the area of GABAergic neurons (van Brederode et al. 2011). For that reason, pre-identification was done mainly by cell size (diameter and area), determined with the LMD software, and position (motor neurons more laterally). In addition, collected cell pools were checked for GABAergic and glial contamination before expression analysis via marker gene PCR (see 2.17.2).

2.10 Contact-free UV-laser microdissection of individual hMNs of murine brainstem cryosections.

Single hypoglossal motor neurons were excised out of coronal brainstem sections via contact free UV-laser microdissection (UV-LMD). For this purpose, a Leica LMD 7000 set-up was used, consisting of an upright digital microscope (Leica DM6500) connected to an UV-diode laser (355 nm). The cold ablation technique of this laser disrupts covalent bonds with UV photons neither altering morphology nor chemistry

of the specimen collected or the surrounding tissue. The sample-containing 2 mm PEN-slide was placed upside down on the slide holder that allowed simultaneous work on up to three series of sections (compare Figure 9). Cresyl violet stained neurons were subsequently visualized under brightfield 63-fold magnification and sectioning lines were drawn. The laser was automatically guided along the lines and dissected cells were collected by gravity into the subjacent collection vessel (0.5 ml nuclease free thin walled reaction tube, Axygen) which are fixed in the cap holder positioned directly under the slide holder. The cap holder was self-manufactured from the university-internal workshop.

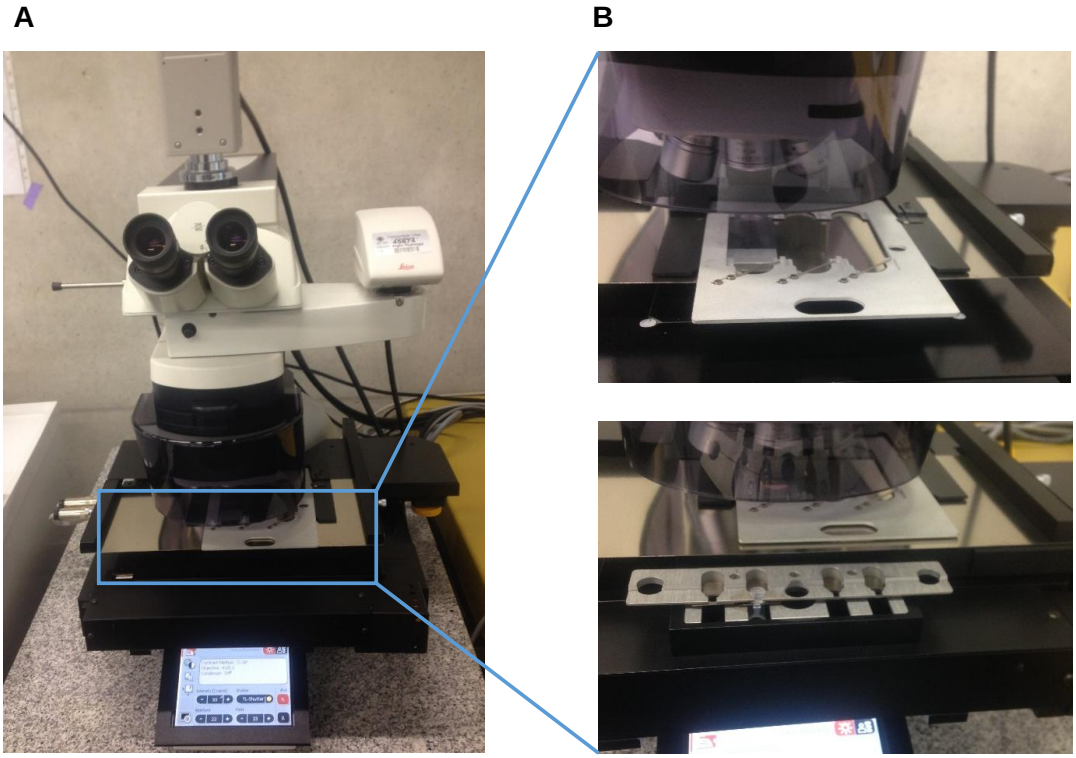

Figure 9: Leica LMD7000 microscope used for UV-laser microdissection.
(A) Photograph of the used LMD7000 setup with the Leica DM 6500 microscope. (B) Upper: Detailed photograph of the slide holder, placed on a motorized stage containing a PEN-slide with mounted cresyl violet-stained coronal mouse midbrain slices. Lower: Detailed photograph of the cap holder with a tube placed in position B.

Microscope and laser were accessed via the LMD7000 software (Version 6.7.2.4295, Figure 10) All settings concerning light intensity, focus and magnification level were adjusted via the “Microscope control” configuration panel. “Laser control” settings allow adjustment of laser energy (Power), lens aperture affecting sectioning

precision (Aperture) and moving speed of the laser during cutting (Speed). The frequency of the laser pulse can be accessed via the "Pulse frequency" parameter. "Head current" allows to determine the overall output percentage of laser current (see Table 10). To favor transfer of specimen into the tube, additional power can be placed on the final laser pulse by enabling the parameter “Specimen Balance”. Another function named “Collector” shows the cap of the collection tubes in 4-fold magnification. After sectioning it was checked whether transfer of the microdissected cells into the cap had been successful. Furthermore, the LMD7000 software is connected to IM1000 database software for image documentation.

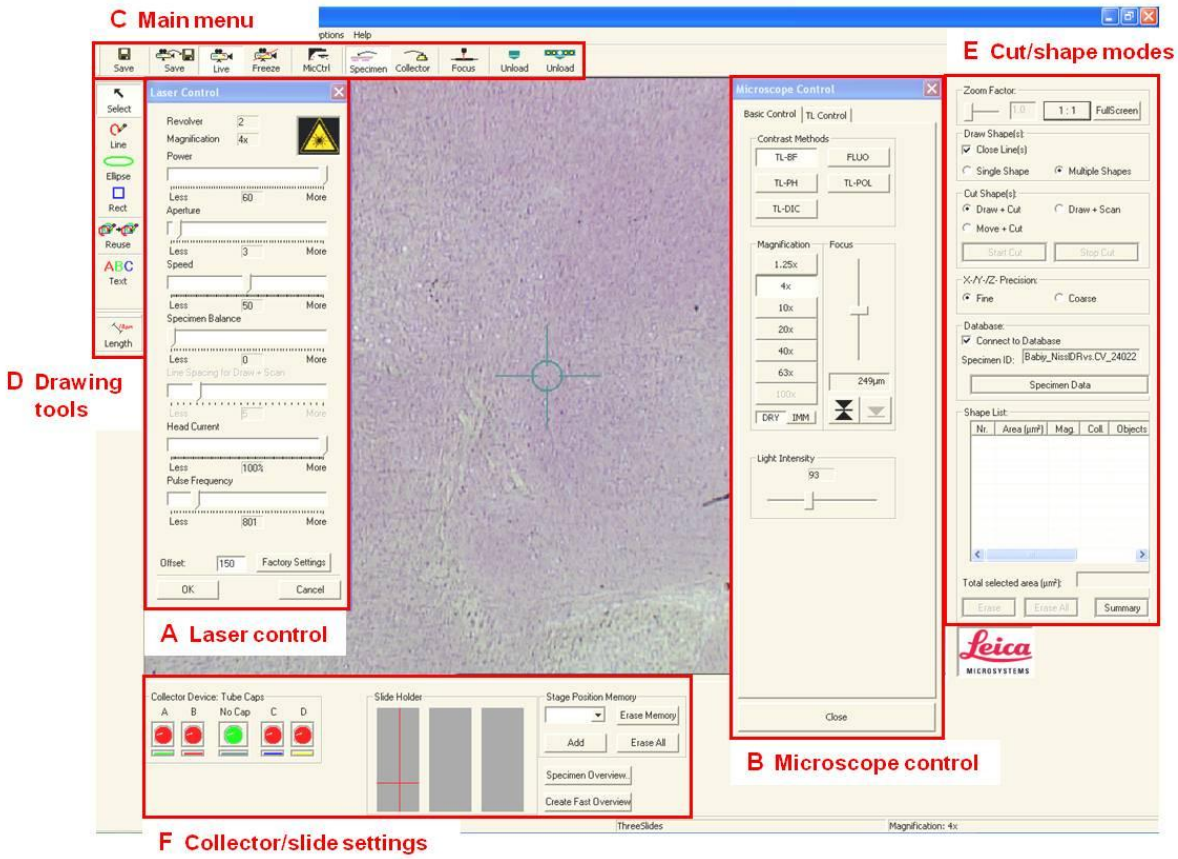

Figure 10: User-mask of the Laser Microdissection (LMD) software with the respective menu bars.
The LMD software allows fully automated control of the UV-LMD setup. The respective menu bars are indicated as follows: A. The menu bar "Laser control” allows adjustment of the laserbeam settings power, aperture, speed, specimen balance, head current, pulse frequency and offset. For detailed description and selected value of each setting please see **Table 10**. B. The “Microscope control” allows automated switching of objectives and contrast mode. C. The “Main menu” controls the cap holder, the slide holder and the camera. D. The “Drawing tools” enable changing of the selection tool and sizing distances at the object. E. The “Cut/shape modes menu” harbors the selection between different cutting modes (“Draw + Cut”, “Draw + Scan”, “Move + Cut”) and shows a summary table of the selected object with a connection to the data base. F. The “Collector/slide settings” gives an overview over the cap holder and the slide holder. It further harbors a position memory function as well as the possibility to generate a specimen overview for a better orientation on the slide in higher magnifications.

The optimal laser settings were determined for murine brainstem tissue and hypoglossal motor neurons in an independent series of experiments and then preserved for the whole study to prevent methodological bias.

Table 10: Laser control settings of the LMD7000 software for UV-LMD of individual hMNs used and held constant throughout the whole series of experiments.

Setting	Description	Value
Power	Energy of the laser	13
Aperture	Width of the cutting line	3
Speed	Cutting speed	15
Specimen Balance	Additional pulse intensity of the last laser impulses	0
Offset	Internal lense distance for determining of the focus	250
Head Current	Percentage of the selected power	100%
Pulse Frequency	Frequency of the pulse	800

2.11 Reverse transcription (RT) of isolated total brainstem RNA

For cDNA synthesis, 10 µl isolated RNA (see 2.16.1) together with 10 µl cDNA synthesis mix were incubated for 2 h at 38°C in a thermomixer (Eppendorf) (350 rpm interval mix each 10 min). The composition of the reaction mixture is shown in Table 11.

Table 11: Reaction mix for cDNA synthesis of isolated total brainstem RNA.
*contains 250 mM TrisHCl (pH 8.3), 375 mM KCl and 15 mM $MgCl_2$ and was supplied with the Reverse Transcriptase.
**contains 20 mM dATP, 20 mM dGTP, 20 mM dCTP and 20 mM dTTP, 1 mM random hexamers and 100 mM TrisHCl, pH 8.

Component	Stock	Volume (20 µl total)	End concentration
FSB (“First Strand Buffer“)*	5x	4 µl	1x
RTB (“Reverse Transcriptase Buffer“)**	10x	2 µl	1x
DTT (Dithiothreitol)	100 mM	2 µl	10 mM
SRS (SuperRNasin)	20 U/µl	1 µl	1 U/µl
Reverse Transcriptase (SuperScriptII)	200 U/µl	1 µl	10 U/µl
Eluted RNA	-	10 µl	-

2.12 Combined cell lysis and cDNA synthesis of individual hMNs after UV-LMD

A combined lysis and cDNA-synthesis to avoid material loss was performed. The laser mix was freshly prepared before every laser experiment for the total number of hMN pools (20-30 per UV-LMD session), importantly, without the reverse transcriptase, and stored on ice in the dark. Contents of the mix are given in Table 12. 4.7 µl of mix were pipetted directly into the collection cap after UV-LMD of hMNs. Incubation for 2 minutes at 72°C in a ThermoStat (Eppendorf) enabled thermal and chemical cell lysis followed by cooling on ice for five seconds. After centrifugation for 1 minute at 11200 rcf (MiniSpin Plus, Eppendorf) at room temperature and cooling on ice for another minute, 0.3 µl of reverse transcriptase (Superscript II) were added. Reverse transcription was done by incubating the samples in a thermomixer (Eppendorf) at 38°C for 2 h interval shaking and subsequently in a thermoblock (Eppendorf) at 39°C over night.

Table 12: Combined lysis and cDNA synthesis mix
* 5x First Strand Buffer (FSB, Invitrogen) contains 250 mM TrisHCl pH 8.3, 375 mM KCl, 15 mM $MgCl_2$
** 10x Reverse Transcriptase Buffer (RTB) contains 20 mM dNTPs (each), 1 mM random Hexamer Primer, 100 mM TrisHCl pH 8. Please note that a mastermix for 20-30 lysis and cDNA reactions was made, but Reverse Transcriptase was added separately to each reaction after lysis was performed.

Component	Stock Conc.	Final Conc.	Volume
First Strand Buffer (FSB)*	5x	1x	1 µl
Dithiothreitol (DTT)	100 mM	10 mM	0.5 µl
Reverse Transcriptase Buffer (RTB)**	10x	1x	0.5 µl
Polyinosinate	1 µg/µl	0.1 µg/µl	0.5 µl
Nonidet P40	10%	0.5%	0.25 µl
Super-RNAsin (SRS)	20 U/µl	1 U/µl	0.25 µl
H_2O	-	-	1.7 µl
Reverse Transcriptase	200 U/µl	12 U/µl	0.3 µl
			∑ = 5.0 µl

2.13 Precipitation of single cell cDNA for purification

Components of the cDNA synthesis mix, especially the reverse transcriptase itself, were observed to dramatically inhibit downstream PCR reactions (Liss 2002). A way to overcome this problem is ethanol precipitation of the cDNA (i.e in most cases in a volume of 5 µl) in the presence of 1/10 volume of the solution to precipitate sodium acetate and suitable carriers to avoid single cell cDNA loss (Liss 2002). Therefore, 7.3µl of precipitation master mix (Table 13, amount according to respective number

of samples for precipitation) were added to each sample as well as 40 µl (i.e. about 3-fold the volume to precipitate) of ethanol absolute (99.9%, Applichem) (samples were vortexed and spun down after each step). Samples were incubated at -20°C to precipitate over night. cDNA was pelletized by centrifugation at 16.100 rcf (Centrifuge 5804R, Eppendorf) for 2 h and supernatant was discarded via careful pipetting. Subsequently, pellets were washed with 100 µl of 80% ethanol (Applichem) followed by another centrifugation step (16.100 rcf for 15 min). Again the supernatant was removed carefully, and cDNA pellets were dried at 45°C in a thermomixer without shaking (Eppendorf). All ethanol had to evaporate before resolving the pellet in the desired amount (17 µl for UV-LMD samples, 11 µl for standard curve serial dilutions) of sterile, RNase free water (Molecular biology grade, 5Prime). Finally, to completely resolubilize cDNA, another incubation step was carried out for 2 h at 45°C in a heating block of a thermomixer (Eppendorf) with interval mix at 450 rpm.

Table 13: Precipitation master mix components.

Component	Stock Conc.	Final Conc.	Volume
Glycogen	1 µg/µl	~0.08 µg/µl	1 µl
Polydeoxycytidylate	1 µg/µl	~0.028 µg/µl	0.35 µl
Sodium acetate	3 M	~0.29 M	1.2 µl
H_2O	-	-	4.8 µl
			∑ = 7.35 µl

2.14 Determination of nucleic acid concentrations

Nucleic acids concentrations of an individual sample can be determined by photometric measurement of its light absorption. Subsequently, after calibration to a blank, the sample concentrations can be determined by application of Beer's law:

$$\boldsymbol{A = \varepsilon \cdot c \cdot d \rightarrow c = \frac{A}{\varepsilon \cdot d}}$$

Figure 11: Beer's law.
A: absorption of the measured substance, ε: specific extinction coefficient, dependent on the substance (ε=0.027 $(\mu g/ml)^{-1}$ cm^{-1} for single stranded cDNA, 0.020 for double stranded DNA and 0.025 for RNA), c: concentration of the measured substance, d: layer thickness, dependent on the photometer cuvette size (d=1 mm for used picodrop suitable pipette tips)

A picodrop photometer enables concentration measurements in µl volumes by using a 10 µl Gilson pipette and special, non-UV light-absorbing pipette tips as cuvettes (UVpette tip, Biozym). The pipette tip containing the sample is placed in the beam of light including wavelenghts of 260 nm and 280 nm that correspond to the absorption of nucleic acids and protein contaminations, respectively. After measurement and software-assisted data aquisition and calculation of DNA-concentrations and possible protein contaminations, the whole sample can be recovered without loss.

2.15 Analysis of RNA integrity number (RIN)

To evaluate the quality of RNA, the RNA integrity number (RIN) of a respectively RNA sample, isolated from tissue, and used for standard curve cDNA synthesis, was determined with the “lab-on-a-chip” based Bioanalyzer 2100 (Agilent) combined with the RNA 6000 Nano-Kit (Agilent). The method principle is based on a gel electrophoresis, yet strongly reduces separation time as well as sample and reagent consumption. The fluorescence marker enables to follow the migration of the samples in the gel and the assignment of the individual samples. According to that, the 2100 Expert Software generates an electropherogram (Figure 12C/D) and calculates the RIN values out of the fragment length distribution and based on the signal of the 18S and the 28S ribosomal RNA (exact algorithm remains a corporate secret of Agilent). A resulting RIN value of 10 corresponds to completely intact RNA, while a value of 1 reflects fully degraded RNA.

The separation procedure itself is performed on a Nano-Chip that has to be previously loaded with polymer gel. This gel additionally contains a fluorescent agent that binds to RNA strands (loading dye). Due to its high viscosity, it must be pressed into the chip’s capillaries with a 1 ml syringe and the so-called priming station (provided by Agilent, Figure 12A, left).

Subsequently, 1.5 µl of each RNA sample is mixed with 5 µl of fluorescent marker that indicates the dye front during electrophoresis. 6 µl of each sample-marker mix are brought into the chips apertures. In addition, the chip accommodates a well for an external standard that contains fragments of known size (ladder, Figure 12C). After

being loaded with gel matrix, samples and ladder, the chip was vortexed for one minute at 240 rpm in a Chip-Vortexer (Agilent) and inserted into the bioanalyzer (Figure 12A, right). Finally, the method was started via a connected computer and the 2100 Expert software in the “Eucaryotic Nano Array” profile.

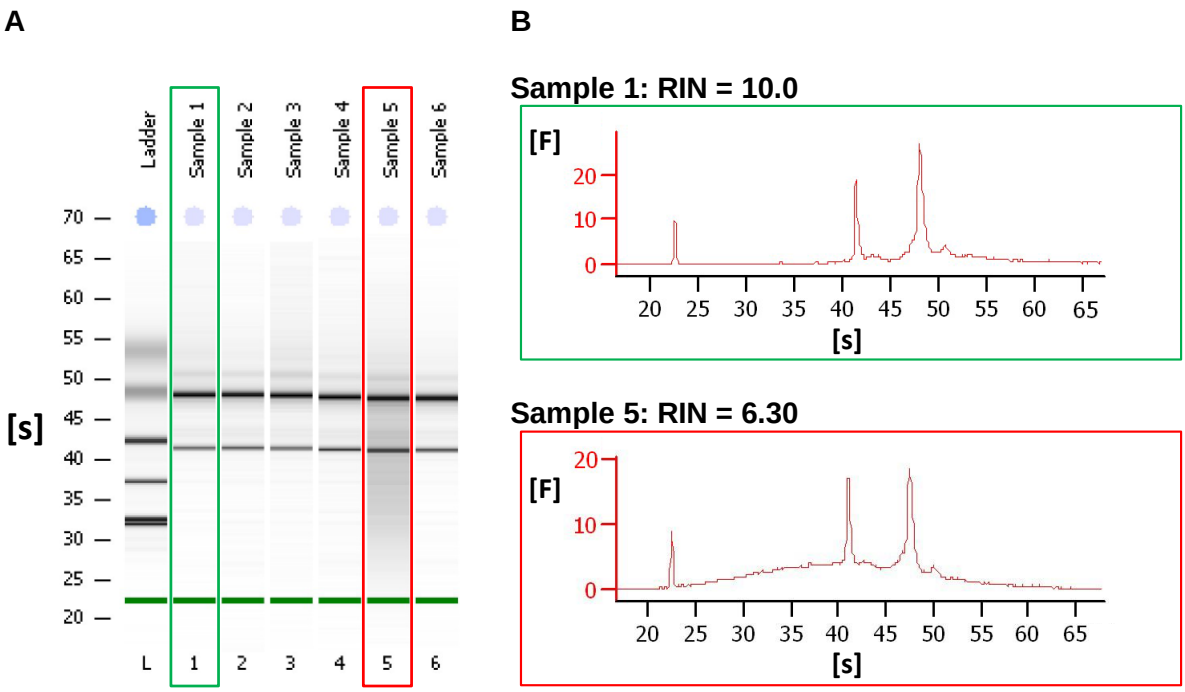

Figure 12: Analysis of RNA integrity number (RIN) via Agilent Bioanalyzer 2100.
(A) Overview on samples of one run with y-axis representing runtime in seconds and x-axis representing individual sample number (L: ladder, external standard RNA). Green frame depicts one fully intact sample (Sample 1) with a RIN of 10.0, while red frame depicts a partially degraded RNA sample (Sample 5) with all samples of one run together. Peaks/dark bands in (A) and (B) show 18s and 28s rRNA bands (B) fragment's distribution by quantity (in fluorescence units [F], y-axis) and length (run-time in seconds [s], x-axis) for two individual samples with a fully intact sample (Sample 1, upper) with a RIN of 10.0 and a partially degraded RNA sample (Sample 5, lower).

As gene expression analysis in this work was based on freshly prepared murine brainstem tissue that was immediately frozen and stored at -80°C, RNA integrity was generally expected to be high. Therefore, RIN analysis was performed after representative RNA preparations according to 2.16.1 (tissue-derived wildtype whole brainstem cDNA for standard curve evaluation) and, as it confirmed very high RNA quality (mean RIN value: 9.84 ± 0.12, n = 8 samples), not performed again afterwards.

2.16 Nucleic acid isolation

2.16.1 Isolation of RNA from murine brainstem tissue

Isolation of total RNA from murine brainstem tissue was performed using the RNeasy Mini Kit according to the manufacturers protocol. Brainstem tissue was quick-frozen in liquid nitrogen, grinded and homogenized with a 21G syringe needle in 600 µl lysis buffer (RLT, provided by Kit). The RLT-buffer contains the chaotropic agent Guanidinium-thiocyanate, which denatures proteins by disruption of hydrogen bonds. 6 µl β-Mercaptoethanol (provided with Kit) was freshly added to the RLT-buffer prior to isolation. It denatures proteins (and thus RNases) by reducing disulfide bonds to free thioles. The homogenization contributes mechanically to the cell lysis and degrades DNA molecules by shear forces. Subsequently, the lysate was centrifuged to separate the lipids from the aqueous phase and to pelletize the lysed cell fragments. 600 µl 70% Ethanol was added to the hydrous phase containing the nucleic acids for DNA precipitation and transferred on a silica column. RNA molecules bind via hydrogen bonds to the silica gel membrane. To remove residual protein and cell fragments, the precipitate was washed and centrifuged (1 min, 15.600 rcf, Centrifuge 5415R, Eppendorf) three times according to the protocol. Afterwards, the RNA was eluted with 30 µl nuclease-free H_2O in a 1.5 ml tube, by pipetting it on the column and centrifuging (1 min, 15600 rcf, Centrifuge 5415R, Eppendorf) and stored at -80°C. All steps of the isolation occurred at room temperature.

2.16.2 Isolation of DNA from single hMNs

For analysis of mitochondrial genome copy number, single hMNs were laser-microdissected and DNA isolation was performed with the QiaAmp DNA Micro Kit according to manufacturer’s protocol. A total of 40 µl ATL-buffer (tissue lysis buffer, provided with the Kit - exact composition is a secret of Qiagen) and 10 µl Proteinase K were added to each laser-microdissected sample and incubated at 56°C in 0.5 ml single sealed tubes for 3 h with interval mixing every 10 min. The ALT-buffer contains chaotropic agents, which denature proteins by disruption of hydrogen bonds. Proteinase K has exo- and endopeptidase activity, thereby cleaving peptide bonds. Subsequently, 50 µl of AL-buffer (lysis buffer, provided with the Kit - exact

composition is a secret of Qiagen) and 50 µl of 100% ethanol (for nucleic acid binding to the silica column via hydrogen bonds) were added and incubation at room temperature was performed for 5 min. The whole lysate was transferred on a silica column placed on a 2 ml collection tube (provided with the kit) and centrifugation was done for 1 min at 5900 rcf (Centrifuge 5415R, Eppendorf). To remove residual protein and cell fragments, the precipitate was washed and centrifuged twice (AW1- and AW2-buffer, provided with the Kit - exact composition is a secret of Qiagen) according to the protocol. Finally, DNA was eluted with 30 µl of molecular biology grade water into a 1.5 ml tube by centrifuging 1 min at 20000 rcf (Centrifuge 5415R, Eppendorf) and stored at 4°C until PCR amplification.

2.17 Polymerase Chain Reaction (PCR)

The polymerase chain reaction exponentially amplifies a distinct DNA sequence. The method relies on thermal cycling, that means cyclic repetitions of melting and subsequent enzymatic replication of the double stranded DNA. First step is the denaturation of double stranded DNA that occurs at high temperatures (94-95°C). After that, temperature is lowered to enable short oligonucleotides (primers) to anneal to their complementary sequences on the DNA strands. The annealing temperature depends mainly on length and GC content of the primer (usually between 50°C and 70°C). Primers define starting and end point of the PCR product, as their 3'OH-ends serve as binding sites for a heat stable DNA dependent DNA-polymerase (e.g. Taq polymerase from *Thermus aquaticus*). In the last step of the amplification cycle, this enzyme elongates the primer with desoxyribonucleotides (dNTPs) along the template strand, thereby creating another double stranded DNA molecule. By doubling the desired DNA sequence from cycle three on, PCR kinetics should ideally be exponential.

2.17.1 Genotyping-PCR for confirmation of SOD1^{G93A} transgenic and wildtype genotype

Mouse tail or ear tissue-biopsies were incubated over night with 100 µl of freshly prepared Lysis-Buffer (Table 14) and 10 µl Proteinase K (Roche, 10 mg/ml) in a

Thermomixer (Eppendorf) at 60°C and 600 rpm interval mix. Subsequently, Proteinase K was inactivated by incubation for 15 min at 94°C.

Table 14: Components for freshly prepared Lysis-Buffer of murine tail/ear tissue.
*provided by ThermoFisherScientific, contains 200 mM TrisHCl (pH 8.0), 500 mM KCl together with Taq DNA polymerase

Component	Stock Conc.	Final Conc.	Volume
PCR Buffer*	10x	1x	10 µl
NP40 (Nonidet P40)	10%	0.45%	4.5 µl
TWEEN 20 solution	10%	0.45%	4.5 µl
H_2O	-	-	81 µl
			∑ = 100 µl

Tissue residues were then spun down for 5 min at 13100 rcf (MiniSpin plus, Eppendorf). PCR was carried out as multiplex-PCR with two specific primer pairs, one detecting murine wildtype SOD1 and another detecting human mutant SOD1 (for sequences, see Table 8. All four primers were stored at stock with 25µM each. PCR-Mix is given in Table 15. The utilized RedTaqReadyMix already contains the loading dye for subsequent gel electrophoresis.

Table 15: Genotyping-PCR-Mix components.
*provided by Sigma, contains 0.06 U/µl of HotStarTaq DNA Polymerase in final concentration, 3 mM $MgCl_2$ and 0.4 mM of each dNTP and loading buffer for subsequent gel electrophoresis

Component	Stock Conc.	Final Conc.	Volume
RedTaqReadyMix*	2x	1x	25 µl
Primer-Mix	25 µM each	0.13 µM each	0.26 µl
Genomic DNA	-	-	5 µl
H_2O	-	-	19.74 µl
			∑ = 50 µl

A 9700 GeneAmp PCR System (Applied Biosystems) was used as thermocycler with the conditions shown in Table 16, and 0.2 ml SingleCap 8-tube strips for PCR reaction. An initial denaturation step at 95° C for 15 minutes is required for activation of the HotStar Taq Polymerase, thereby avoiding formation of misprimed products and primer dimer formation at lower temperatures.

Table 16: Genotyping-PCR cycling parameters.

Cycling-Step	Temperature	Duration	No. Cycles
HotStart	95°C	3 min	1x
Denaturation	95°C	30 sec	35x
Annealing	60°C	45 sec	
Elongation	72°C	1 min	
Final Elongation	72°C	5 min	1x
Final Hold	4°C	∞	

Visualization of the genotyping-PCR products was carried out after agarose gel electrophoresis, which was carried out essentially as described in 2.17.3

2.17.2 Qualitative multiplex-nested-PCR

Motor neurons express the marker choline acetyltransferase (ChAT), while surrounding glial cells specifically express “glial fibrillary acidic protein” (GFAP) and GABAergic neurons are marked by glutamate decarboxylase (GAD, two isoforms GAD65 and GAD67). Multiple primer sets (see table Table 7, *outer primers*) within a single PCR mix were used, suited to amplify the desired marker genes (ChAT, GFAP and GAD65/67) in one PCR reaction. In a following nested-PCR, new sets of primers are used (Table 7, *inner primers*) whose binding sites are located within the target sequence of multiplex-PCR, now in individual PCR-reaction for each primer pair and with 5 µl of multiplex-PCR product each as templates. High abundance of the pre-amplified multiplex-PCR product compared to unspecific primer binding sites increases sensitivity and specificity of nested-PCR. Each multiplex and nested primer pair spans an intron of several 1000 bp in the respective genomic DNA sequence each. This ensures, that only cDNA but not genomic DNA is amplified in this PCR approach.

Multiplex-PCR was carried out in 50 µl reaction volume in 0.2 ml SingleCap 8-tube strips in a thermocycler (9700 GeneAmp PCR System, Applied Biosystems). The so-called 9600 emulation mode was chosen for ramp speed, meaning heating and cooling with 1°C per second. 45 µl of Multiplex-PCR mix were given in each tube before 5 µl of the respective template cDNA was added.

Table 17: Multiplex-PCR-reaction components
* provided by Qiagen, contains 5 U/µl of HotStarTaq DNA Polymerase in final concentration, 3 mM $MgCl_2$ and 0.4 mM of each dNTP . Note that, in contrast to nested-PCR, multiplex-PCR master mix contains all primers, but no cDNA.

Component	Stock Conc.	Final Conc.	Volume
HotStarTaq Mastermix*	2x	1x	25 µl
Primer Pairs (F+R)	50 µM each	1 µM each	1 µl each
Template cDNA	-	-	5 µl
H_2O	-	-	19 µl
			∑ = 50 µl

For details of multiplex-PCR-Mix and cycling conditions, see Table 17 and Table 18.

Table 18: Multiplex-PCR conditions.

Cycling-Step	Temperature	Duration	No. Cycles
HotStart	95°C	15 min	1x
Denaturation	94°C	30 sec	
Annealing	58°C	1 min	35x
Elongation	72°C	3 min	
Final Elongation	72°C	7 min	1x
Final Hold	4°C	∞	

Nested-PCRs were carried out in 25 µl reaction volumes in 0.2 ml SingleCap 8-tube strips in the same thermocycler (9700 GeneAmp PCR System, Applied Biosystems) with the same ramp speed (9600 emulation mode) as described above. 1 µl of the forward/reverse primer-mix (50µM each) was placed at the bottom of each tube and afterwards, 24 µl of the cDNA containing mix were added. For each multiplex-PCR, one individual nested-PCR mastermix was prepared (i.e. for 10 samples and 4 genes, 10 4,2 fold mixes). For details of nested-PCR-Mix and cycling conditions, see Table 19 and Table 20.

Table 19: Nested-PCR-Mix components
*provided by Sigma, contains 0.06 U/µl of HotStarTaq DNA Polymerase in final concentration, 3 mM $MgCl_2$ and 0.4 mM of each dNTP and loading dye for subsequent gel electrophoresis. Note that, in contrast to multiplex-PCR, nested-PCR master mix contains template cDNA from multiplex-PCR, but primers are added seperately for each reaction.

Component	Stock Conc.	Final Conc.	Volume
RedTaq ReadyMix*	2x	1x	25 µl
Primer Pairs (F+R, as mix)	50 µM each	2 µM each	1 µl each
Template cDNA	-	-	1.5 µl
H_2O	-	-	Ad 25 µl
			∑ = 25 µl

Table 20: Nested-PCR conditions.

Cycling-Step	Temperature	Duration	No. Cycles
Initial Denaturation	94°C	2:30 min	1x
Denaturation	94°C	30 sec	35x
Annealing	58°C	1 min	
Elongation	72°C	1 min	
Final Elongation	72°C	7 min	1x
Final Hold	4°C	∞	

Visualization of the nested-PCR products was carried out after agarose gel electrophoresis, which was carried out essentially as described in 2.17.3. However, for this purpose, a 2% TEA agarose containing gel was used.

2.17.3 Agarose gel electrophoresis

The agarose gel electrophoresis serves to visualize the products of the qualitative multiplex-nested-PCRs. It is a method to separate DNA molecules in an agarose gel matrix corresponding to their particular size by applying voltage. Because nucleic acids are negatively charged, the molecules move in the electric field to the positive pole (anode). The gel matrix determines the migration velocity of the separating DNA fragments due to its pore size and does not interact with the nucleic acids.

A 2% agarose gel was prepared by dissolving the agarose powder in 1x TAE buffer (see composition in 2.3) and boiled in a microwave. After cooling, ethidium bromide (stock: 1µg/µl; end concentration 0.1 µg/µl) was added and the solution was filled into a cast for polymerization. The absorbance of this agent shows two maxima at 210 and 285 nm and intensifies up to 20-fold after binding to DNA, enabling identification

of DNA-bands in UV-light. The gel was loaded with 12 µl of each PCR product and 6 µl of a DNA ladder as DNA size standard (GeneRuler, 100 bp DNA Ladder). The applied voltage was dependent on the gel size. A big gel (~29x18 cm) ran at 120-150 V. In this way, negatively charged DNA molecules were sorted based on their size with smaller fragments moving faster through the agarose grid. The DNA fragments on the agarose gels were visualized in the gel documentation system BioDocII after UV excitation at a wavelength λ of 312 nm. Figure 13 shows an exemplary agarose gel with genotyping-PCR products.

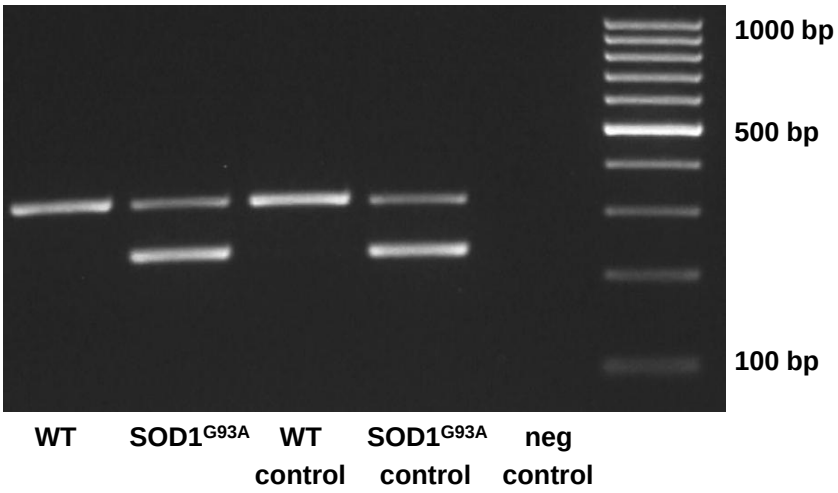

Figure 13: Agarose gel (2%) electrophoresis of genotyping-PCR products for murine tail tissue of wildtype (WT) and SOD1^{G93A} transgenic animals.
Shown are PCR products of a sample WT and SOD1^{G93A} animal as well as a WT, SOD1^{G93A} and negative control (from left to right). The ladder (right) contains DNA fragments with known size in intervals of 100 base pairs. Note that animals that carry the mutant gene show two bands, one for wildtype SOD1 DNA at 324 bp and one for mutant human SOD1^{G93A} DNA at 236bp. In contrast, their wildtype littermates displayed only one band for the wildtype SOD1 at 324bp. bp: base pairs, WT: wildtype.

2.17.4 Quantitative realtime-PCR (qPCR) using TaqMan primer/probe assays

Real-time quantitative PCR (qPCR) is the gold standard for quantitative reverse transcription (RT) based gene expression analysis (Arikawa et al. 2008). It uses fluorescent reporter dyes that bind either non-sequence-specifically (SYBRgreen) to double stranded DNA or sequence-specifically (TaqMan Probe / Scorpion Primers) to single stranded DNA. After each cycle, fluorescence intensity is detected depending on the used method (SYBRgreen or TaqMan, see below), generating a fluorescence plot. The increase in fluorescence in the exponential phase of PCR is ideally proportional to the amount of DNA produced during each PCR cycle, thereby

allowing quantification of starting amouts of DNA – in respect to a relative or absolute DNA-standard. Quantity is determined at the PCR cycle at which fluorescence first reaches a manually defined threshold level (so called cycle at threshold or C_t-Value). Sample C_t-values are converted to expression level values, in respect to a standard curve with known concentrations, according to the formula shown in Figure 18.

Normal qPCR fluorescence plot consists of a linear *baseline region*, where fluorescence of the emerging PCR product is below the detection threshold. In the following *exponential phase* the amount of the PCR product is doubled in each PCR cycle, due to optimal PCR conditions and 100% PCR efficiency. After a certain number of cycles (mostly between 25 and 35), the efficiency of the polymerase decreases due to exhaustion of the reagents, also called the *"linear" phase*. In the final *plateau phase*, the total consumption of the reagents leads to cessation of the reaction. The four characteristic phases of the fluorescence signal during qPCR are illustrated in Figure 14. The ROX (5-carboxy-X-rhodamine derivate) dye provides an internal reference to which the reporter-dye signal can be normalized during data analysis. Normalization is necessary to correct for fluorescence fluctuations due to changes in concentration or volume. Consequently, fluorescence values of each PCR cycle that were normalized to ROX are given as ΔRn.

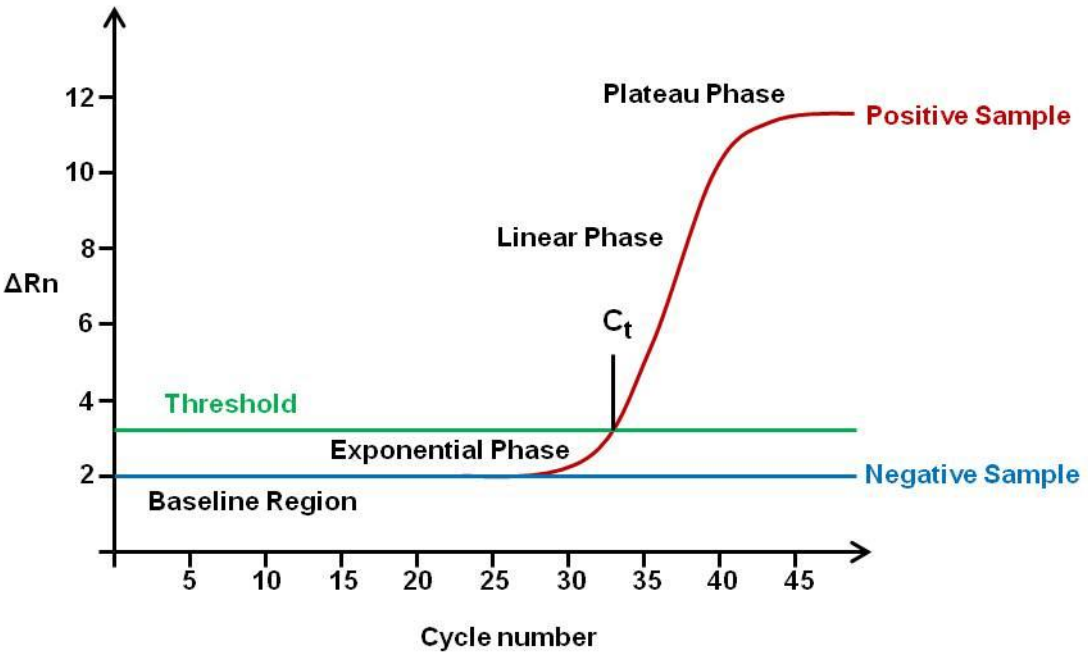

Figure 14: Four phases of a a quantitiative PCR reaction.
The plot (blue line) starts with a baseline region, where signal cannot be separated from noise, in this work determined as cycle 3 to 15. Subsequently, in the exponential phase, the amount of fluorescence doubles with the produced DNA amount. In the linear phase, amplification slows down, because reagents run low. In the final plateau phase, the total consumption of reagents leads to cessation of the PCR reaction. The green line indicates the signal of a negative control with no template. ΔRn: relative level of fluorescence, Threshold: fluorescence level where the cycle number is read out. C_t: cycle number at threshold.

All RT-qPCR experiments in this work were carried out on a GeneAmp 7900HT (Applied Biosystems) with a 96-well block. Fluorescence excitation in this system is operated via a 488 nm argon ion laser and the emission is detected through a CCD. 96-well Detection Plates (Fisher Scientific) were covered with ABI Prism optical adhesive covers (Applied Biosystems). Programming and subsequent data analysis were carried out using the SDS-(Sequence-Detection-System)Software (Version 2.3).

The most important feature of TaqMan qPCR is the presence of a third oligonucleotide called probe, which hybridizes within the target sequence amplified by the two primers, and generates a fluorescent signal within the elongation phase of each PCR cycle, thereby providing additional specificity. The probe typically spans an exon-exon boundary, thereby preventing amplification of genomic DNA, as it only binds to mRNA derived cDNA. In this work, the probe was labeled at the 5' phosphate with a fluorescent reporter dye (FAM, a derivate of 6-carboxyfluorescein, $\lambda_{Absorption}$=494 nm, $\lambda_{Emission}$=518 nm) and at the 3'OH end with a non-fluorescent quencher (black hole quencher, BHQ). When near to the fluorescent dye, the quencher suppresses the fluorescent signal via fluorescence resonance energy

transfer (FRET). However, during the elongation step, 5'-3' exonuclease activity of the polymerase cleaves the bound probe and thus frees the fluorophore from the quencher, and fluorescence is emitted and can be detected by the qPCR cycler (compare Figure 15). A combined annealing and elongation step for 1 min at 60°C instead of the traditional three-step PCR cycle ensures, that the probe remains bound to its target during primer extension, since TaqMan probes are typically designed to have a length of 80 bp and a melting temperature (T_m) of 60-70°C.

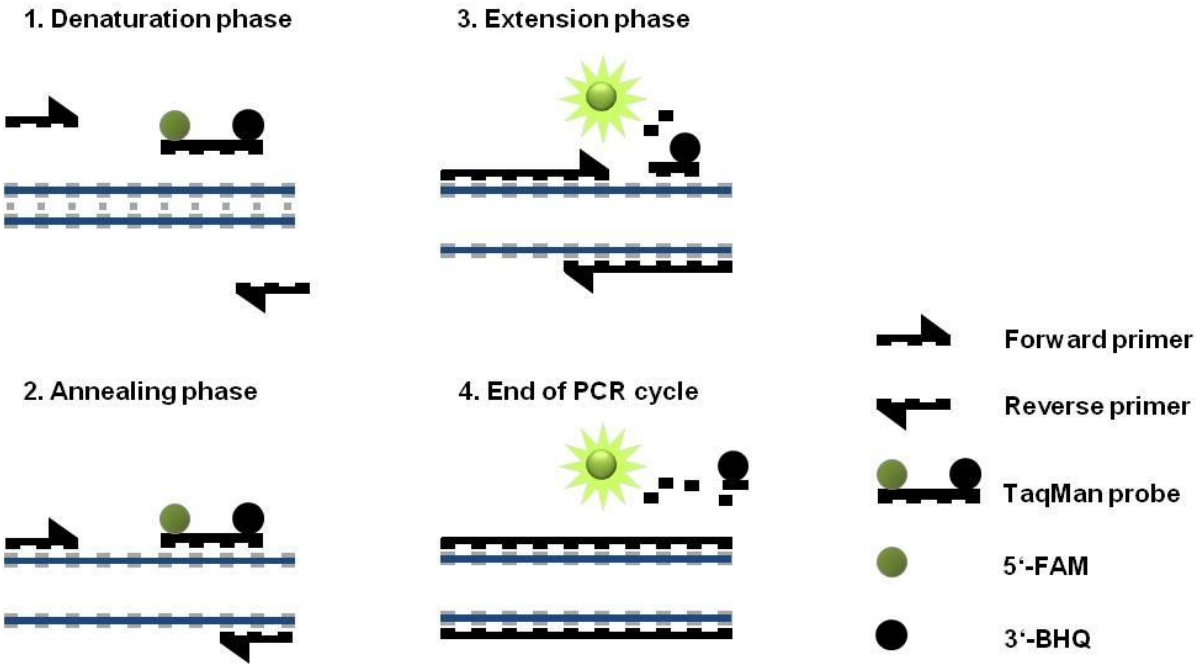

Figure 15: Principles of TaqMan PCR.
Illustration of a typical qPCR cycle and fluorescence detection principle of TaqMan assays. After the denaturation phase, TaqMan probes bind to specific single stranded DNA-sequences. When the reporter dye (5'-FAM) is separated from the quencher (3'-BHQ) by the proof reading Taq-polymerase via hydrolysis during the extension phase, it emits its fluorescence which is recorded at the end of each PCR cycle. FAM = Fluorescein, BHQ = Black hole quencher.

For details of TaqMan PCR-Mix and cycling conditions, see Table 21 and Table 22.

Table 21: TaqMan PCR-Mix reaction components.
*contains the HotStarTaq DNA polymerase, the ROX passive reference dye, desoxynucleotides and the QuantiTect Probe PCR Buffer including KCl and $(NH_4)_2SO_4$ (exact composition remains manufacturers secret), which promote specific primer annealing, enabling high PCR specificity and sensitivity.

Component	Stock Conc.	Final Conc.	Volume
QuantiTect Probe PCR Master Mix*	2x	1x	10 µl
Primer Probe Mix	20x	1x	1 µl
H_2O (5Prime)	-	-	4 µl
Template cDNA	-	-	5 µl
			∑ = 20 µl

An UNG (uracil N-glycosylase) step (2 min at 60°C incubation of the PCR reaction prior to amplification) prevents contamination with carried-over PCR products. That is, because besides the four nucleotides dATP, dTTP, dCTP and dGTP, also dUTP nucleotides are contained in the Qiagen PCR mixes which are integrated competing with dTTP. The Qiagen PCR Kits are available with an UNG which breaks N-glycosylated bonds and eliminates possible existent contaminations with dUTP containing double stranded DNA, thus PCR products from previous PCR runs (see QuantiTect® Probe PCR Handbook, Qiagen Homepage). The here used PCR Kits did not contain UNG, but the UNG step was retained in the PCR program. The PCR Kit included a HotStar TaqPolymerase (Qiagen). This polymerase exhibits a 5`-3`exonuclease activity and needs a heat activation step (15 min, 95°C) which reduces unspecifc amplification during the first denaturation cycle.

Table 22: TaqMan PCR conditions.
UNG: uracil N-glycosylase step

Cycling-Step	Temperature	Duration	No. Cycles
UNG	60°C	2 min	1x
HotStart of TaqPol	95°C	15 min	1x
Denaturation	94°C	15 sec	50x
Annealing/Elongation	60°C	1 min	

The PCR reactions were pipetted in a 96-well plate (ThermoFisher) after preparation of a mastermix containing all PCR reaction components but the DNA, in the following way: 15 µl of the respective-master mix were given into each well utilizing the same pipette tip. Afterwards, 5 µl of respective DNA-sample were added (i.e. cDNA for RT-qPCR analysis or mitochondrial genomic DNA for quantification of mitochondrial DNA copy-numbers). qPCR assay details and assay-specific standard curve parameters are given in Table 23. Suitable standard-curves for qPCR quantification were

generated using serial 10X dilutions of cDNA (1:1 = 750 ng/µl, derived from brainstem RNA from a C57Bl/6 mouse of the corresponding age, P120, RIN 9.84, see 2.15) over at least four magnitudes of dilutions, in at least three independent qPCR runs.

2.18 qPCR Data acquisition and analysis

2.18.1 Analysis of realtime qPCR data

The SDS2.3 software shows the absolute fluorescence (Rn), the fluorescence normalized to ROX (ΔRn), the amplification plot with an optional logarithmic Y-axis for better identification of the exponential PCR-phase, and the standard curve plot from each qPCR reaction.

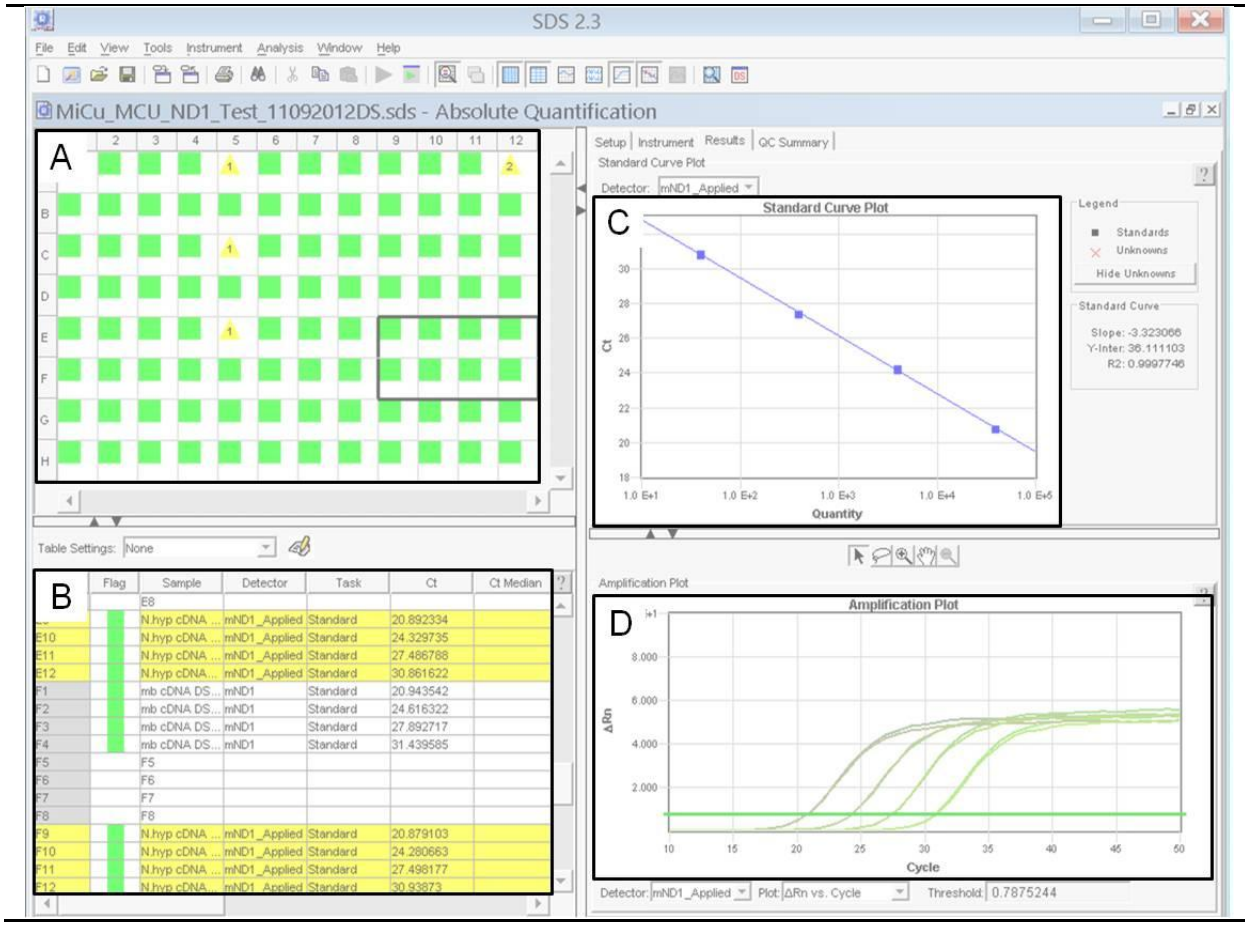

Figure 16: Overview of Applied Biosystems SDS 2.3 software for realtime quantitative PCR data aquisition.
(A,B) 96-well plate, where each well is assigned with a sample number, detector dependent on the gene and, for standard curve generation, the respective dilution step. (C) In the standard curve plot, the known quantity is plotted semilogarithmic against the C_t-values. The calculated slope, y-intercept and R^2 (coefficient of linear regression/determination) of the standard curve are liste on the side. (D) The amplification plot shows the (relative) fluorescence signal plotted linearly or logarithmically against the current cycle. The green line indicates the threshold which is set in the exponential phase.

The analysis of realtime qPCR data with TaqMan assays was performed in the following steps, as specified below:

1. Analysis of background fluorescence and the signal to noise ratio by analyzing the Rn-plot on a linear scale.
2. Determination of the baseline (between the cycles 3 and 15).
3. Normalization of data to ROX passive fluorescence.
4. Identification of the exponential phase of the PCR amplification plot and determination of the threshold for qPCR analysis on a log Y-scale.
5. Analysis of the standard curve parameters from serial dilutions of cDNA standard (slope, y-intercept and R^2) to assess assay kinetics, sensitivity and efficiency (E) of respective qPCRs.
6. Calculation of relative quantities in respect to mouse brainstem tissue derived cDNA standard curves
7. Statistical analysis (mean, SD, SEM, MWU-test, t-test)

The PCR assay performance was evaluated from the standard curve plot (Figure 16) where the used amount of standard DNA was plotted semi-logarithmic against the C_t values. In an assay with an efficiency of 100% the standard curves from serial 10x dilutions of standard DNA show a slope of -3.32. The value can be obtained from the following equation:

$$\boldsymbol{E = -1 + x^{-1/slope}}$$

or respectively

$$\boldsymbol{slope = \frac{-1}{log_x(E)}}$$

Figure 17: Formula for calculation of assay efficiency.
E: amplification efficiency of the assay (2 in this case), x: serial dilution factor (10 in this case). The amplification efficiency of 2 means a duplication of the template per cycle.

2.18.2 Calculation of relative quantity from realtime qPCR data

For in this work determined/utilized threshold cycle (C_t) values as well as slopes and Y-intercepts of respective standard curves, for all individual Taqman assays, see Table 23. The cDNA amount per neuron in relation to the utilized standard, derived from mouse brainstem tissue was calculated as described (Schlaudraff et al. 2014; Gründemann et al. 2008) according to:

$$cDNA\,amount\,per\,cell = \frac{S^{[(Ct - Y_{intercept})/slope]}}{No_{cells} \bullet cDNA\,fraction}$$

Figure 18: Formula for calculation of cDNA amounts based on obtained C_t-value and standard curve parameters from quantitative PCR results.
With *S* = serial dilution factor of the standard curve (i.e. 10), No_{cells} = number of harvested neurons per UV-LMD sample (i.e. 15), *cDNA fraction* = fraction of the UV-LMD cDNA-reaction sample used as template in the individual qPCR reactions (pools of 15 hMNs: 5/17 for Ca^{2+} transporters, and 1/9 for marker genes ChAT, GFAP and ND1; single hMN: 1/2 for marker genes ChAT and GFAP, and 1/6 for genomic ND1). The $Y_{intercept}$ unit-magnitude corresponds to the respective standard utilized (i.e. pg equivalents of standard cDNA, derived from brainstem tissue mRNA) (Gründemann et al. 2008; Schlaudraff et al. 2014).

Single cell cDNA amounts were calculated with a $Y_{intercept}$ of 42 for all Ca^{2+} transporter genes for better comparison, and with $Y_{intercept}$ from respective standard curves given in Table 23 for ChAT, GFAP and NADH dehydrogenase subunit 1 (ND1). Mitochondrial DNA amounts, represented by ND1, were calculated in the same manner. Biological replicates were analyzed by determining mean values, standard deviation (SD) and standard error of the mean (SEM), without and with normalization to ND1 and ChAT DNA/cDNA levels as well as cell size, respectively.

2.18.3 Normalization of realtime qPCR data to mitochondrial DNA, ChAT and cell size

Given the mitochondrial pathologies that have been described in ALS, the number of mitochondria might be altered compared to WT hMNs and even differ among variably diseased $SOD1^{G93A}$ hMNs. To account for these possible variations, expression data of mitochondrial Ca^{2+} transporters were normalized to the number of mitochondrial genomes, represented by the mitochondrially coded ND1 gene that was empirically shown to be almost never affected by mitochondrial DNA deletion events (He et al. 2002; Bender et al. 2006). Thus the amount of genomic ND1 DNA in an individual cell should be linearly correlated to the number of mitochondria in the respective cell. Similarly, the expression levels of plasmalemmal Ca^{2+} transporters were normalized to that of choline-acetyltransferase, the key enzyme for acetylcholine synthesis. It was also a goal of this work to consider variations of cell size, therefore, expression was normalized to the cell area for each hMN pool that is recorded automatically by the LMD software. Normalization to ChAT and ND1 levels was carried out by dividing respective expression values of Ca^{2+} transporters to respective relative ChAT and ND1 expression values, for each individual hMN cell pool. Normalization to cell pool size was carried out by dividing respective mRNA expression values of the investigated genes to respective total area of the cell pool.

2.18.4 Statistical analysis

Microsoft Excel as well as GraphPad Prism (Version 6.01) were used for statistical analysis. Significant differences in the expression analysis of the different genes were tested via the Mann-Whitney-U (MWU) test of GraphPad Prism. The MWU test can be applied on unknown data distribution, contrary to the t-test, which has to be applied only on normal distributions. In addition, the MWU test is more robust, meaning less likely than the t-test to mistakenly indicate significance because of the presence of outliers. All statistical significant differences were determined with a defined significance level of 0.05. In graphs, the p-values < 0.05 are marked with *, p-values < 0.01 with ** and p-values < 0.001 with ***.

3 Results

3.1 Standard curve generation for evaluation of suitable TaqMan assays for RT-qPCR based quantification of Ca^{2+} transporter mRNA levels in individual hMNs

TaqMan assays, suitable for RT-qPCR based quantification of single cell mRNA from hMN, isolated from ethanol-fixed mouse brain sections via UV-LMD, were successfully established for all mitochondrial and plasmalemmal Ca^{2+} transporters as well as marker genes ChAT and ND1 according to 2.17.4. All assays utilized in this study were chosen to detect, but not discriminate between all major functionally described splice variants. To avoid amplification of genomic DNA, all assays were also chosen to be intron-spanning with the amplicon containing an exon-exon boundary, separated by an intron of at least over 1000 bp. To ensure proper amplification independent of RNA integrity status, amplicons were designed to be no longer than 80 bp (Schlaudraff et al. 2014).

For each gene, two to four distinct TaqMan assays were initially chosen according to the above detailed criteria, ordered from life technologies, and tested for sensitivity, reproducibility and amplification kinetics, by using serial dilutions of brainstem tissue derived cDNA to generate standard curves, as described (2.17.4). An ideal assay should display 100% PCR efficiency, represented by a slope of -3.32 in the standard curve plot, if serial dilutions with a factor of ten are used as qPCR templates. Exemplary standard curve amplification plots for MICU1, PMCA3 and ND1, as well as the respective standard curves are given in Figure 19. In the upper graphs, relative fluorescence signals (ΔRn) for the individual TaqMan assays, using standard template cDNAs - in duplicates with concentrations as indicated - are plotted on a logarithmic scale against the PCR cycles on a linear scale. The threshold for further analysis is given by the cycle at threshold (C_t) line (compare Figure 14). In the lower graphs the template cDNA quantities of the standard curves are plotted against the PCR cycle number, where the relative fluorescence signal crosses the manually set C_t-line (also termed C_t value). Detailed standard curve information of all finally chosen assays are summarized in Table 23.

Each standard curve experiment was run usually 3-times, using 4 different concentrations of the same standard curve cDNA as templates (37500, 3750, 375 and 37.5 pg/µl). From these standard curves, one assay each was chosen for each gene that gave the most sensitive and most reproducible results over all four magnitudes of standard template cDNA. Information about the accession number according to the National Center for Biotechnology Information (NCBI), the assay ID, the consensus sequence of the probe, the exon boundary, the assay location and the amplicon length in base pairs and standard curve parameters (threshold, slope, PCR efficiency, y-intercept of standard curves, R^2 of standard curves and n number of independent standard curve replicates) of each analyzed assay are given in Table 23. The R^2 value for the standard curve (numerical value between 1 and 0, where values closer to 1 indicate tighter correlation) describes the correlation between the actual threshold cycles (C_t) and the calculated logarithmic value of the starting copy number for the samples that comprise the standard curve plot. N means the number of all performed standard curve analysis for assay establishing.

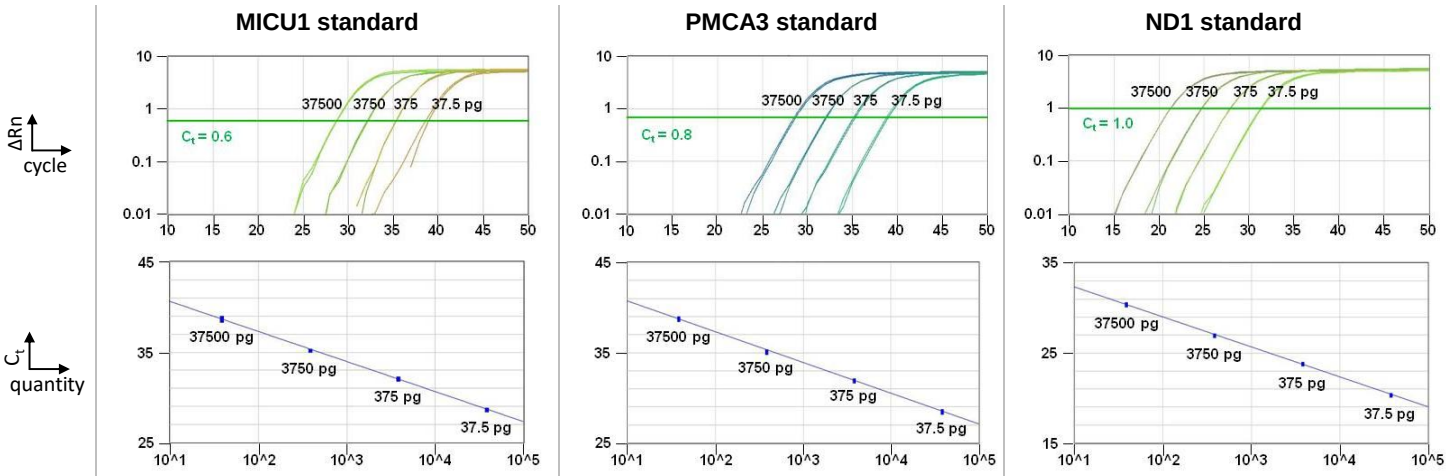

threshold:	0.6	threshold:	0.8	threshold:	1.0
slope:	-3.15	slope:	-3.39	slope:	-3.32
y-intercept:	43.33	y-intercept:	44.31	y-intercept:	36.11
R^2:	0.99	R^2:	1.00	R^2:	1.00

Figure 19: TaqMan realtime quantitative PCR of serial dilutions from 37.5 to 37500 pg of murine wildtype (WT) brainstem standard cDNA for performance test of the TaqMan assays for an exemplary mitochondrial (MICU1), plasmalemmal (PMCA3) and normalization gene (ND1).
For each gene, the amplification plot (top) as well as the standard curve plot (bottom) of serial dilutions from 37.5 to 37500 pg of murine standard cDNA from WT brainstem tissue are shown. In the amplification plot, the relative fluorescence signal (ΔRn) was plotted against the PCR cycles. The threshold is a numerical value assigned in the exponential phase for each individual assay which reflects a statistically significant point above the calculated baseline. The standard curve plot shows the relative quantity (cDNA in [pg]) in dependence of the C_t value. The C_t value is determined at the respective PCR cycle, where the fluorescence signal crosses the threshold. The values for slope, y-intercept and R^2 are exemplary given for the presented plot. The y-intercept represents the extrapolated Y-value for 1pg. The R^2 value represents how well the experimental data fit the regression line. For details see text and **Table 23.** PMCA: plasma membrane Ca^{2+} ATPase, MICU1: Mitochondrial Ca^{2+} uptake 1, ND1: NADH dehydrogenase subunit 1, ΔRn: relative fluorescence, C_t: cycle number at threshold.

Table 23: Information on mouse TaqMan quantitative PCR assays that were used in this work for quantificaton of calcium (Ca^{2+}) transporter as well as marker genes.
Information comprises probe sequences in 5'-3' direction, accession numbers according to the National Center for Biotechnology Information (NCBI) as reference for sequence and position, length of the resulting PCR-amplicon in base pairs (bp), spanned exons, thresholds, y-intercepts, slopes, R^2s and number of performed standard curves. Threshold, slope and y-intercept values were determined with using serial dilutions of cDNA derived from mouse brainstem tissue as qPCR templates. (*) Primers did detect but not discriminate between described splice variants. For all other genes, no different splice variants are known to date. assayID: assay identification number at life technologies. thrsh.: threshold at which C_t values were recorded. n: number of performed standard curves, amp. length: length of the resulting PCR-amplicon. NCX: plasmalemmal Na^+/Ca^{2+} exchanger, PMCA: plasma membrane Ca^{2+} ATPase, UCP: Uncoupling protein, LETM1: Leucine zipper EF hand-containing transmembrane protein 1, MNCX: Mitochondrial sodium-Ca^{2+} exchanger, MCU: Mitochondrial Ca^{2+} uniporter, MICU1: Mitochondrial Ca^{2+} uptake 1, MCUR1: Mitochondrial Ca^{2+} uniporter regulator 1, ChAT: Choline acetyltransferase, GFAP: Glial fibrillary acidic protein, ND1: NADH dehydrogenase subunit 1.

assay ID	target gene / primer sequence	genbank accession no. (NCBI)	amp. length [bp]	exon	thrsh.	y-int.	slope	R^2	n
Mm01168774_m1	**MCU (Ccdc109a)** CACCAAAGAGAGACCTCCTAAGCCA	NM_001033259.3	92	4-5	0.6	45.77 ± 0.13	-3.43 ± 0.02	0.99 ± 0.00	8
Mm01173692_m1	**MICU1 (Cbara1)** AGACAGAAAAGTGATGGAGTATGAG	NM_144822.2	67	3-4	0.6	44.73 ±0.16	-3.39 ±0.05	0.99 ±0.00	8
Mm01351581_m1	**MCUR1 (Ccdc90a)** AAAGCAACAAGTGATGGATGAAGTG	NM_001081059.3	98	5-6	0.6	46.13 ± 0.18	-3.14 ± 0.00	0.99 ± 0.01	2
Mm00522265_m1	**LETM1** GCCAGCTGAAACAGTGGCTGGACTT	NM_019694.1	74	7-8	0.8	44.30 ± 0.44	-3.31 ± 0.11	1.00 ± 0.00	3
Mm01197102_m1	**MNCX (Slc24a6) *** TAGTCAAGTTGCCTGTGGAGTTCTT	NM_133221.2 NM_001177594.1 NM_001177595.1	61	9-10/ 10-11	0.9	49.70 ± 0.71	-3.68 ± 0.17	0.98 ± 0.01	3
Mm01274107_g1	**UCP2** GGTCCGGCTGCAGATCCAAGGGGAG	NM_011671.4	82	3-4	1.2	44.72 ± 0.18	-3.33 ± 0.06	0.99 ± 0.00	4
Mm00494077_m1	**UCP3** GTCTCACCTGTTTACTGACAACTTC	NM_009464.3	69	5-6	0.8	48.62 ± 0.48	-3.33 ± 0.11	0.98 ± 0.01	5
Mm01245805_m1	**PMCA1 (Atp2b1)** GGGGACCTTACTCTGGGGCCAGCTT	NM_026482.2	77	19-20	0.8	44.85 ± 0.32	-3.33 ± 0.09	0.99 ± 0.01	3
Mm00437640_m1	**PMCA2 (Atp2b2) *** ATAGGCAAGGCGGGCCTGGTGATGT	NM_001036684.2 NM_009723.3	79	7-8	1.0	42.32 ± 0.19	-3.29 ± 0.04	0.99 ± 0.00	4
Mm00623641_m1	**PMCA3 (Atp2b3)** AGACAAGAAAGGCAAGCAGCAGGAT	NM_177236.3	71	6-7	0.8	43.94 ± 0.31	-3.30 ± 0.08	1.00 ± 0.00	3
Mm01285597_m1	**PMCA4 (Atp2b4) *** TGAAAACCTCCCCTATAGAAGGTCT	NM_213616.3, NM_001167949.1	86	1-2	1.0	46.86 ± 0.25	-3.23 ± 0.05	0.99 ± 0.01	3
Mm01232255_m1	**NCX1 (Slc8a1) *** ACTGTCAGCGCTGGGGAAGATGACG	NM_001112798.1 NM_011406.2	65	7-8/ 9-10	1.0	45.60 ± 0.38	-3.38 ± 0.06	0.99 ± 0.00	3
Mm00455836_m1	**NCX2 (Slc8a2)** AGGTGTAGTCCAGGTGTGGGAGGCA	NM_148946.2	100	2-3	1.2	46.75 ± 0.24	-3.26 ± 0.08	0.98 ± 0.02	3
Mm00475520_m1	**NCX3 (Slc8a3) *** CATCACTGTTAGTGCAGGAGGGGAT	NM_080440.3, NM_001167920.1	71	5-6/ 6-7	1.0	46.14 ± 0.53	-3.28 ± 0.13	0.99 ± 0.00	3
Mm01221882_m1	**ChAT** TAGCTGTGAGGAGGTGCTGGACTTA	NM_009891.2	67	3-4	0.8	46.13 ± 0.64	-3.04 ± 0.10	0.99 ± 0.00	3
Mm01253033_m1	**GFAP *** AGAAAACCGCATCACCATTCCTGTA	NM_001131020.1 NM_010277.3	75	6-7	0.8	42.41 ± 0.10	-3.29 ± 0.04	0.99 ± 0.00	3
Mm04225274_s1	**ND1** ACAACCATTTGCAGACGCCATAAAA	NC_005089_ND1.0	81	-	1.0	35.60 ± 0.56	-3.34 ± 0.03	1.00 ± 0.00	3

3.2 Information on individual SOD1^{G93A} and wildtype mice analyzed in this study

SOD1^{G93A} mice and their wildtype littermates were bred according to 0. For this study, a total of 10 wildtype and 10 SOD1^{G93A} transgenic animals were utilized, of which 4/4 each were used in 2011, only for MCU/MICU1 quantitative RT-qPCR-based expression analysis (Fuchs et al. 2013) and 6/6 each in 2012 for expression analysis of MCU/MICU1, as well as all other Ca^{2+} transporters, ND1 and ChAT (Mühling et al. 2014). SOD1^{G93A} mice were classified according to their clinical performance with considerable inter-individual variations, ranging from endstage symptoms at postnatal day 116 (ID 572) to postnatal day 149 (ID 574). Variations in disease course were more prominent in the 2012 cohort (endstage symptoms at postnatal day (mean±SD) 131.7±11.0 (WT) and 132.8±11.9 (SOD1^{G93A})) compared to the homogeneous 2011 cohort (postnatal day 127.0±1.2 (WT) and 123.5±2.6 (SOD1^{G93A})). Body weight at preparation date was recorded only for the 2012 cohort and showed the expected significant weight loss for SOD1^{G93A} mice (29.12±2.1 vs. 21.45±2.8, p=0.0065, MWU-Test). Table 24 summarizes all mouse data and indicates the individual scatter plot symbol for Figure 27 and Figure 28.

Table 24: Informations about all individual SOD1^{G93A} and wildtype (WT) mice of which hypoglossal motor neurons were analyzed within this study.
Mice were either from the 2011 (University of Frankfurt animal facitlity) or 2012 (Ulm University animal facility) cohort. ID: identification number (lab registration number), Plot symbol: individual symbol that is used in scatter plots of **Figure 27** and **Figure 28**. Σ: Mean values of the respective dataset ± SD, WT: wildtype animals, TG: SOD1^{G93A} transgenic animals.

ID	Genotype	Preparation date	Age [d]	Weight [g]	Plot symbol
2011					
934	WT	275/11	128	n.a.	▲
946	WT	275/11	128	n.a.	■
957	WT	320/11	126	n.a.	◓
959	WT	320/11	126	n.a.	▼
944	SOD1^{G93A}	274/11	127	n.a.	■
948	SOD1^{G93A}	275/11	121	n.a.	▲
960	SOD1^{G93A}	318/11	124	n.a.	▼
977	SOD1^{G93A}	318/11	122	n.a.	◓
		Σ(2011) =	WT: 127.0 ± 1.2 TG: 123.5 ± 2.6		
2012					
409	WT	298/12	133	32.4	⬡
421	WT	303/12	136	n.a.	□
442	WT	298/12	126	27.9	○
575	WT	341/12	116	28.8	△
557	WT	355/12	130	29.6	▽
580	WT	009/13	149	26.9	◇
410	SOD1^{G93A}	298/12	133	26.9	⬢
417	SOD1^{G93A}	310/12	143	20.0	■
439	SOD1^{G93A}	298/12	126	19.2	●
572	SOD1^{G93A}	341/12	116	21.1	▲
554	SOD1^{G93A}	355/12	130	20.0	▼
574	SOD1^{G93A}	009/13	149	21.5	◆
		Σ(2012) =	WT: 131.67 ± 11.0 TG: 132.83 ± 11.9	WT: 29.12 ± 2.1 TG: 21.45 ± 2.8	

3.3 Determination of cell size of hypoglossal motor neurons in ethanol-fixed cresyl violet stain coronal brainstem sections

In order to analyze gene expression in individual hMNs, the first aim and a prerequisite for all further goals was to establish a protocol for adequate preparation of murine brainstem tissue followed by UV-laser microdissection of individual hMN cell bodies. This first step was successfully taken by adapting the groups known protocol for preparation and UV-LMD of dopaminergic midbrain neurons for hMNs. According to 2.9, hMNs were identified by their size and position in the ventral part of

the hypoglossal nucleus on coronal ethanol fixed and cresyl violet stained brainstem sections (Figure 7). All utilized sections as well as cells pre- and after UV-laser microdissection were photo-documented with the UV-LMD software (Figure 20).

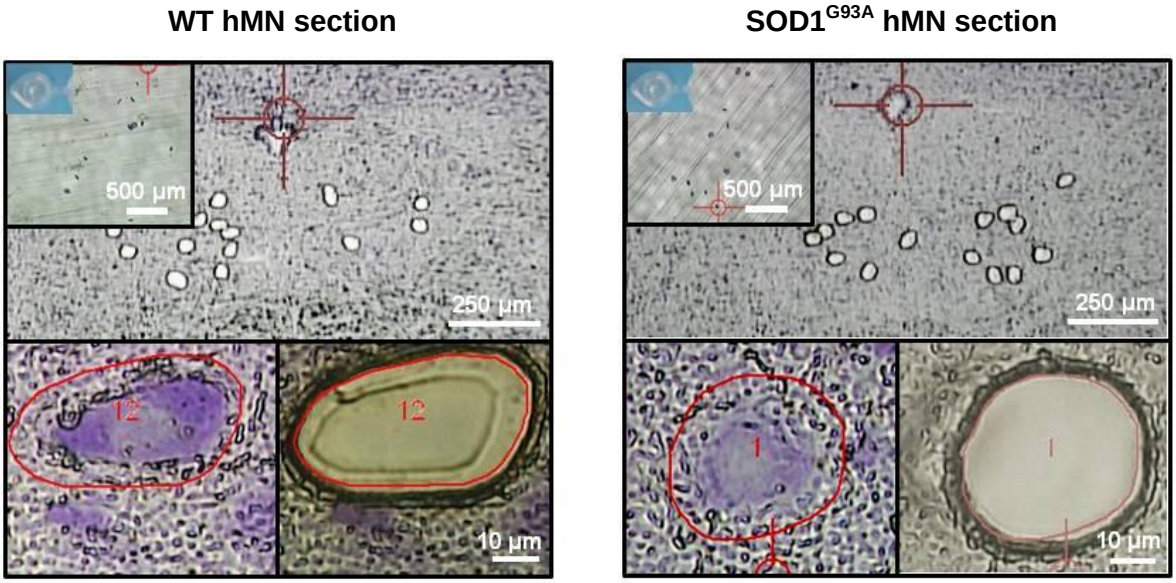

Figure 20: Mouse brainstem histology of the hypoglossal nucleus and illustration of UV laser microdissection (UV-LMD) of its motor neurons.
Upper: Overview of a wildtype (WT, left) and endstage SOD1^{G93A} mouse (right) coronal cresyl violet stained brainstem section after UV-LMD of 15 individual hMNs each. Inserts: photograph of the reaction tube cap for inspection of proper collection of all 15 neurons after UV-LMD, prior to cell lysis and reverse transcription (RT). Lower: one individual hMN each before and after UV-LMD. Scale bars as indicated.

For an estimate of the size lasered hMNs from WT and from SOD1^{G93A} mice, the microdissected area of 15 hMNs each was determined after UV-LMD via the respective LMD software. According to this area quantification, lasered and RT-qPCR analyzed hMNs of SOD1^{G93A} mice were about 5% larger than hMNs of WT control mice (Table 25 and Figure 21A). However, to preserve the entire cell body during laser sectioning, it was necessary to manually include a safety margin around the cell that increases measured areas and could bias actual differences. To address these differences in cell size without sampling artefact, an additional series of area measurements was performed from hMNs on the same sections, independently of UV-LMD experiments, by manually retracing the cell shape, this time without a safety margin. Results from this approach again yielded a similar – but not significant - 5% higher hMN size in SOD1^{G93A} transgenic animals (Table 25 and Figure 21B).

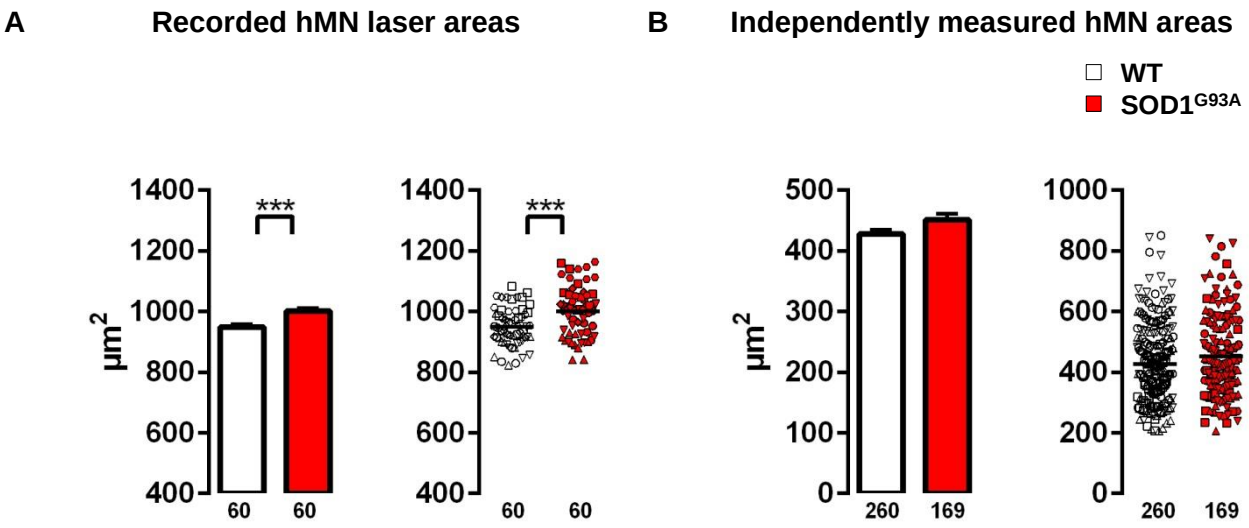

Figure 21: Estimated sizes of hypoglossal motor neurons (hMNs) from wildtype (WT) and SOD1^{G93A} transgenic animals analyzed via realtime quantitative PCR (RT-qPCR) in this study.
Indivdual hMN size estimates in (A) were determined via calculating the mean microdissected area of an individual hMN in pools of 15 cells each, after UV-laser microdissection (UV-LMD) and before RT-qPCR. In (B), an independent cohort of individual hMN from the same sections as in (A) were only carefully encircled with the UV-LMD software for exact area-determination, but not lasered or further processed. Note, that areas between both methods differ considerably, because of the necessary safety margin for UV-LMD. For absolute amounts see **Table 25**. Data are shown as bargraphs illustrating the mean value ± standard error of the mean (SEM) and scatter plots, where each symbol represents either the mean individual hMN area, derived from pools of 15 hMNs each, (A), or independently measured individual hMN areas (B). Number of analyzed hMN pools (A) or individual hMNs (B) given in bargraph. White bars/symbols represent wildtype, red bars/symbols represent SOD1^{G93A} transgenic animals.

Table 25 summarizes area quantifications of laser-microdissected hMN areas as well as independently encircled individual hMN areas.

Table 25: Estimated sizes of hypoglossal motor neurons (hMNs) from wildtype (WT) and SOD1^{G93A} transgenic animals analyzed via realtime quantitative PCR in this study.
Size estimates were derived from determining the lasered area after UV-laser microdissection (UV-LMD) of 15 hMN each (mean value for one individual hMN, left) and by manually encircling and measuring hMN areas via the UV-LMD software (right). Note, that areas between both methods differ considerably, because of the necessary safety margin for UV-LMD. MWU: Mann-Whitney-U-Test.

Area quantification of individual hMNs				
	Recorded hMN laser areas		**Independently measured hMN areas**	
	WT	**SOD1**	**WT**	**SOD1**
Mean ± SEM [µm²]	949 ± 8.14	1001 ± 10.65	428 ± 7.51	452 ± 10.07
n / N	60 / 6	60 / 6	260 / 4	169 / 4
p-value (MWU)	**< 0.001**		0.08	

3.4 Chat and ND1 are suitable genes for normalization of UV-LMD RT-qPCR data from individual hMN from WT and SOD1^{G93A} mice

After successful adaptation of the single cell UV-LMD RT-qPCR protocol from dopaminergic neurons of mouse midbrain preparations to motor neurons of mouse brainstem preparations, I next addressed the question whether the key enzyme for acetylcholine synthesis, choline-acetyltransferase (ChAT) as well as the mitochondrially encoded NADH dehydrogenase subunit 1 (ND1), were suitable genes for normalization and stratification of mouse hMN derived RT-qPCR data.

Quantifying ChAT mRNA in parallel with plasmalemmal Ca^{2+} transporter mRNAs in individual hMNs allows the normalization of plasmalemmal Ca^{2+} transporter expression levels to a highly abundant and motor neuron specific marker gene. As a prerequisite for using ChAT for cell-specific normalization of hMN expression data, expression should not significantly differ in hMNs of WT and SOD1^{G93A} transgenic mice. Indeed, there was no significant difference in ChAT mRNA-levels in single or pooled individual hMNs from WT and SOD1^{G93A} mice (Figure 22 and Table 26). ChAT might thus be more valid for normalization of plasmalemmal Ca^{2+} transporters than cell size, which showed slight but significant alterations when comparing hMNs of WT and SOD1^{G93A} transgenic aminals (see 3.3).

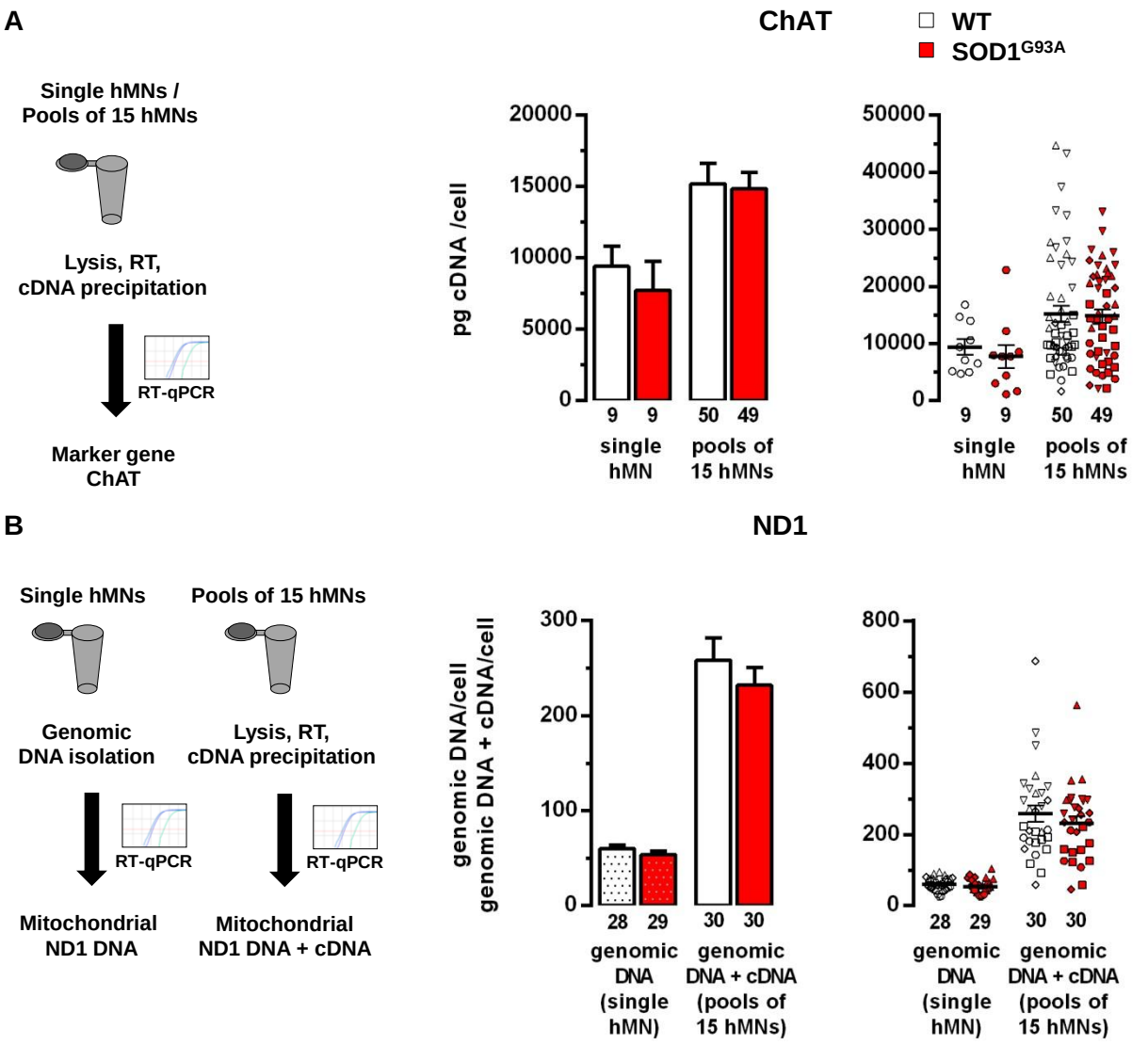

Figure 22: Evaluation of NADH dehydrogenase subunit 1 (ND1) and choline-acetyltransferase (ChAT) expression, used for normalization of cell-specific realtime quantitative PCR (RT-qPCR) data.
(A) RT-qPCR data for ChAT, derived either from single hypoglossal motor neurons (hMNs) or from pools of 15 hMNs each, are similar in wildtype (WT) and SOD1^{G93A} mice, a prerequisite for using ChAT cDNA-levels for normalization of respective plasma membrane Ca^{2+} transporter RT-qPCR results. (B) qPCR data for mitochondrially coded (ND1), using genomic DNA from individual hMNs as templates, indicate similar numbers of mitochondrial genomic DNA molecules in hMN from WT and from endstage SOD1^{G93A} mice. Note that combined mitochondrial genomic DNA and cDNA levels for ND1, determined via RT-qPCR of pools of 15 hMNs each, are also not different between WT and SOD1^{G93A} mice, a prerequisite for using ND1 DNA-levels for normalization of respective mitochondrial Ca^{2+} transporter RT-qPCR results.
For absolute amounts see **Table 26**. Data are shown as bargraphs illustrating the mean value ± standard error of the mean (SEM) and scatter plots, where each symbol represents either cDNA/genomic DNA expression of single hMNs or mean individual hMN mRNA expression, derived from pools of 15 hMNs each. Number of analyzed hMN pools or individual hMNs given in bargraph. White bars/symbols represent wildtype, red bars/symbols represent SOD1^{G93A} transgenic animals. RT: reverse transcription.

Similarly, quantification of ND1 DNA copies in parallel with mitochondrial Ca^{2+} transporter mRNAs in individual hMNs allows the normalization of mitochondrial Ca^{2+} transporter expression levels to the number of mitochondria / mitochondrial genomes

in the respective analyzed hMN pools. To probe if the number of mitochondrial genomes is altered in individual hMNs from WT and SOD1^{G93A} mice, ND1 genomic DNA copy numbers after isolation of genomic DNA from individual hMN were quantified. No significant difference in ND1 genomic DNA levels in individual hMN from WT and SOD1^{G93A} mice was detected (Figure 22 and Table 26). To probe if this is also the case, when analyzing (intronless) genomic ND1 levels without a distinct genomic DNA isolation step by using the in our group established UV-LMD RT-qPCR protocol (a prerequisite for using this gene and this approach for RT-qPCR data normalization), ND1 DNA levels (genomic DNA + cDNA) in respective pools of 15 hMNs from WT and SOD1^{G93A} mice was quantified. Again, no difference between WT and SOD1^{G93A} was detected, but, as expected, about 4-fold higher ND1 DNA levels (genomic DNA + cDNA) per cell (fold difference: WT: 4.28; SOD^{G93A}: 4.30) (Figure 22 *and* Table 26).

Table 26: Summarized expression levels and statistical analysis for marker genes choline acetyltransferase (ChAT) and NADH dehydrogenase subunit 1 (ND1).
The values are given as mean values ± standard error of the mean (SEM). n-values represent the number of analyzed pools while N-values represent the number of analyzed mice. p-values are calculated according to the Mann-Whitney-U (MWU) test of GraphPad Prism. hMNs: hypoglossal motor neurons

Expression of marker genes in single hMNs				
	ChAT		**ND1 (DNA)**	
	WT	**SOD1**	**WT**	**SOD1**
mean±SEM	9411 ± 1405	7743 ± 2012	60.32 ± 3.64	53.91 ± 3.73
n / N	10 / 1	10 / 1	28 / 3	29 / 3
p-value	0.35		0.23	
Expression of marker genes in pools of 15 hMNs				
	ChAT		**ND1 (DNA+cDNA)**	
	WT	**SOD1**	**WT**	**SOD1**
mean±SEM	15196 ±1452	14853 ± 1156	258.5 ± 23.22	232.0 ± 18.82
n / N	50 / 6	49 / 6	30 / 3	30 / 3
p-value	0.80		0.51	

3.5 Co-detection of GFAP in ChAT positive and GAD65/67 negative hMN from SOD1^{G93A} but not from WT mice.

To ensure homogeneity of laser microdissected hMN pools, each pools was tested for the expression of suitable positive and negative hMN marker gene expression, as illustrated in Figure 23. Homogeneous hMN neuronal pools should be positive for the motor neuron marker ChAT, but negative for the GABAergic neuronal markers GAD65/67 as well as the astroglia marker GFAP. This was tested by qualitative

multiplex-nested-PCR or via qPCR, using 1/3 of the hMN derived cDNA pool. This marker gene expression profile was present in 90% of hMN pools from WT mice (n=55/61). No GFAP contamination was present and 10% (6/61) showed a GAD65/67 signal for GABAergic contamination and were excluded from subsequent analysis. However surprisingly, in hMN pools from SOD1^{G93A} mice, 46% (n=39/85) of pools showed a GFAP signal via multiplex-nested-PCR (see Figure 23, right).

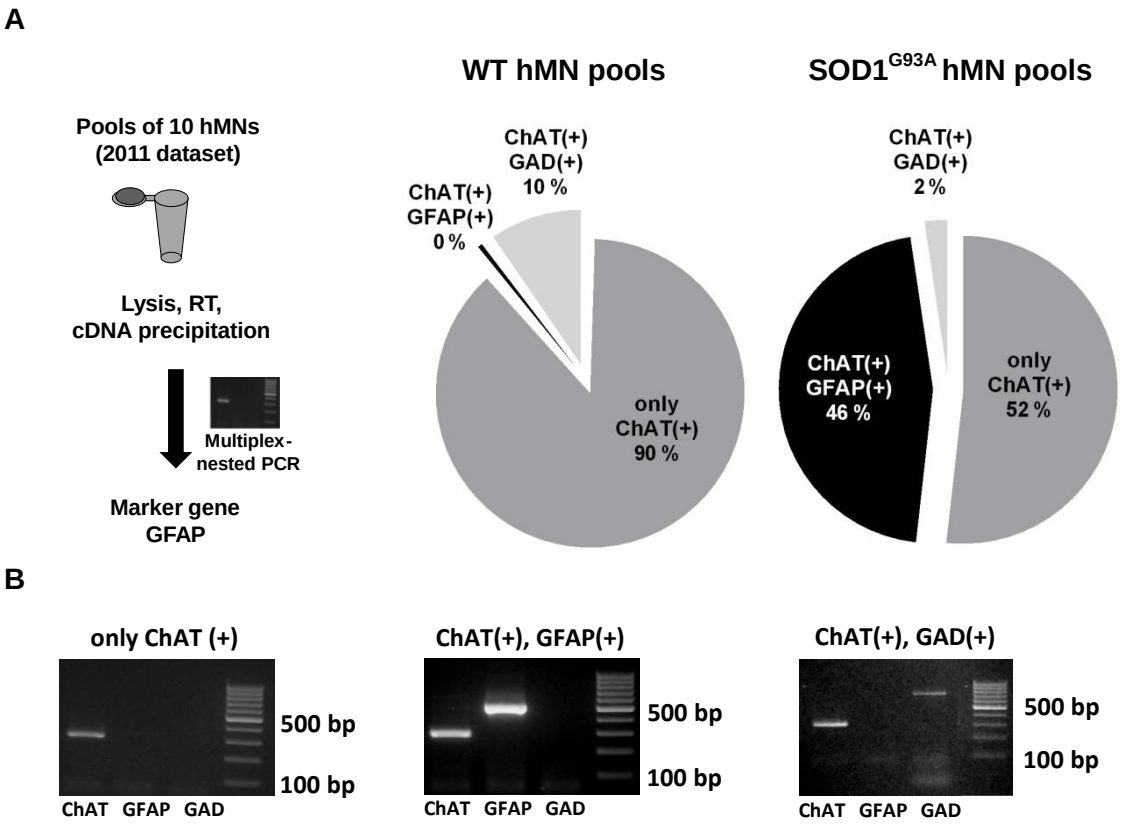

Figure 23: Evaluation of glial fibrillary acidic protein (GFAP) and glutamate decarboxylase (GAD) 65/67 in choline acetyltransferase (ChAT) positive hypoglossal motor neurons (hMNs) in SOD1^{G93A} transgenic and wildtype (WT) mice via multiplex-nested-PCR.
(A) shows distribution of marker gene signals in multiplex-nested-PCR of hMN pools for WT (left) and SOD1^{G93A} (right) mice of the 2011 dataset with either ChAT positive (gray), ChAT/GFAP coexpressing (black) and GAD65/67 contaminated (light gray) cell pools. Note that in hMN pools from WT animals, no GFAP contamination was detected, whereas 46% pools from SOD1^{G93A} transgenic animals showed GFAP. (B) shows corresponding agarose gel (2%) electrophoresis of multiplex-nested-PCR products, representative for ChAT positive (left), ChAT/GFAP coexpressing (mid) and GAD65/67 contaminated (right) cell pools. bp: base pairs. RT: reverse transcription.

To further address this unexpected finding, GFAP expression levels in pools of 15 hMNs as well as in individual hMN of WT and SOD1^{G93A} mice after UV-LMD were quantified. Again, we almost never detected any robust signal for GFAP in individual WT hMNs (n=1/9), but in all 9 tested individual hMNs from SOD1^{G93A} mice, and in 100% (n = 50) of hMN pools (GFAP qPCR expression levels are given in Table 27).

Given these results, it is very unlikely that GFAP positive hMNs, selectively in SOD1^{G93A} mice are caused artificially due to technical issues.

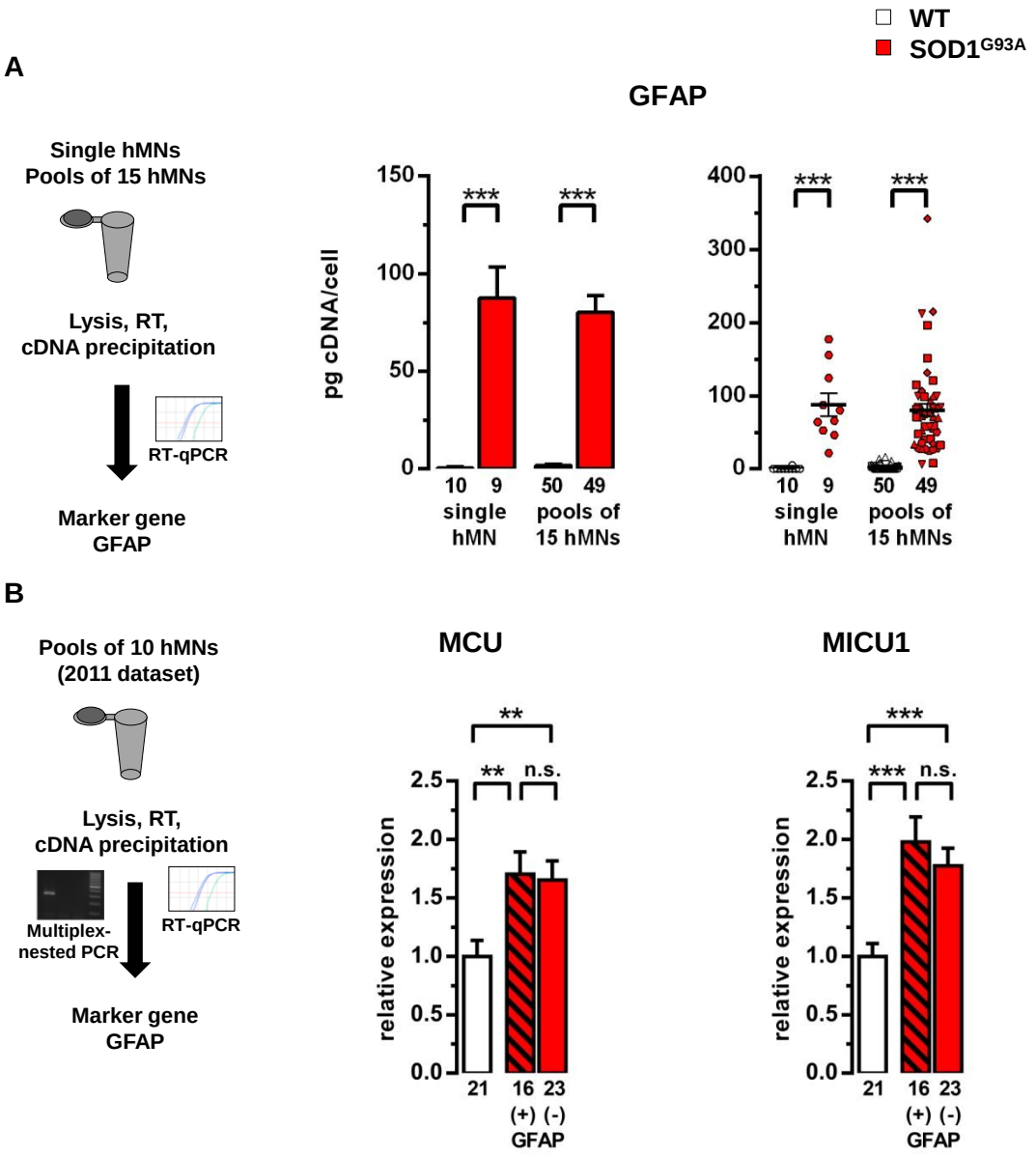

Figure 24: Evaluation of glial fibrillary acidic protein (GFAP) in choline acetyltransferase (ChAT) positive hypoglossal motor neurons (hMNs) in SOD1^{G93A} transgenic and wildtype (WT) mice via realtime quantitative PCR (RT-qPCR) (A) and influence of GFAP co-expression on expression levels of mitochondrial calcium uniporter (mCU) subunits mitochondrial calcium uniporter (MCU) and mitochondrial calcium uptake 1 (MICU1).

(A) GFAP was robustly detected in single hMNs or pools of 15 hMNs each from SOD1^{G93A}, but not from WT mice. For absolute amounts see **Table 26**

(B) Importantly, Ca^{2+} transporter expression is not influenced by co-expression of GFAP, as shown by comparison of MCU and MICU1 expression in GFAP positive (red-black striped) and negative (red) SOD1^{G93A} pools compared to WT (2011 dataset). For absolute amounts see **Table 28**

Data are shown as bargraphs illustrating the mean value ± standard error of the mean (SEM) and scatter plots, where each symbol represents either cDNA expression of single hMNs or mean individual hMN mRNA expression, derived from pools of 15 hMNs each. Number of analyzed hMN pools or individual hMNs given in bargraph. White bars/symbols represent wildtype, red bars/symbols represent SOD1^{G93A} transgenic animals. RT: reverse transcription.

Followingly, MCU and MICU1 mRNA-levels between GFAP positive and GFAP negative hMN pools of SOD1^{G93A} mice were compared, whereas no significant difference was detected (SOD1^{G93A}: relative expression; MCU: GFAP pos. 1.71±0.19, n=16; GFAP neg. 1.65±0.16, n=23; p=0.96; MICU1: GFAP pos. 1.98±0.22, n=16; GFAP neg. 1.78±0.15, n=23; p=0.51). Thus, we did not exclude GFAP positive hMN pools from further PCR analysis of Ca^{2+} transporter expression.

Table 27: Summarized mRNA expression levels and statistical analysis for glial fibrillary acidic protein (GFAP).
The values are given as mean values ± standard error of the mean (SEM). n-values represent the number of analyzed pools while N-values represent the number of analyzed mice. p-values are calculated according to the Mann-Whitney-U (MWU) test of GraphPad Prism.

Expression of GFAP in single hMNs		
	GFAP	
	WT	**SOD1**
mean±SEM	0.49 ± 0.49	87.62 ± 15.77
n / N	10 / 1	10 / 1
p-value	**<0.001*** **	
Expression of GFAP in pools of 15 hMNs		
	GFAP	
	WT	**SOD1**
mean±SEM	1.85 ± 0.50	80.38 ± 8.46
n / N	50 / 6	50 / 6
p-value	**<0.001*** **	

Table 28 shows expression levels for MCU and MICU1 in GFAP positive and negative hMN pools.

Table 28: Expression of mitochondrial calcium uniporter (MCU) and mitochondrial calcium uptake 1 (MICU1) in glial fibrillary acidic protein (GFAP) positive (+) and negative (-) pools (2011 dataset).
The values are given as mean values ± standard error of the mean (SEM) relative to the wildtype (WT) mean value. n-values represent the number of analyzed pools while N-values represent the number of analyzed mice. p-values are calculated according to the Mann-Whitney-U (MWU) test of GraphPad Prism. Note, that Ca^{2+} transporter expression is not influenced by GFAP-coexpression.

Expression of MCU and MICU1 *(2011 dataset)* in SOD1^{G93A} GFAP (+) and (-) pools relative to WT						
	MCU			**MICU1**		
	WT	**SOD1 GFAP (+)**	**SOD1 GFAP (-)**	**WT**	**SOD1 GFAP (+)**	**SOD1 GFAP (-)**
Mean ± SEM	1.00 ± 0.14	1.71 ± 0.19	1.65 ± 0.16	1.00 ± 0.11	1.98 ± 0.21	1.78 ± 0.15
n / N	21 / 4	16 / 4	23 / 4	21 / 4	16 / 4	23 / 4
p-value	(WT / SOD1 GFAP (+)) **< 0.001** (WT / SOD1 GFAP (-)) **< 0.001** (SOD1 GFAP (+) / (-)) 0.96			(WT / SOD1 GFAP (+)) **< 0.001** (WT / SOD1 GFAP (-)) **< 0.001** (SOD1 GFAP (+) / (-)) 0.51		

3.5.1 All tested mitochondrial and plasmalemma Ca^{2+} transporters are expressed in mouse hMNs with the exception of UCP3 and NCX2

After establishment of the protocol and evaluation of suitable normalization genes, it had to be probed, which of the putative mitochondrial and plasmalemmal Ca^{2+} transporters (according to the functional findings, compare 1.8 and Figure 5) are expressed in hMNs of $SOD1^{G93A}$ transgenic and WT animals. For that purpose, hMNs were first examined via qualitative PCR for putative candidate genes. Qualitative analysis showed expression of all mitochondrial and plasmalemmal Ca^{2+} transporters except UCP3 and NCX2 in ChAT and ND1 positive hMNs (n=3 pools of 15 hMNs each, see Figure 25).

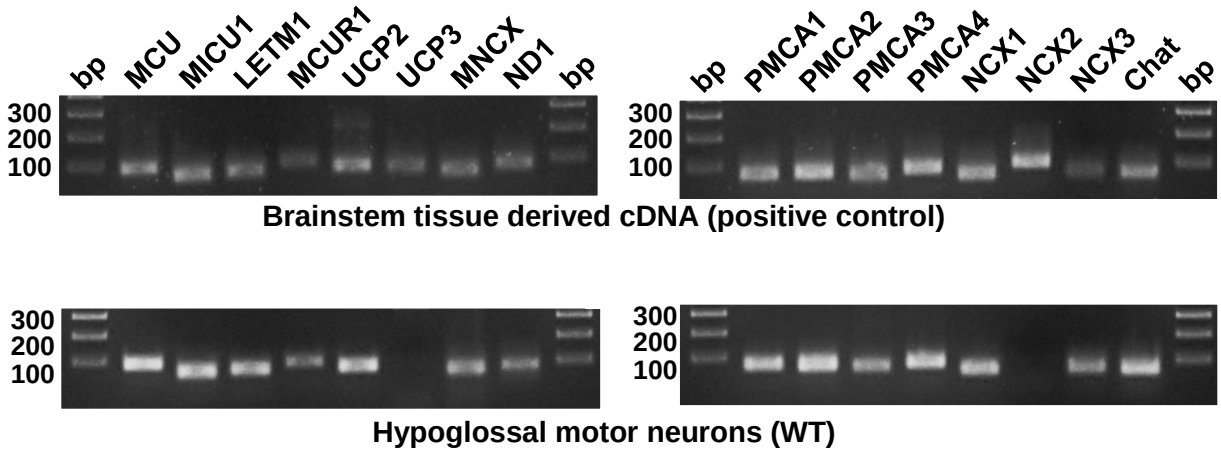

Figure 25: Expression of putative mitochondrial (left) and plasma membrane (right) calcium (Ca^{2+}) transporters in brainstem tissue derived cDNA (upper) as well as choline acetyltransferase (ChAT) and NADH dehydrogenase subunit 1 (ND1) positive hypoglossal motor neurons (hMNs) (lower).
Agarose gel (2%) electrophoresis of qualitative PCR products for brainstem tissue derived cDNA as positive control (upper) and hypoglossal motor neurons (lower). All Ca^{2+} transporters are expressed in cDNA, derived from mouse brainstem tissue (upper) while ChAT and ND1 positive hypoglossal motor neurons of wildtype and $SOD1^{G93A}$ (not shown) mice express all Ca^{2+} transporters except UCP3 and NCX2.
NCX: plasmalemmal Na^{+}/Ca^{2+} exchanger, PMCA: plasma membrane Ca^{2+} ATPase, UCP: Uncoupling protein, LETM1: Leucine zipper EF hand-containing transmembrane protein 1, MNCX: Mitochondrial sodium-Ca^{2+} exchanger, MCU: Mitochondrial Ca^{2+} uniporter, MICU1: Mitochondrial Ca^{2+} uptake 1, MCUR1: Mitochondrial Ca^{2+} uniporter regulator 1, bp: base pairs.

3.5.2 Mitochondrial Ca^{2+} uniporter (mCU) subunits show elevated mRNA levels in hMNs from $SOD1^{G93A}$ transgenic compared to WT mice

After qualitative assessment of Ca^{2+} transporter expression in hMNs, quantification of MCU and MICU1, both subunits of the mitochondrial Ca^{2+} uniporter (mCU) was performed (2011 dataset). A transcriptional down-regulation of one or both mCU subunits would provide a possible explanation for the functionally reported reduced transport capacity of mCU (compare 1.8). However, both genes showed significantly

elevated expression in hMNs of SOD1^{G93A} mice, with MICU1 levels being ~1.85-fold and MCU levels being ~1.65-fold higher, respectively (Figure 26). A similar fold-difference was detected for both genes in the second (2012) dataset, performed with another mouse cohort, which were bred in the mouse facility of the ulm university (see below).

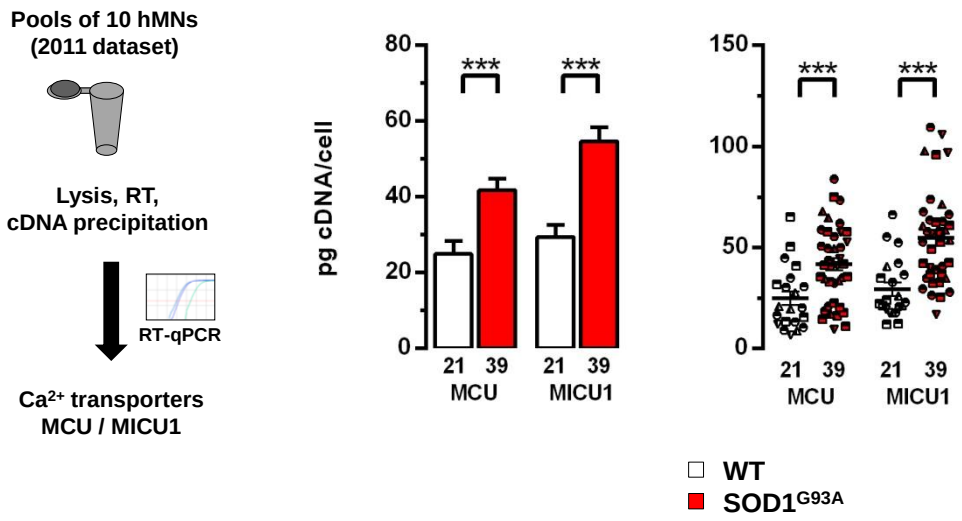

Figure 26: Realtime quantitative (RT-qPCR) data of mitochondrial Ca^{2+} transporters mitochondrial calcium uniporter (MCU) and mitochondrial calcium uptake 1 (MICU1) (2011 dataset).
Please note the significantly elevated MCU and MICU1 levels in hMNs of SOD1^{G93A} mice.
For absolute amounts see **Table 29**. Data are shown as bargraphs illustrating the mean value ± standard error of the mean (SEM) and scatter plots, where each symbol represents expression derived from a pool of 10 hMNs each. Number of analyzed hMN pools given in bargraph. White bars/symbols represent wildtype, red bars/symbols represent SOD1^{G93A} transgenic animals. WT: wildtype. RT: reverse transcription

Table 29 summarizes the expression data of MCU and MICU1 in the 2011 dataset.

Table 29: Summarized mRNA expression levels and statistical analysis for mitochondrial calcium uniporter (MCU) and mitochondrial calcium uptake 1 (MICU1) according to 2011 dataset.
The values are given as mean values ± standard error of the mean (SEM). n-values represent the number of analyzed pools while N-values represent the number of analyzed mice. p-values are calculated according to the Mann-Whitney-U (MWU) test of GraphPad Prism. WT: wildtype.SOD1: SOD1^{G93A} transgenic. MWU: Mann-Whitney-U test.

mRNA levels of MCU and MICU1 *(2011 dataset)*				
	MCU		**MICU1**	
	WT	**SOD1**	**WT**	**SOD1**
Mean ± SEM	24.95 ± 3.40	41.80 ± 3.06	29.43 ± 3.23	54.68 ± 3.68
n / N	21 / 4	39 / 4	21 / 4	39 / 4
p-value (MWU)	**< 0.001**		**< 0.001**	

3.5.3 Not only mitochondrial Ca^{2+} uniporter subunits MCU and MICU1 show elevated mRNA levels in hMNs from $SOD1^{G93A}$ compared to WT mice, but also mitochondrial Ca^{2+} transporters LETM1 and UCP2

After identifying a possibly compensatory upregulation of two components of the mitochondrial uniporter, MCU and MICU1, the aim was to further clarify the underlying molecular mechanism of the functionally identified Ca^{2+} uptake deficit in endstage $SOD1^{G93A}$ hMNs. Accordingly, mRNA-levels for all previously identified (compare Figure 25) mitochondrial and plasma membrane Ca^{2+} transporters were quantified via qPCR in hMNs from WT and endstage $SOD1^{G93A}$ mice. Results for mitochondrial candidate genes are given in Figure 27 and Table 30. Without cell-specific normalization, significantly higher mRNA levels of only MICU1 and UCP2 were identified in hMNs from $SOD1^{G93A}$ mice (each about 1.7-fold higher compared to WT). All other Ca^{2+} transporter mRNA-levels were not significantly altered (although trends were observed in particular for MCU and LETM1).

For mitochondrial Ca^{2+} transporters, normalization should be performed to the number of mitochondrial genomes, represented by ND1 expression levels. As mentioned above, there were no significant differences in expression levels of ND1 mRNA and DNA between hMNs of WT and $SOD1^{G93A}$ mice, making this gene suitable for normalization (see 3.4). Accordingly, cell-specific normalization of hMN qPCR data for mitochondrial Ca^{2+} transporters to mitochondrially encoded ND1 DNA-levels (and thus to respective hMN mitochondrial genome numbers) revealed significantly higher mRNA levels not only of MICU1 and UCP2, but also of MCU and LETM1 in hMNs from $SOD1^{G93A}$ mice (each about 1.8-fold higher compared to WT), while levels of MCUR1 and MNCX were not altered (Figure 27 and Table 30).

Expression levels of mitochondrial Ca^{2+} transporters

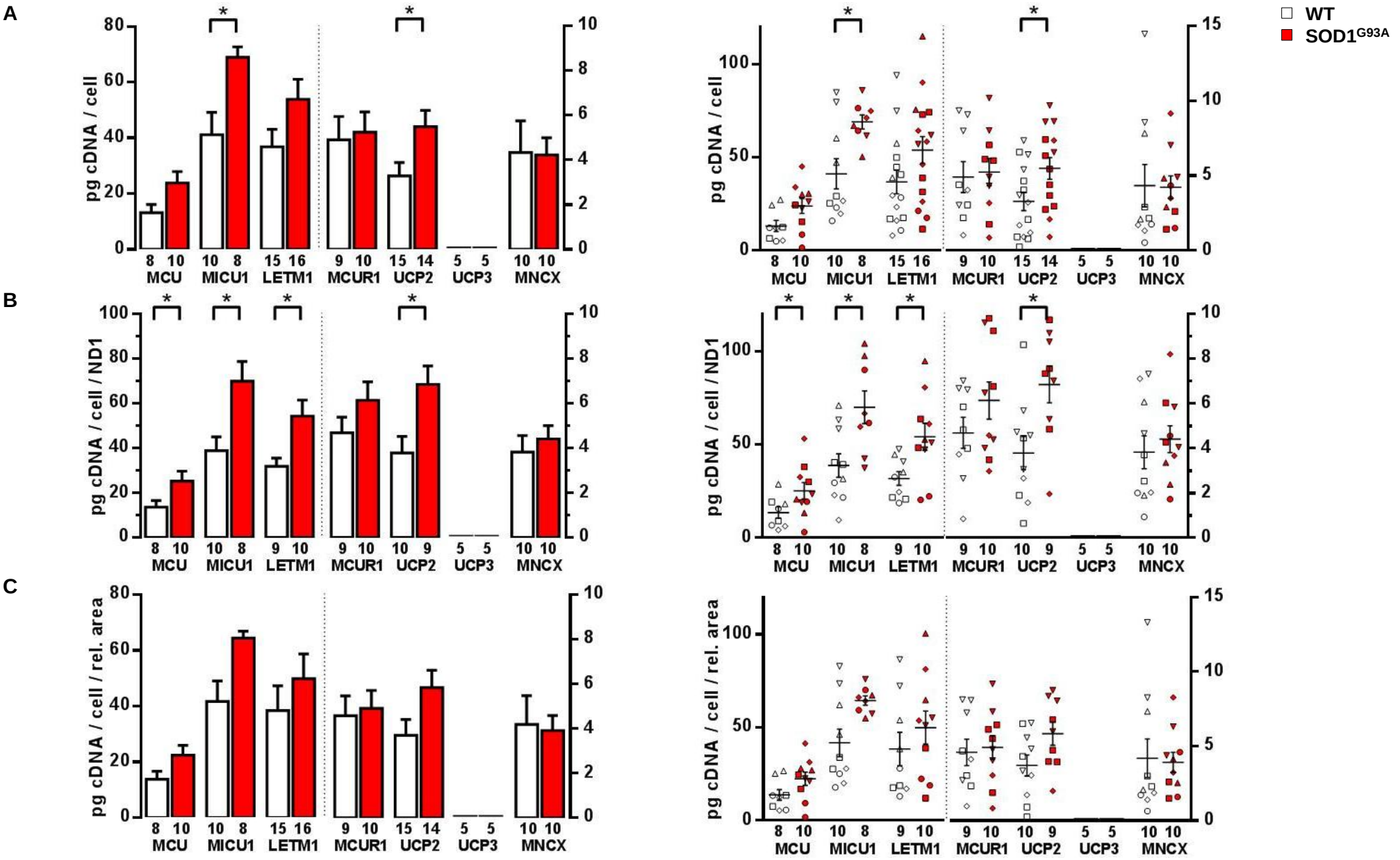

Figure 27: Realtime quantitative PCR data of mitochondrial calcium (Ca^{2+}) transporters in hypoglossal motor neurons of wildtype (WT, white) and SOD1^{G93A} (red) mice.
Please note elevated levels of MCU (normalized, B), MICU1, LETM1 (normalized, B) and UCP2 in hMNs of SOD1^{G93A} mice. Data are shown as bargraphs illustrating the mean value ± standard error of the mean (SEM) and scatter plots, where each symbol represents a pool of 15 cells. Data are given as [pg/cell] in respect to a cDNA standard curve, generated from WT mouse brainstem tissue (A). Data from (A) were normalized to mitochondrially coded ND1 DNA-levels of the respective pool (B) and to relative cell areas (C). The numbers below the graphs represent the number of analyzed cDNA pools. Significant differences were tested via the Mann-Whitney-U test. UCP: Uncoupling protein, LETM1: Leucine zipper EF hand-containing transmembrane protein 1, MNCX: Mitochondrial sodium-Ca^{2+} exchanger, MCU: Mitochondrial Ca^{2+} uniporter, MICU1: Mitochondrial Ca^{2+} uptake 1, MCUR1: Mitochondrial Ca^{2+} uniporter regulator 1, ND1: NADH dehydrogenase subunit 1.

3.5.4 From all analyzed plasma membrane Ca^{2+} transporters, only NCX1 displayed elevated mRNA levels in hMNs from $SOD1^{G93A}$ animals compared to WT

In this study, all plasmalemmal genes should be normalized to the cell pool size. However, as shown in Table 25, recorded cell areas of $SOD1^{G93A}$ hMNs were significantly larger than of WT hMNs. Therefore, the gene for choline-acetyltransferase was probed as a normalization gene for plasmalemmal Ca^{2+} transporters. As described in 3.4, ChAT levels were homogenous for hMNs of WT and $SOD1^{G93A}$ mice, making this gene suitable for normalization. After cell-specific normalization of hMN qPCR data for all analyzed plasma membrane Ca^{2+} transporters to relative ChAT levels (and thus to respective hMN cell-sizes), about 1.7-fold higher mRNA-levels, selectively of NCX1 in hMN from $SOD1^{G93A}$ mice compared to WT were detected (Table 30 and Figure 28). All other tested plasma membrane Ca^{2+} transporters (PMCA1-4 and NCX3) were not altered in hMNs from $SOD1^{G93A}$ mice compared to those of WT.

Expression levels of plasma membrane Ca^{2+} transporters

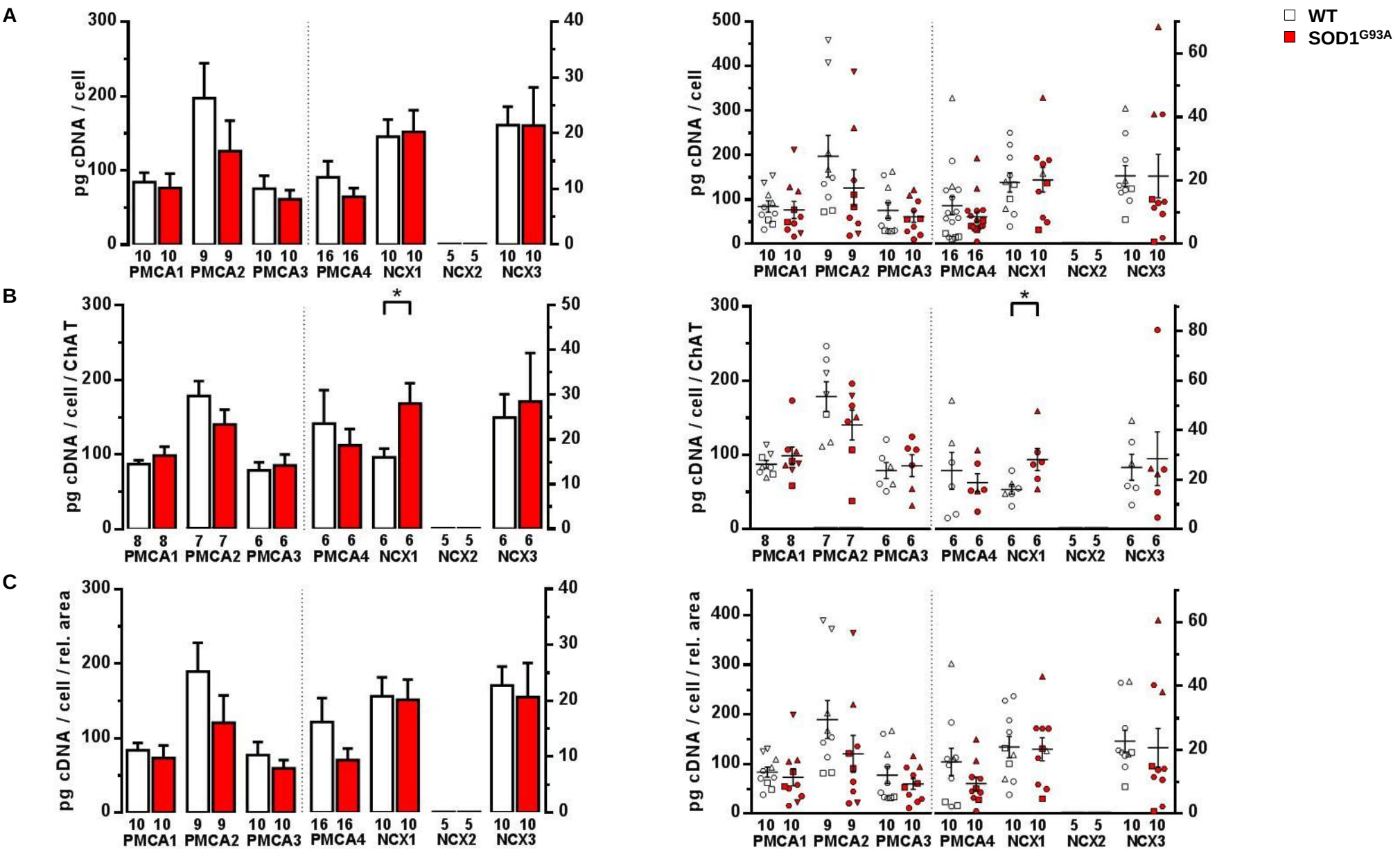

Figure 28: Realtime quantitative PCR data of plasma membrane calcium (Ca^{2+}) transporters in hypoglossal motor neurons of wildtype (WT, white) and $SOD1^{G93A}$ (red) mice.
Please note elevated levels of NCX1 (normalized to ChAT) in hMNs of $SOD1^{G93A}$ mice. Data are shown as bargraphs illustrating the mean value ± standard error of the mean (SEM) and scatter plots, where each symbol represents a pool of 15 cells. Data are given as [pg/cell] in respect to a cDNA standard curve, generated from WT mouse brainstem tissue (A). Data from (A) were normalized to relative ChAT expression of the respective pool (B) and to relative cell areas (C). The numbers below the graphs represent the number of analyzed cDNA pools. Significant differences were tested via the Mann-Whitney-U test. NCX: sodium-Ca^{2+} exchanger, PMCA: plasma membrane Ca^{2+} ATPase, ChAT: Choline acetyltransferase.

Table 30: Summarized realtime quantitative PCR results and statistical analysis for expression profiling of mitochondrial and plasmalemmal calcium (Ca^{2+}) transporters in hypoglossal motor neurons (hMNs) from wildtype (WT) and SOD1^{G93A} mice.

mRNA levels of all mitochondrial and plasma membrane Ca^{2+} transporters quantified in hypoglossal motor neurons of wildtype (WT) and SOD1^{G93A} (SOD1) mice from **Figure 27** and **Figure 28** are summarized in this table. The values are given as mean values ± standard error of the mean (SEM). n-values represent the number of analyzed pools while N-values represent the number of analyzed mice. p-values are calculated according to the Mann-Whitney-U (MWU) test of GraphPad Prism. NCX: plasmalemmal Na^{+}/Ca^{2+} exchanger, PMCA: plasma membrane Ca^{2+} ATPase, UCP: Uncoupling protein, LETM1: Leucine zipper EF hand-containing transmembrane protein 1, MNCX: Mitochondrial sodium-Ca^{2+} exchanger, MCU: Mitochondrial Ca^{2+} uniporter, MICU1: Mitochondrial Ca^{2+} uptake 1, MCUR1: Mitochondrial Ca^{2+} uniporter regulator 1, ChAT: Choline acetyltransferase, ND1: NADH dehydrogenase subunit 1.

mRNA levels of *mitochondrial* Ca^{2+} transporters														
	MCU		**MICU1**		**LETM1**		**MCUR1**		**UCP2**		**UCP3**		**MNCX**	
	WT	**SOD1**	**WT**	**SOD1**	**WT**	**SOD1**	**WT**	**SOD1**	**WT**	**SOD1**	**WT**	**SOD1**	**WT**	**SOD1**
mean±SEM	13.17±2.98	23.88±4.00	41.18±8.02	68.90±3.80	36.78±6.32	53.89±7.13	4.90±1.03	5.24±0.90	3.27±0.61	5.48±0.73	-	-	4.33±1.42	4.22±0.77
n / N	8 / 4	10 / 5	10 / 5	8 / 4	15 / 6	16 / 6	9 / 3	10 / 3	15 / 4	14 / 4	5 / 2	5 / 2	10 / 5	10 / 5
p-value	0.08		**0.03**		0.08		0.70		**0.03**		-		0.47	
mRNA levels of *mitochondrial* Ca^{2+} transporters normalized to relative mitochondrial genome count (ND1)														
	MCU		**MICU1**		**LETM1**		**MCUR1**		**UCP2**		**UCP3**		**MNCX**	
	WT	**SOD1**	**WT**	**SOD1**	**WT**	**SOD1**	**WT**	**SOD1**	**WT**	**SOD1**	**WT**	**SOD1**	**WT**	**SOD1**
mean±SEM	13.57±2.98	25.29±4.41	38.79±6.28	69.95±8.80	31.86±3.64	54.25±7.26	4.69±0.70	6.13±0.83	3.79±0.74	6.85±0.82	-	-	3.83±0.74	4.41±0.60
n / N	8 / 4	10 / 5	10 / 5	8 / 4	9 / 5	10 / 5	9 / 3	10 / 3	10 / 3	9 / 3	5 / 2	5 / 2	10 / 5	10 / 5
p-value	**0.04**		**0.02**		**0.01**		0.39		**0.01**		-		0.39	
mRNA levels of *mitochondrial* Ca^{2+} transporters normalized to relative cell size														
	MCU		**MICU1**		**LETM1**		**MCUR1**		**UCP2**		**UCP3**		**MNCX**	
	WT	**SOD1**	**WT**	**SOD1**	**WT**	**SOD1**	**WT**	**SOD1**	**WT**	**SOD1**	**WT**	**SOD1**	**WT**	**SOD1**
mean±SEM	13,74±2.91	22,42±3.52	41,70±7.38	64,42±2.46	38,39±8.92	49,90±8.87	4,58±0.88	4,91±0.80	3,71±0.71	5,84±0.78	-	-	4,19±1.29	3,92±0.67
n / N	8 / 4	10 / 5	10 / 5	8 / 4	9 / 5	10 / 5	9 / 3	10 / 3	10 / 3	9 / 3	5 / 2	5 / 2	10 / 5	10 / 5
p-value	0.10		0.05		0.35		0.76		0.08		-		0.47	

mRNA levels of *plasma membrane* Ca^{2+} transporters														
	PMCA1		**PMCA2**		**PMCA3**		**PMCA4**		**NCX1**		**NCX2**		**NCX3**	
	WT	**SOD1**	**WT**	**SOD1**	**WT**	**SOD1**	**WT**	**SOD1**	**WT**	**SOD1**	**WT**	**SOD1**	**WT**	**SOD1**
mean±SEM	84.42±12.52	76.55±19.11	197.3±46.9	126.0±41.1	75.60±17.34	61.33±12.16	12.08±2.88	8.58±1.54	19.39±3.05	20.24±3.89	-	-	21.46±3.31	21.39±6.84
n / N	10 / 5	10 / 5	9 / 5	9 / 5	10 / 4	10 / 4	16 / 5	16 / 5	10 / 4	10 / 4	5 / 2	5 / 2	10 / 4	10 / 4
p-value	0.39		0.31		0.57		0.58		0.95		-		0.24	
mRNA levels of *plasma membrane* Ca^{2+} transporters normalized to relative levels of ChAT														
	PMCA1		**PMCA2**		**PMCA3**		**PMCA4**		**NCX1**		**NCX2**		**NCX3**	
	WT	**SOD1**	**WT**	**SOD1**	**WT**	**SOD1**	**WT**	**SOD1**	**WT**	**SOD1**	**WT**	**SOD1**	**WT**	**SOD1**
mean±SEM	87.15±5.32	98.53±11.90	178.4±20.1	140.2±20.2	78.76±10.82	85.28±14.58	23.56±7.45	18.69±3.66	15.99±1.96	28.07±4.48	-	-	24.89±5.24	28.47±0.79
n / N	8 / 4	8 / 4	7 / 4	7 / 4	6 / 3	6 / 3	6 / 3	6 / 3	6 / 3	6 / 3	5 / 2	5 / 2	6 / 3	6 / 3
p-value	0.43		0.46		0.68		0.68		**0.03**		-		0.79	
mRNA levels of *plasma membrane* Ca^{2+} transporters normalized to relative cell size														
	PMCA1		**PMCA2**		**PMCA3**		**PMCA4**		**NCX1**		**NCX2**		**NCX3**	
	WT	**SOD1**	**WT**	**SOD1**	**WT**	**SOD1**	**WT**	**SOD1**	**WT**	**SOD1**	**WT**	**SOD1**	**WT**	**SOD1**
mean±SEM	83,59±9.89	73,29±17.16	189,6±38.38	120.5±37.08	77,51±17.22	59,62±10.98	16,19±4.32	9,38±2.07	20,84±3.39	20,18±3.62	-	-	22,73±3.40	20,66±6.10
n / N	10 / 5	10 / 5	9 / 5	9 / 5	10 / 4	10 / 4	10 / 4	10 / 4	10 / 4	10 / 4	5 / 2	5 / 2	10 / 4	10 / 4
p-value	0.28		0.11		0.43		0.28		0.84		-		0.19	

4 Discussion

This work provides a cell-specific quantitative analysis of mitochondrial and plasma membrane Ca^{2+} transporter mRNA expression in highly vulnerable cholinergic hypoglossal motor neurons from endstage $SOD1^{G93A}$ transgenic mice compared to WT. By this means, a selective up-regulation of the mitochondrial Ca^{2+} transporters MCU/MICU1, LETM1 and UCP2 as well as of the plasma membrane Na^{+}/Ca^{2+} exchanger NCX1 in remaining hMNs in endstage $SOD1^{G93A}$ was identified, while cDNA and genomic DNA levels for the mitochondrially coded ND1 gene, as well as cDNA levels for ChAT, the key enzyme for acetylcholine-synthesis, were not altered.

4.1 Methodological aspects

4.1.1 $SOD1^{G93A}$ mice and emerging animal models of ALS

Although early pathogenesis might differ, there is a considerable clinical and pathological overlap in later stages of disease of mutant SOD1 dependent and independent ALS. Of all animal models, the clinical picture of SOD1 transgenic animals (including sparing of the eye movements) still fits best to symptom onset and time course of human ALS patients (McGoldrick et al. 2013). Signs of most key pathogenic features like oxidative stress, excitotoxicity and mitochondrial dysfunction have been seen in both, SOD1 mouse models and human ALS patients, with considerable accordance down to the detail (Redler and Dokholyan 2012). A link between SOD1 pathology and sporadic ALS cases was found recently, when *wildtype* SOD1 was reported to show similar folding disturbances and aggregation when modified through oxidative stress (Bosco et al. 2010; Martins and English 2014). Nevertheless, problems associated with SOD1 overexpression models, most importantly the lack of transitional therapeutical success, prompted the generation of new animal models based on novel pathogenetic insights. Especially mice with mutated or overexpressed 43-kDa trans-activating response region binding protein (TDP-43) and fused in sarcoma (FUS) are increasingly being used. To date, they do not reproduce the ALS-like phenotype to the extent of SOD1 transgenic mice: TDP-43 models display mainly axonal phenotypes with mild MN cell death. In the few studies on FUS-ALS, overexpression of mutant FUS lacks MN degeneration in spinal

cord, whereas wildtype FUS overexpression caused an aggressive phenotype in homozygous but no motor pathology in hemizygous animals (McGoldrick et al. 2013). As these models are currently far from being understood, it is not surprising, that the number of pharmacologic trials is still very limited, compared to SOD1 models, and neither positive nor negative results have been published (McGoldrick et al. 2013). Very recently, a promising C9ORF72 related animal model was created, exhibiting TDP-43 pathology, neuronal loss as well as behavioral and motor deficits (Chew et al. 2015). However, given the previous functional analysis of activity dependent Ca^{2+} homeostasis in hMNs from $SOD1^{G93A}$ mice and the fact that none of the recently generated models was shown to recapitulate most aspects of human ALS as convincing as the SOD1 mutant mouse, $SOD1^{G93A}$ mice were utilized in this complementary study.

4.1.2 UV-LMD and RT- qPCR of motor neurons in ALS

UV-laser microdissection of single cells is an important tool to enlighten the process of neurodegeneration in general, as it eliminates bias of a decreased neuronal cell population, reactive astroglial proliferation and other cellular reactions compared to study of whole tissue. Thus, results yielded with both approaches can be contradictory, as it was demonstrated by our group for Parkinson's disease, where at least 70% of dopaminergic neurons are lost at disease onset (compare (Schlaudraff et al. 2014)). MN degeneration in brainstem nuclei (including the hypoglossal nucleus with ~30-35 %) and spinal cord as well as astrogliosis are present in $SOD1^{G93A}$ mice on clinical and pathological level (Zang and Cheema 2002; Haenggeli and Kato 2002; Fuchs et al. 2010; Ferrucci et al. 2010) underlining the need for a cell-specific approach. Accordingly, the number of studies using this technique is growing (compare Appendix, Table 1) although, probably due to lower cost and easier handling, a number of results based on whole tissue preparation is still published.

Selection of MN was done manually according to cell diameter (> 20-25 µm), morphology and location in the ventral part of the hypoglossal nucleus in cresyl violet stained sections without further MN-specific staining (e.g. for ChAT). A method of MN selection based on these criteria was chosen for preliminary functional experiments, where identity was spot-checked by ChAT immunochemistry (Fuchs 2013) and is also used in most UV-laser microdissection experiments (compare **Appendix, Table***)*. In

this work, MN identity was additionally confirmed by means of marker gene expression profiling (compare Figure 22), showing a general high reliability of the above-mentioned morphologic criteria.

The profiling of gene expression in ALS patients and animal models is currently performed mostly via microarray experiments that yield a huge amount of data on alteration of gene expression in various disease stages. However, these studies have their significance mostly in providing first hints on possibly involved molecular pathways and are generally complemented by more specific methods, e.g. qPCR of laser-microdissected cells. In contrast, a clear preexisting hypothesis that is e.g. based on a functional background is certainly an advantage of this study, as impairments in Ca^{2+} homeostasis during ALS disease progression are well-described for motor neurons (see 1.3.2.4). Moreover, the accordance between different microarray platforms still shows considerable differences (Pedotti et al. 2008) and the practice of publishing alterations in gene expression not below a certain cut-off might overlook more subtle, but potentially important changes.

For quantification of marker genes as well as Ca^{2+} transporters via quantitative PCR, Taqman assays were used. As primers are complemented by a sequence-specific detection probe, transcript specificity is generally enhanced in comparison to other qPCR assay types (e.g. SYBRgreen). Primer validation was done by standard curve generation and run of qPCR products on agarose gel, in accordance with the MIQE (minimum information for the publication of quantitative real-time PCR experiments) guidelines (Taylor and Mrkusich 2014).

4.2 Implications of marker gene expression analysis

For the 2011 dataset, validation of MN identity for pools of 10 cells each was done via multiplex-nested-PCR for ChAT, GAD and GFAP. Surprisingly, co-expression of astroglial marker GFAP was detected in about 46% of analyzed ChAT positive hMN cDNA pools from SOD1^{G93A} mice but never in WT in this first dataset. To further confirm this unexpected finding, in the 2012 dataset, GFAP levels as well as ChAT-levels were quantified in parallel in individual hMN neurons and in pools of 15 hMN neurons from WT and SOD1^{G93A} mice, with more sensitive RT-qPCR. Again, no robust GFAP positive signals (none up to minimal amounts) were obtained in ChAT positive WT hMNs or hMN pools but in 100% of ChAT positive individual hMNs or hMN pools from SOD1^{G93A} mice. Importantly, general technical issues (i.e. contaminations by whole glial cells) were excluded by single cell experiments, where GFAP expression was never seen in the absence of ChAT (which would correspond to a harvested glial cell).

Two possible explanations for the detected GFAP signals selectively in hMNs from SOD1^{G93A} but not WT mice are provided here: Either SOD1^{G93A} hMNs might de-differentiate or reprogram their neuronal phenotype due to the disease process, as described for other cell types (Sarthy et al. 1991; Qiang et al. 2013; Hol et al. 2003; Gao et al. 2014; Puri and Hebrok 2012; Arendt 2008), and due to this process co-express GFAP. Or alternatively, the well-described reactive astroglia cell activation and proliferation, present in ALS and other neurodegenerative diseases (Chen et al. 2012; Parpura et al. 2012; Forsberg et al. 2011; Bi et al. 2013) might change the morphological astroglia - neuron interaction, and thus, dendrites of astroglial cells might reside more closely to hMNs from SOD1^{G93A} compared to WT, and might have been partly laser microdissected together with the hMN cell bodies. Recent evidence for the latter comes from (Trias et al. 2013), who reported a toxic, highly proliferative astroglial phenotype to emerge during disease onset in SOD1^{G93A} rats, with strong association to motor neurons. However, it is important to note that no morphological evidence for this latter GFAP contamination explanation was present in UV-LMD samples from SOD1^{G93A} brains. Furthermore, respective GFAP co-expression in individual dopamine neurons from e.g. Parkinson’s disease brains, where a respective reactive gliosis also has been described ('Episcopo et al. 2013), or from

respective Parkinson's disease mouse models, in over 15 years of UV-LMD RT-qPCR analysis of individual dopamine neurons was never detected by our group (Ramirez et al. 2006; Gründemann et al. 2011; Schiemann et al. 2012; Gründemann et al. 2008; Schlaudraff et al. 2014). Thus, while general methodological issues can be ruled out, it cannot for sure be concluded that the detected GFAP signal of hMNs selectively from SOD1^{G93A} but not from WT mice is genuinely derived from hMNs, and further studies are necessary to address this point and its possible implication for ALS. However, this surprising finding further highlights the emerging crucial role of astroglia cells in ALS and its animal models (Valori et al. 2014). Indeed mutant SOD1 expression has been shown to greatly affect the astroglial functional phenotype, turning astrocytes into neurotoxic cells, altering their vital MN-supportive functions, and eventually astrocytes themselves become more prone to cell death (Valori et al. 2014).

4.3 Quantification of mitochondrial genome copy numbers

Although mitochondrial dysfunction is present in MNs in ALS as well as in SOD1^{G93A} mice (Barrett et al. 2011; Martin 2011), and macroscopic and functional alterations of mitochondria have been characterized extensively (Cozzolino and Carrì 2012; Vehviläinen et al. 2014; Kawamata and Manfredi 2010), the number of mitochondria/mitochondrial genomes in highly vulnerable MNs to our knowledge has not yet been addressed. Cell-specific ND1 data provided by this work argue against significant changes in number of mitochondria or mitochondrial genomes (at least in the cell soma) in hMNs from endstage SOD1^{G93A} mice, compared to WT. In accordance with these findings, ND2 genomic DNA levels in human *post mortem* spinal cord motor neurons of ALS patients were also not altered compared to controls, whereas mitochondrial genomic DNA-levels for mitochondrially coded cytochrome oxidase and ND4 were significantly lower in ALS (Keeney and Bennett 2010) - probably due to mitochondrial DNA deletions that occur preferentially in the ND4 gene (He et al. 2002). These deletions or mutations are likely to occur more frequently in ALS, as DNA repair enzymes in mitochondria have been shown to be impaired (Murakami et al. 2007), although the frequency of the mtDNA 5 kB common deletion in individual motor neurons in post-mortem tissue from sALS patients was only slightly elevated in spinal cord but not in other motor or non-motor regions

(Mawrin et al. 2004). However, the ND1 gene has been demonstrated to be almost never affected by those DNA deletions (He et al. 2002; Bender et al. 2006).

4.4 Quantification of Ca^{2+} transporter genes in hMNs of $SOD1^{G93A}$ and WT mice

Whenever discussing gene expression levels in ALS motor neurons, one should not forget that these cells go through various stages of degeneration and the here presented data for pools of 15 hMNs each represent mean values of a cross section ranging from viable to moribund cells. Therefore, differences in mRNA levels might generally be underestimated, especially when considering that the functional Ca^{2+} buffering phenotype was present in ~1/3 of hMN (Fuchs et al. 2013).

4.4.1 Elevated mRNA levels of MCU, MICU1, LETM1 and UCP2 in hMNs of $SOD1^{G93A}$ and WT mice

Functional disturbances in mitochondrial uptake of cytosolic Ca^{2+} have been recurrently reported in the context of ALS in the past years. Importantly, Fuchs et al could recently demonstrate, that mitochondrial Ca^{2+} uptake deficit in hMNs of $SOD1^{G93A}$ mice occurs in vulnerable hypoglossal, but not in resistant oculomotor motor neurons and selectively at the endstage of disease. More precisely, in these vulnerable hMN of $SOD1^{G93A}$ mice under high-Ca^{2+} loading conditions, mCU-mediated mitochondrial Ca^{2+} uptake was reduced together with an increase of Ca^{2+} extrusion across the plasma membrane (Fuchs et al. 2013) (Appendix, Figure, left). The present molecular analysis points to a complex underlying mechanism for this functional hMN phenotype in $SOD1^{G93A}$ mice, as mRNA-levels of the mCU core components MCU and MICU1 were about 1.7-fold higher in hMN from $SOD1^{G93A}$ mice. Increased MCU expression might enforce metabolic coupling, as mitochondrial Ca^{2+} activates e.g. enzymes of the tricarboxylic acid cycle (McCormack and Denton 1990; Wiederkehr et al. 2011) while simultaneous MICU1 upregulation is important to prevent a harmful constant Ca^{2+} leakage into mitochondria at resting conditions (Mallilankaraman et al. 2012b). On the other hand, overexpression of MCU can sensitize cells to apoptotic stimuli (Stefani et al. 2011). Thus, mCU up-regulation might provide in first instance a compensatory mechanism to maintain function of

diseased hMNs in SOD1^{G93A} mice. Accordingly, these mechanisms were seen in neurons that survived until a very late disease stage. In the end however, dysregulation of mCU components might contribute to neurodegenerative ALS pathology by promoting hMN death. It is noteworthy that mRNA-levels of another regulatory mCU subunit MCUR1 were not altered in hMNs from SOD1^{G93A} mice, thus the stoichiometry and thus general function of mCU might also be altered in hMNs from SOD1^{G93A} mice. In this context, additional mCU components have recently been identified (Marchi and Pinton 2014), like EMRE and MICU2, which regulate MCU/MICU1 activity (Ahuja and Muallem 2014; Kamer and Mootha 2014; Foskett and Madesh 2014), that need to be analyzed in further studies.

In addition to elevated MCU/MICU1 levels similarly elevated levels for LETM1 as well as for UCP2 mRNA in hMN from SOD1^{G93A} mice were detected, while UCP3 mRNA was neither detected in hMNs from WT nor from transgenes. LETM1 is regarded as a highly Ca^{2+} sensitive mitochondrial Ca^{2+}/H^{+} exchanger, operating mainly at cytosolic Ca^{2+} levels below 1 µM (Jiang et al. 2009; Waldeck-Weiermair et al. 2011). As significant mitochondrial Ca^{2+} uptake via the mCU becomes apparent particularly at cytosolic Ca^{2+} concentrations not below 5-10µm (Rizzuto and Pozzan 2006; Marchi and Pinton 2014) a concerted up-regulation of mCU and LETM1 might effectively buffer pathophysiologically complex, activity dependent, altered cytosolic Ca^{2+} levels in SOD1^{G93A} mice, and thereby promote hMN survival. This complex view is further supported by the detected elevated levels of UCP2 in hMNs from SOD1^{G93A} mice. In addition to the proposed mediated direct mitochondrial Ca^{2+} uptake, UCP2 acts as mitochondrial uncoupling protein, and thus decreases the amount of reactive oxygen species produced by a steep proton gradient of the respiratory chain (Donadelli et al. 2014). This mild uncoupling has been shown to be neuroprotective in highly vulnerable dopamine neurons in mouse models of Parkinson’s disease (Liss et al. 2005; Guzman et al. 2010). However, overexpression of human UCP2 in SOD1^{G93A} mice paradoxically accelerated disease progression and further reduced mitochondrial Ca^{2+} uptake capacity (Peixoto et al. 2013). The authors conclude, that in bio-energetically defective mitochondria of SOD1^{G93A} mice, UCP2 might have adverse effects, possibly by enhancing sensitivity to Ca^{2+} induced depolarization of mitochondria and/or interacting with other Ca^{2+} uptake pathways.

Further possible explanations for a reduced mitochondrial Ca^{2+} uptake in the presence of elevated mRNA-levels of Ca^{2+} transporters comprise post-translational deficits in synthesis, maturation and mitochondrial import of these proteins (Li et al. 2010) or mislocalization of mitochondria themselves in relation to Ca^{2+} sources, e.g. the endoplasmic reticulum (Magrané and Manfredi 2009; Tadic et al. 2014). Appendix, Figure summarizes and opposes the functional and molecular alterations of cytosolic Ca^{2+} clearance in hMNs.

4.4.2 Elevated mRNA levels of NCX1 in hMNs of SOD1^{G93A} and WT mice

In accordance with the functional phenotype, mRNA-levels of the plasma membrane Na^+/Ca^{2+} exchanger NCX1 were about 1.7-fold higher in hMNs from SOD1^{G93A} mice, while NCX2 was not expressed, and NCX3 as well as PMCA1-4 mRNA-levels were not altered. The lack of NCX2 mRNA detection in hMNs from WT as well as from SOD1^{G93A} mice is somewhat surprising, since this isoform was attributed a key role in neuronal Ca^{2+} homeostasis (Brini and Carafoli 2011). The low-affinity/high-capacity Ca^{2+} transporter NCX is believed to mediate the bulk of plasma membrane Ca^{2+} export after stimulation, rather than the PMCAs (Brini and Carafoli 2011; Sharma and O'Halloran 2014). Moreover, NCXs are controlled by cytosolic concentrations of Na^+ and Ca^{2+} (Brini and Carafoli 2011), thus the observed increased functional plasma membrane Ca^{2+} extrusion is likely caused by an enhanced NCX1 expression, accompanied by an enhanced functional NCX transport capacity, due to pathologically elevated cytosolic Ca^{2+} and a reduced mitochondrial Ca^{2+} buffer capacity in hMNs from endstage SOD1^{G93A} mice. It is noteworthy, that for NCX1, allosteric regulation by Ca^{2+} and response kinetics depend significantly on expressed isoforms/splice variants (Dunn et al. 2002) and might not have been detected by our primers. A further important property of NCXs in general is their sensitivity to mild cytosolic acidification under acidosis or ischemic conditions where Ca^{2+} binding regulatory domains have shown to function as a dual Ca^{2+}/pH sensor (DiPolo and Beaugé 2006; Boyman et al. 2011). Up-regulation of NCX1 appears under pathologic conditions in excitable tissues, e.g. end-stage heart disease, where it may contribute to altered excitation-contraction coupling and arrythmogenesis (Xu et al. 2006). On the other hand there is strong evidence for a neuroprotective role of NCX1 in response to ischemic events, that are characterized by progressive Na^+ and, in later phases, Ca^{2+} overload, where upregulation or pharmacological activation reduced

brain damage (Pignataro et al. 2012; Boscia et al. 2006). Selective modulation of NCX1 to alleviate cytosolic Ca^{2+} loads and excitotoxic damage in degenerating motor neurons might thus be of therapeutic value for treatment of ALS.

PMCAs are also stimulated by Ca^{2+} via calmodulin or phosphorylation (Strehler 2013; Lopreiato et al. 2014). As specific PMCA splice variants differ e.g. in their affinity and reaction upon calmodulin binding (Strehler 2013; Brini et al. 2013), an pathologic shift in PMCA splice variants might also contribute to enhanced plasma membrane Ca^{2+} extrusion in hMN from $SOD1^{G93A}$ mice. It is noteworthy in this context, that our PMCA TaqMan assays are detecting but not discriminating distinct PMCA splice variants. To date, functional studies of plasma membrane Ca^{2+} transporters are hampered by lack of specific pharmacology which makes it difficult to address the distinct contributions of individual NCX- or PMCA-isoforms (Strehler 2013).

4.5 Outlook

This study provides novel molecular and cell-specific insights into the complex nature of cytosolic Ca^{2+} dysregulation and mitochondrial dysfunction in highly vulnerable hMNs in the most common ALS mouse model, the endstage $SOD1^{G93A}$ mice (illustrated in Appendix, Figure 1). The detected concerted up-regulation of distinct mitochondrial and plasma membrane Ca^{2+} transporters with different intracellular locations as well as transport kinetics (MCU/MICU1, LETM1, UCP2, NCX1) might serve as a complex compensatory response to the disease trigger and to the altered Ca^{2+} homeostasis, and protect hMNs in $SOD1^{G93A}$ mice from degeneration. In the short run, it might adapt subcellular coupling of Ca^{2+} levels to higher metabolic demands of (external) excitotoxic stress. However, in the long run, it might not be sufficient to effectively lower cytosolic Ca^{2+} levels, or it could even contribute to cytosolic Ca^{2+} overload and MN degeneration (like shown for UCP2).

For a further clarification of causes and consequences, in a next step, a molecular analysis of hMNs from pre-symptomatic (P70) animals should be performed to attribute the gene expression changes to the respective disease stages. Furthermore, it must be clarified, whether the reported transcriptional dysregulation occurs selectively in vulnerable motor neurons or if it might be present in all motor neurons of $SOD1^{G93A}$ mice, by performing expression analysis of Ca^{2+} transporters in

motor neurons that are more resistant to the disease process in ALS (e.g. those of the oculomotor nucleus). Functional findings already suggest an intact mitochondrial Ca^{2+} clearance in these resistant motor neurons (Fuchs 2013), thus identification of differentially expressed Ca^{2+} transporters might help to clarify, which of them are more likely to have a protective or harmful effect.

Moreover, as it became clear in the last years, that some characteristics of SOD1 related ALS pathology are absent in the majority of fALS and sALS cases, a similar analysis of cell specific functional and molecular analysis of motor neurons should be analyzed in other ALS mouse models (e.g. TDP-43, FUS or C9ORF72) in view of a "converging common pathway".

Finally, most important for all animal model studies, is the transition of mouse model findings to the human disease. Thus we have already obtained snap-frozen hMN- and oMN-containing *post mortem* tissue from ALS and control patients (3 and 10 brains), collected by Prof. Thal and Prof. Ludolph, Ulm University. We plan to quantify Ca^{2+} transporter mRNA levels as well as those of the marker genes ChAT and GFAP in highly vulnerable and more resistant motor neurons from ALS patients and controls by combining UV-LMD and RT-qPCR approaches, as here described for mice.

5 Summary

Amyotrophic lateral sclerosis (ALS) is a neurodegenerative disease affecting particularly cholinergic motor neurons (MN) of the motor cortex, the brainstem and the spinal cord, and leading to paralysis and atrophy of the innervated muscles. Most patients die within two to four years after onset of the first symptoms. Glutamate excitotoxicity, associated disturbances in calcium (Ca^{2+}) homeostasis and mitochondrial dysfunction have emerged as major pathogenic features in familial as well as sporadic forms of ALS. However, the distinct molecular pathology, in particular the cause for the differential vulnerability of different motor neuron subtypes to disease triggers, remains unclear. Recently, in a common ALS model, the endstage superoxide dismutase 1 ($SOD1^{G93A}$) transgenic mouse, an activity-dependent, complex Ca^{2+} clearance deficit, present selectively in highly vulnerable motor neurons of the hypoglossal nucleus (hMNs) was described by our group. This functional deficit was defined by a reduced mitochondrial Ca^{2+} uptake and an elevated Ca^{2+} extrusion across the plasma membrane, selectively in hMNs of endstage $SOD1^{G93A}$ mice, while Ca^{2+} clearance via the endoplasmic reticulum (ER) remained preserved.

To address the underlying molecular mechanisms, I (1) transferred an established combined ultraviolett laser microdissection (UV-LMD) and realtime quantitative polymerase chain reaction (RT-qPCR) protocol for cell specific messenger RNA (mRNA) quantification of individual neurons from mouse midbrain sections to a respective mouse brainstem preparation and hypoglossal motor neurons from adult wildtype (WT) and $SOD1^{G93A}$ mice and (2) established suitable primers to analyze expression levels of respective mitochondrial (mitochondrial calcium uniporter (MCU), mitochondrial calcium uptake 1 (MICU1), mitochondrial calcium uniporter regulator 1 (MCUR1), leucine zipper EF-hand containing transmembrane protein 1 (LETM1), uncoupling proteins 2 and 3 (UCP2, UCP3), mitochondrial sodium-calcium exchanger (MNCX)) and plasma membrane Ca^{2+} transporters (sodium-calcium exchanger 1-3 (NCX1-3), plasma membrane calcium ATPase (PMCA 1-4)) in individual, choline-acetyltransferase (ChAT) positive hMNs from wildtype and endstage $SOD1^{G93A}$ mice. In addition (3), to further stratify single cell UV-LMD RT-qPCR data derived from mouse hMNs, suitable normalization strategies were tested

(normalization to cell size, as well as to the cytosolic marker gene ChAT and the mitochochondrial marker gene NADH dehydrogenase 1 (ND1). And finally (4), I compared with this optimized protocol mRNA expression levels of mitochondrial and plasma membrane Ca^{2+} transporters in individual hMNs from endstage $SOD1^{G93A}$ and WT mice.

With this optimized method I found (1) that ChAT as well as ND1 mRNA levels are similar in hMNs from $SOD1^{G93A}$ and WT mice. This indicates (i) that neither neurotransmitter synthesis nor number of mitochondria/mitochondrial genoms is altered in hMNs of endstage SOD1 mice, and (ii) that ChAT as well as ND1 mRNA levels are suitable for normalization of RT-qPCR data derived from mouse hMNs. I also found that (2) all tested Ca^{2+} transporters but UCP3 and NCX2 were expressed in mouse hMNs. Furthermore (3), with cell specific normalization of RT-qPCR data for mitochondrial Ca^{2+} transporters to ND1 and plasmalemmal Ca^{2+} transporters to ChAT, I detected about 2-fold higher mRNA levels of the mitochondrial Ca^{2+} transporters MCU/MICU1, LETM1, and UCP2 in remaining hMNs from endstage $SOD1^{G93A}$ mice. These higher expression-levels of mitochondrial Ca^{2+} transporters in individual hMNs were not associated with a respective increase in number of mitochondrial genomes, as evident from hMN specific ND1 DNA quantification. In addition (4), normalized mRNA-levels for the plasma membrane Na^{+}/Ca^{2+} exchanger NCX1 were also about 2-fold higher in hMNs from $SOD1^{G93A}$ mice. This concerted up-regulation of distinct mitochondrial and plasma membrane Ca^{2+} transporters with different locations as well as transport kinetics might serve as a complex compensatory response to the disease trigger and to the altered Ca^{2+} homeostasis, and protect surviving hMNs in $SOD1^{G93A}$ mice from degeneration. Thus, pharmacological stimulation of Ca^{2+} transporters in highly vulnerable hMNs might offer a neuroprotective strategy for ALS. However further studies a necessary to address cell specific causes and consequences of altered Ca^{2+} transporter activity in motor neurons – in mouse models and, most important, in human motor neurons from ALS patients and controls.

6 Publication bibliography

1. Ahuja, Malini; Muallem, Shmuel: The gatekeepers of mitochondrial calcium influx: MICU1 and MICU2. EMBO reports 15: 205–206 (2014).

2. Amador, Fernando J.; Stathopulos, Peter B.; Enomoto, Masahiro; Ikura, Mitsuhiko: Ryanodine receptor calcium release channels: lessons from structure-function studies. The FEBS journal 280: 5456–5470 (2013).

3. Angenstein, Frank; Niessen, Heiko G.; Goldschmidt, Jürgen; Vielhaber, Stefan; Ludolph, Albert C.; Scheich, Henning: Age-dependent changes in MRI of motor brain stem nuclei in a mouse model of ALS. Neuroreport 15: 2271–2274 (2004).

4. Arendt, T. (2008): Differentiation and De-Differentiation—Neuronal Cell-Cycle Regulation During Development and Age-Related Neurodegenerative Disorders. In Abel Lajtha, J. Regino Perez-Polo, Steffen Rossner (Eds.): Handbook of Neurochemistry and Molecular Neurobiology. Boston, MA: Springer US: 157–213.

5. Arikawa, Emi; Sun, Yanyang; Wang, Jie; Zhou, Qiong; Ning, Baitang; Dial, Stacey L.; Guo, Lei; Yang, Jingping: Cross-platform comparison of SYBR Green real-time PCR with TaqMan PCR, microarrays and other gene expression measurement technologies evaluated in the MicroArray Quality Control (MAQC) study. BMC Genomics 9: 328 (2008).

6. Ash, Peter; Bieniek, Kevin F.; Gendron, Tania F.; Caulfield, Thomas; Lin, Wen-Lang; DeJesus-Hernandez, Mariely; van Blitterswijk, Marka M; Jansen-West, Karen; Paul, Joseph W.; Rademakers, Rosa; Boylan, Kevin B.; Dickson, Dennis W.; Petrucelli, Leonard: Unconventional translation of C9ORF72 GGGGCC expansion generates insoluble polypeptides specific to c9FTD/ALS. Neuron 77: 639–646 (2013).

7. Bakkar, Nadine; Boehringer, Ashley; Bowser, Robert: Use of biomarkers in ALS drug development and clinical trials. Brain Research 1607: 94–107 (2015).

8. Barber, Siân C.; Shaw, Pamela J.: Oxidative stress in ALS: Key role in motor neuron injury and therapeutic target. Free Radical Biology and Medicine 48: 629–641 (2010).

9. Barrett, Ellen F.; Barrett, John N.; David, Gavriel: Mitochondria in motor nerve terminals: function in health and in mutant superoxide dismutase 1 mouse models of familial ALS. Journal of bioenergetics and biomembranes 43: 581–586 (2011).

10. Barrett, Paul J.; Timothy Greenamyre, J.: Post-translational modification of α-synuclein in Parkinson's disease. Brain Research 1628: 247–253 (2015).

11. Baughman, Joshua M.; Perocchi, Fabiana; Girgis, Hany S.; Plovanich, Molly; Belcher-Timme, Casey A.; Sancak, Yasemin; Bao, X. Robert; Strittmatter, Laura; Goldberger, Olga; Bogorad, Roman L.; Koteliansky, Victor; Mootha, Vamsi K.: Integrative genomics identifies MCU as an essential component of the mitochondrial calcium uniporter. Nature 476: 341–345 (2011).

12. Bellingham, Mark C.: A review of the neural mechanisms of action and clinical efficiency of riluzole in treating amyotrophic lateral sclerosis: what have we learned in the last decade? CNS neuroscience & therapeutics 17: 4–31 (2011).

13. Bender, Andreas; Krishnan, Kim J.; Morris, Christopher M.; Taylor, Geoffrey A.; Reeve, Amy K.; Perry, Robert H.; Jaros, Evelyn; Hersheson, Joshua S.; Betts, Joanne; Klopstock, Thomas; Taylor, Robert W.; Turnbull, Douglass M.: High levels of mitochondrial DNA deletions in substantia nigra neurons in aging and Parkinson disease. Nature Genetics 38: 515–517 (2006).

14. Berridge, Michael J.; Bootman, Martin D.; Roderick, H. Llewelyn: Calcium signalling: dynamics, homeostasis and remodelling. Nature reviews. Molecular cell biology 4: 517–529 (2003).

15. Bi, Fangfang; Huang, Cao; Tong, Jianbin; Qiu, Guang; Huang, Bo; Wu, Qinxue; Li, Fang; Xu, Zuoshang; Bowser, Robert; Xia, Xu-Gang; Zhou, Hongxia: Reactive astrocytes secrete lcn2 to promote neuron death. Proceedings of the National Academy of Sciences of the United States of America 110: 4069–4074 (2013).

16. Boillée, Séverine; Yamanaka, Koji; Lobsiger, Christian S.; Copeland, Neal G.; Jenkins, Nancy A.; Kassiotis, George; Kollias, George; Cleveland, Don W.: Onset and progression in inherited ALS determined by motor neurons and microglia. Science (New York, N.Y.) 312: 1389–1392 (2006).

17. Boscia, Francesca; Gala, Rosaria; Pignataro, Giuseppe; Bartolomeis, Andrea de; Cicale, Maria; Ambesi-Impiombato, Alberto; Di Renzo, Gianfranco; Annunziato, Lucio: Permanent focal brain ischemia induces isoform-dependent changes in the pattern of Na+/Ca2+ exchanger gene expression in the ischemic core, periinfarct area, and intact brain regions. Journal of cerebral blood flow and metabolism : official journal of the International Society of Cerebral Blood Flow and Metabolism 26: 502–517 (2006).

18. Bosco, Daryl A.; Morfini, Gerardo; Karabacak, N. Murat; Song, Yuyu; Gros-Louis, Francois; Pasinelli, Piera; Goolsby, Holly; Fontaine, Benjamin A.; Lemay, Nathan; McKenna-Yasek, Diane; Frosch, Matthew P.; Agar, Jeffrey N.; Julien, Jean-Pierre; Brady, Scott T.; Brown, Robert H.: Wild-type and mutant SOD1 share an aberrant conformation and a common pathogenic pathway in ALS. Nature Neuroscience 13: 1396–1403 (2010).

19. Boyman, Liron; Hagen, Brian M.; Giladi, Moshe; Hiller, Reuben; Lederer, W. Jonathan; Khananshvili, Daniel: Proton-sensing Ca2+ binding domains regulate the cardiac Na+/Ca2+ exchanger. The Journal of biological chemistry 286: 28811–28820 (2011).

20. Boyman, Liron; Williams, George S B; Khananshvili, Daniel; Sekler, Israel; Lederer, W. J.: NCLX: the mitochondrial sodium calcium exchanger. Journal of molecular and cellular cardiology 59: 205–213 (2013).

21. Braak, Heiko; Brettschneider, Johannes; Ludolph, Albert C.; Lee, Virginia M.; Trojanowski, John Q.; Del Tredici, Kelly: Amyotrophic lateral sclerosis--a model of corticofugal axonal spread. Nature reviews. Neurology 9: 708–714 (2013).

22. Brini, M.; Carafoli, E.: The Plasma Membrane Ca2+ ATPase and the Plasma Membrane Sodium Calcium Exchanger Cooperate in the Regulation of Cell Calcium. Cold Spring Harbor Perspectives in Biology 3: a004168 (2011).

23. Brini, Marisa; Calì, Tito; Ottolini, Denis; Carafoli, Ernesto: The plasma membrane calcium pump in health and disease. The FEBS journal 280: 5385–5397 (2013).

24. Brini, Marisa; Calì, Tito; Ottolini, Denis; Carafoli, Ernesto: Neuronal calcium signaling: function and dysfunction. Cellular and molecular life sciences : CMLS 71: 2787–2814 (2014).

25. Brini, Marisa; Carafoli, Ernesto: Calcium pumps in health and disease. Physiological reviews 89: 1341–1378 (2009).

26. Brockington, Alice; Heath, Paul R.; Holden, Hazel; Kasher, Paul; Bender, Florian L P; Claes, Filip; Lambrechts, Diether; Sendtner, Michael; Carmeliet, Peter; Shaw, Pamela J.: Downregulation of genes with a function in axon outgrowth and synapse formation in motor neurones of the VEGFdelta/delta mouse model of amyotrophic lateral sclerosis. BMC Genomics 11: 203 (2010).

27. Brockington, Alice; Ning, Ke; Heath, Paul R.; Wood, Elizabeth; Kirby, Janine; Fusi, Nicolò; Lawrence, Neil; Wharton, Stephen B.; Ince, Paul G.; Shaw, Pamela J.: Unravelling the enigma of selective vulnerability in neurodegeneration: motor neurons resistant to degeneration in ALS show distinct gene expression characteristics and decreased susceptibility to excitotoxicity. Acta Neuropathologica 125: 95–109 (2013).

28. Brooks, B. R.; Miller, R. G.; Swash, M.; Munsat, T. L.: El Escorial revisited: revised criteria for the diagnosis of amyotrophic lateral sclerosis. Amyotrophic lateral sclerosis and other motor neuron disorders : official publication of the World Federation of Neurology, Research Group on Motor Neuron Diseases 1: 293–299 (2000).

29. Bruijn, L. I.; Houseweart, M. K.; Kato, S.; Anderson, K. L.; Anderson, S. D.; Ohama, E.; Reaume, A. G.; Scott, R. W.; Cleveland, D. W.: Aggregation and motor neuron toxicity of an ALS-linked SOD1 mutant independent from wild-type SOD1. Science (New York, N.Y.) 281: 1851–1854 (1998).

30. Byrne, Susan; Walsh, Cathal; Lynch, Catherine; Bede, Peter; Elamin, Marwa; Kenna, Kevin; McLaughlin, Russell; Hardiman, Orla: Rate of familial amyotrophic lateral sclerosis: a systematic review and meta-analysis. Journal of neurology, neurosurgery, and psychiatry 82: 623–627 (2011).

31. Carrì, M. T.; Ferri, A.; Battistoni, A.; Famhy, L.; Gabbianelli, R.; Poccia, F.; Rotilio, G.: Expression of a Cu,Zn superoxide dismutase typical of familial amyotrophic lateral sclerosis induces mitochondrial alteration and increase of cytosolic Ca2+ concentration in transfected neuroblastoma SH-SY5Y cells. FEBS letters 414: 365–368 (1997).

32. Charcot, J.; Joffroy, A.: Deux cas d’atrophie musculaire progressive avec lésions de la substance grise et des faisceaux antéro-latéraux de la moelle épiniére. Arch Physiol Neurol Path 2: 744–750 (1869).

33. Chaudhuri, Dipayan; Sancak, Yasemin; Mootha, Vamsi K.; Clapham, David E.: MCU encodes the pore conducting mitochondrial calcium currents. eLife 2: e00704 (2013).

34. Chen, Yanchun; Guan, Yingjun; Liu, Huancai; Wu, Xin; Yu, Li; Wang, Shanshan; Zhao, Chunyan; Du, Hongmei; Wang, Xin: Activation of the Wnt/β-catenin signaling pathway is associated with glial proliferation in the adult spinal cord of ALS transgenic mice. Biochemical and biophysical research communications 420: 397–403 (2012).

35. Chew, Jeannie; Gendron, Tania F.; Prudencio, Mercedes; Sasaguri, Hiroki; Zhang, Yong-Jie; Castanedes-Casey, Monica; Lee, Chris W.; Jansen-West, Karen; Kurti, Aishe; Murray, Melissa E.; Bieniek, Kevin F.; Bauer, Peter O.; Whitelaw, Ena C.; Rousseau, Linda; Stankowski, Jeannette N.; Stetler, Caroline; Daughrity, Lillian M.; Perkerson, Emilie A.; Desaro, Pamela; Johnston, Amelia; Overstreet, Karen; Edbauer, Dieter; Rademakers, Rosa; Boylan, Kevin B.; Dickson, Dennis W.; Fryer, John D.; Petrucelli, Leonard: Neurodegeneration. C9ORF72 repeat expansions in mice cause TDP-43 pathology, neuronal loss, and behavioral deficits. Science (New York, N.Y.) 348: 1151–1154 (2015).

36. Chinopoulos, Christos; Adam-Vizi, Vera: Mitochondrial Ca2+ sequestration and precipitation revisited. The FEBS journal 277: 3637–3651 (2010).

37. Chiò, A.; Logroscino, G.; Traynor, B.J.; Collins, J.; Simeone, J.C.; Goldstein, L.A.; White, L.A.: Global Epidemiology of Amyotrophic Lateral Sclerosis: A Systematic Review of the Published Literature. Neuroepidemiology 41: 118–130 (2013).

38. Coussee, Evelyne; Smet, Patrick de; Bogaert, Elke; Elens, Iris; van Damme, Philip; Willems, Peter; Koopman, Werner; van Den Bosch, Ludo; Callewaert, Geert: G37R SOD1 mutant alters mitochondrial complex I activity, Ca2+ uptake and ATP production. Cell Calcium 49: 217–225 (2011).

39. Cova, J. L.; Aldskogius, H.: A morphological study of glial cells in the hypoglossal nucleus of the cat during nerve regeneration. The Journal of comparative neurology 233: 421–428 (1985).

40. Cozzolino, Mauro; Carrì, Maria Teresa: Mitochondrial dysfunction in ALS. Progress in neurobiology 97: 54–66 (2012).

41. Cozzolino, Mauro; Ferri, Alberto; Valle, Cristiana; Carrì, Maria Teresa: Mitochondria and ALS: Implications from novel genes and pathways. Molecular and Cellular Neuroscience 55: 44–49 (2013).

42. Dal Canto, M.; Gurney, M.: Development of central nervous system pathology in a murine transgenic model of human amyotrophic lateral sclerosis. The American journal of pathology 145: 1271–1279 (1994).

43. DeJesus-Hernandez, Mariely; Mackenzie, Ian R.; Boeve, Bradley F.; Boxer, Adam L.; Baker, Matt; Rutherford, Nicola J.; Nicholson, Alexandra M.; Finch, NiCole A.; Flynn, Heather; Adamson, Jennifer; Kouri, Naomi; Wojtas, Aleksandra; Sengdy, Pheth; Hsiung, Ging-Yuek R.; Karydas, Anna; Seeley, William W.; Josephs, Keith A.; Coppola, Giovanni; Geschwind, Daniel H.; Wszolek, Zbigniew K.; Feldman, Howard; Knopman, David S.; Petersen, Ronald C.; Miller, Bruce L.; Dickson, Dennis W.; Boylan, Kevin B.; Graff-Radford, Neill R.; Rademakers, Rosa: Expanded GGGGCC hexanucleotide repeat in noncoding region of C9ORF72 causes chromosome 9p-linked FTD and ALS. Neuron 72: 245–256 (2011).

44. Dimmer, Kai Stefan; Navoni, Francesca; Casarin, Alberto; Trevisson, Eva; Endele, Sabine; Winterpacht, Andreas; Salviati, Leonardo; Scorrano, Luca: LETM1, deleted in Wolf-Hirschhorn syndrome is required for normal mitochondrial morphology and cellular viability. Human molecular genetics 17: 201–214 (2008).

45. DiPolo, Reinaldo; Beaugé, Luis: Sodium/calcium exchanger: influence of metabolic regulation on ion carrier interactions. Physiological reviews 86: 155–203 (2006).

46. Donadelli, Massimo; Dando, Ilaria; Fiorini, Claudia; Palmieri, Marta: UCP2, a mitochondrial protein regulated at multiple levels. Cellular and Molecular Life Sciences 71: 1171–1190 (2014).

47. Drago, Ilaria; Pizzo, Paola; Pozzan, Tullio: After half a century mitochondrial calcium in- and efflux machineries reveal themselves. The EMBO Journal 30: 4119–4125 (2011).

48. Dunn, Jeremy; Elias, Chadwick L.; Le, Hoa Dinh; Omelchenko, Alexander; Hryshko, Larry V.; Lytton, Jonathan: The molecular determinants of ionic regulatory differences between brain and kidney Na+/Ca2+ exchanger (NCX1) isoforms. The Journal of biological chemistry 277: 33957–33962 (2002).

49. 'Episcopo, Francesca L.; Tirolo, Cataldo; Testa, Nuccio; Caniglia, Salvo; Morale, Maria Concetta; Marchetti, Bianca: Reactive astrocytes are key players in nigrostriatal dopaminergic neurorepair in the MPTP mouse model of Parkinson's disease: focus on endogenous neurorestoration. Current aging science 6: 45–55 (2013).

50. Ferraiuolo, Laura; Heath, Paul R.; Holden, Hazel; Kasher, Paul; Kirby, Janine; Shaw, Pamela J.: Microarray analysis of the cellular pathways involved in the adaptation to and progression of motor neuron injury in the SOD1 G93A mouse model of familial ALS. The Journal of neuroscience : the official journal of the Society for Neuroscience 27: 9201–9219 (2007).

51. Ferraiuolo, Laura; Kirby, Janine; Grierson, Andrew J.; Sendtner, Michael; Shaw, Pamela J.: Molecular pathways of motor neuron injury in amyotrophic lateral sclerosis. Nature reviews. Neurology 7: 616–630 (2011).

52. Ferrucci, Michela; Spalloni, Alida; Bartalucci, Alessia; Cantafora, Emanuela; Fulceri, Federica; Nutini, Michele; Longone, Patrizia; Paparelli, Antonio; Fornai, Francesco: A systematic study of brainstem motor nuclei in a mouse model of ALS, the effects of lithium. Neurobiology of Disease 37: 370–383 (2010).

53. Fischer, Lindsey R.; Culver, Deborah G.; Tennant, Philip; Davis, Albert A.; Wang, Minsheng; Castellano-Sanchez, Amilcar; Khan, Jaffar; Polak, Meraida A.; Glass, Jonathan D.: Amyotrophic lateral sclerosis is a distal axonopathy: evidence in mice and man. Experimental neurology 185: 232–240 (2004).

54. Forsberg, Karin; Andersen, Peter M.; Marklund, Stefan L.; Brännström, Thomas: Glial nuclear aggregates of superoxide dismutase-1 are regularly present in patients with amyotrophic lateral sclerosis. Acta neuropathologica 121: 623–634 (2011).

55. Foskett, J. Kevin; Madesh, Muniswamy: Regulation of the mitochondrial Ca(2+) uniporter by MICU1 and MICU2. Biochemical and Biophysical Research Communications 449: 377–383 (2014).

56. Frank-Cannon, Tamy C.; Alto, Laura T.; McAlpine, Fiona E.; Tansey, Malú G.: Does neuroinflammation fan the flame in neurodegenerative diseases? Molecular neurodegeneration 4: 47 (2009).

57. Fratta, Pietro; Mizielinska, Sarah; Nicoll, Andrew J.; Zloh, Mire; Fisher, Elizabeth M C; Parkinson, Gary; Isaacs, Adrian M.: C9orf72 hexanucleotide repeat associated with amyotrophic lateral sclerosis and frontotemporal dementia forms RNA G-quadruplexes. Scientific reports 2: 1016 (2012).

58. Fray, A. E.; Ince, P. G.; Banner, S. J.; Milton, I. D.; Usher, P. A.; Cookson, M. R.; Shaw, P. J.: The expression of the glial glutamate transporter protein EAAT2 in motor neuron disease: an immunohistochemical study. The European journal of neuroscience 10: 2481–2489 (1998).

59. Freischmidt, Axel; Müller, Kathrin; Zondler, Lisa; Weydt, Patrick; Volk, Alexander E.; Božič, Anže Lošdorfer; Walter, Michael; Bonin, Michael; Mayer, Benjamin; von Arnim, Christine A F; Otto, Markus; Dieterich, Christoph; Holzmann, Karlheinz; Andersen, Peter M.; Ludolph, Albert C.; Danzer, Karin M.; Weishaupt, Jochen H.: Serum microRNAs in patients with genetic amyotrophic lateral sclerosis and pre-manifest mutation carriers. Brain : a journal of neurology 137: 2938–2950 (2014).

60. Fuchs, Andrea: Neurophysiologische Charakterisierung von adulten vulnerablen und resistenten Motoneuronen in einem Mausmodell der Amyotrophen Lateralsklerose. PhD Thesis. Philipps University Marburg, Marburg. Institute of Anatomiy and Cell Biology (2013).

61. Fuchs, Andrea; Kutterer, Sylvie; Mühling, Tobias; Duda, Johanna; Schütz, Burkhard; Liss, Birgit; Keller, Bernhard U.; Roeper, Jochen: Selective mitochondrial Ca 2+ uptake deficit in disease endstage vulnerable motoneurons of the SOD1 G93A mouse model of amyotrophic lateral sclerosis. The Journal of Physiology 591: 2723–2745 (2013).

62. Fuchs, Andrea; Ringer, Cornelia; Bilkei-Gorzo, Andras; Weihe, Eberhard; Roeper, Jochen; Schütz, Burkhard: Downregulation of the potassium chloride cotransporter KCC2 in vulnerable motoneurons in the SOD1-G93A mouse model of amyotrophic lateral sclerosis. Journal of neuropathology and experimental neurology 69: 1057–1070 (2010).

63. Gao, Tao; McKenna, Brian; Li, Changhong; Reichert, Maximilian; Nguyen, James; Singh, Tarjinder; Yang, Chenghua; Pannikar, Archana; Doliba, Nicolai; Zhang, Tingting; Stoffers, Doris A.; Edlund, Helena; Matschinsky, Franz; Stein, Roland; Stanger, Ben Z.: Pdx1 maintains β cell identity and function by repressing an α cell program. Cell metabolism 19: 259–271 (2014).

64. Gincel, D.; Zaid, H.; Shoshan-Barmatz, V.: Calcium binding and translocation by the voltage-dependent anion channel: a possible regulatory mechanism in mitochondrial function. The Biochemical journal 358: 147–155 (2001).

65. Giorgi, Carlotta; Baldassari, Federica; Bononi, Angela; Bonora, Massimo; Marchi, Elena de; Marchi, Saverio; Missiroli, Sonia; Patergnani, Simone; Rimessi, Alessandro; Suski, Jan M.; Wieckowski, Mariusz R.; Pinton, Paolo: Mitochondrial Ca(2+) and apoptosis. Cell Calcium 52: 36–43 (2012).

66. Gordon, Paul: Amyotrophic Lateral Sclerosis: An update for 2013 Clinical Features, Pathophysiology, Management and Therapeutic Trials. Aging and Disease 04: 295–310 (2013).

67. Gordon, Paul H.; Salachas, François; Lacomblez, Lucette; Le Forestier, Nadine; Pradat, Pierre-François; Bruneteau, Gaelle; Elbaz, Alexis; Meininger, Vincent: Predicting Survival of Patients with Amyotrophic Lateral Sclerosis at Presentation: A 15-Year Experience. Neurodegenerative Diseases 12: 81–90 (2013).

68. Grosskreutz, Julian; Haastert, Kirsten; Dewil, Maarten; van Damme, Philip; Callewaert, Geert; Robberecht, Wim; Dengler, Reinhard; van Den Bosch, Ludo: Role

of mitochondria in kainate-induced fast Ca2+ transients in cultured spinal motor neurons. Cell calcium 42: 59–69 (2007).

69. Gründemann, Jan; Schlaudraff, Falk; Haeckel, Olga; Liss, Birgit: Elevated alpha-synuclein mRNA levels in individual UV-laser-microdissected dopaminergic substantia nigra neurons in idiopathic Parkinson's disease. Nucleic acids research 36: e38 (2008).

70. Gründemann, Jan; Schlaudraff, Falk; Liss, Birgit: UV-laser microdissection and mRNA expression analysis of individual neurons from postmortem Parkinson's disease brains. Methods in molecular biology (Clifton, N.J.) 755: 363–374 (2011).

71. Gurney, M. E.; Pu, H.; Chiu, A. Y.; Dal Canto, M C; Polchow, C. Y.; Alexander, D. D.; Caliendo, J.; Hentati, A.; Kwon, Y. W.; Deng, H. X.: Motor neuron degeneration in mice that express a human Cu,Zn superoxide dismutase mutation. Science (New York, N.Y.) 264: 1772–1775 (1994).

72. Guzman, Jaime N.; Sanchez-Padilla, Javier; Wokosin, David; Kondapalli, Jyothisri; Ilijic, Ema; Schumacker, Paul T.; Surmeier, D. James: Oxidant stress evoked by pacemaking in dopaminergic neurons is attenuated by DJ-1. Nature 468: 696–700 (2010).

73. Haenggeli, Christine; Kato, Ann C.: Differential vulnerability of cranial motoneurons in mouse models with motor neuron degeneration. Neuroscience letters 335: 39–43 (2002).

74. Harraz, Maged M.; Marden, Jennifer J.; Zhou, Weihong; Zhang, Yulong; Williams, Aislinn; Sharov, Victor S.; Nelson, Kathryn; Luo, Meihui; Paulson, Henry; Schöneich, Christian; Engelhardt, John F.: SOD1 mutations disrupt redox-sensitive Rac regulation of NADPH oxidase in a familial ALS model. The Journal of clinical investigation 118: 659–670 (2008).

75. He, Langping; Chinnery, Patrick F.; Durham, Steve E.; Blakely, Emma L.; Wardell, Theresa M.; Borthwick, Gillian M.; Taylor, Robert W.; Turnbull, Douglass M.: Detection and quantification of mitochondrial DNA deletions in individual cells by real-time PCR. Nucleic acids research 30: e68 (2002).

76. Hedlund, Eva; Karlsson, Martin; Osborn, Teresia; Ludwig, Wesley; Isacson, Ole: Global gene expression profiling of somatic motor neuron populations with different vulnerability identify molecules and pathways of degeneration and protection. Brain : a journal of neurology 133: 2313–2330 (2010).

77. Hilge, Mark; Aelen, Jan; Vuister, Geerten W.: Ca2+ regulation in the Na+/Ca2+ exchanger involves two markedly different Ca2+ sensors. Molecular cell 22: 15–25 (2006).

78. Hol, E. M.; Roelofs, R. F.; Moraal, E.; Sonnemans, M A F; Sluijs, J. A.; Proper, E. A.; de Graan, P N E; Fischer, D. F.; van Leeuwen, F W: Neuronal expression of GFAP in patients with Alzheimer pathology and identification of novel GFAP splice forms. Molecular psychiatry 8: 786–796 (2003).

79. Howland, David S.; Liu, Jian; She, Yijin; Goad, Beth; Maragakis, Nicholas J.; Kim, Benjamin; Erickson, Jamie; Kulik, John; DeVito, Lisa; Psaltis, George; DeGennaro, Louis J.; Cleveland, Don W.; Rothstein, Jeffrey D.: Focal loss of the glutamate transporter EAAT2 in a transgenic rat model of SOD1 mutant-mediated amyotrophic lateral sclerosis (ALS). Proceedings of the National Academy of Sciences of the United States of America 99: 1604–1609 (2002).

80. Hübers, Annemarie; Just, Walter; Rosenbohm, Angela; Müller, Kathrin; Marroquin, Nicolai; Goebel, Ingrid; Högel, Josef; Thiele, Holger; Altmüller, Janine; Nürnberg, Peter; Weishaupt, Jochen H.; Kubisch, Christian; Ludolph, Albert C.; Volk, Alexander E.: De novo FUS mutations are the most frequent genetic cause in early-onset German ALS patients. Neurobiology of Aging 36: 3117.e1-6 (2015).

81. Igoudjil, A.; Magrane, J.; Fischer, L. R.; Kim, H. J.; Hervias, I.; Dumont, M.; Cortez, C.; Glass, J. D.; Starkov, A. A.; Manfredi, G.: In Vivo Pathogenic Role of Mutant SOD1 Localized in the Mitochondrial Intermembrane Space. Journal of Neuroscience 31: 15826–15837 (2011).

82. Ionov, Ilya D.: Survey of ALS-associated factors potentially promoting Ca2+ overload of motor neurons. Amyotrophic lateral sclerosis : official publication of the World Federation of Neurology Research Group on Motor Neuron Diseases 8: 260–265 (2007).

83. Jaiswal, Manoj Kumar; Keller, Bernhard U.: Cu/Zn superoxide dismutase typical for familial amyotrophic lateral sclerosis increases the vulnerability of mitochondria and perturbs Ca2+ homeostasis in SOD1G93A mice. Molecular pharmacology 75: 478–489 (2009).

84. Jiang, D.; Zhao, L.; Clapham, D. E.: Genome-Wide RNAi Screen Identifies Letm1 as a Mitochondrial Ca2+/H+ Antiporter. Science 326: 144–147 (2009).

85. Jiang, Dawei; Zhao, Linlin; Clish, Clary B.; Clapham, David E.: Letm1, the mitochondrial Ca2+/H+ antiporter, is essential for normal glucose metabolism and alters brain function in Wolf-Hirschhorn syndrome. Proceedings of the National Academy of Sciences of the United States of America 110: E2249-54 (2013).

86. Jiang, Yue-Mei; Yamamoto, Masahiko; Kobayashi, Yasushi; Yoshihara, Tsuyoshi; Liang, Yideng; Terao, Shinichi; Takeuchi, Hideyuki; Ishigaki, Shinsuke; Katsuno, Masahisa; Adachi, Hiroaki; Niwa, Jun-ichi; Tanaka, Fumiaki; Doyu, Manabu; Yoshida, Mari; Hashizume, Yoshio; Sobue, Gen: Gene expression profile of spinal motor neurons in sporadic amyotrophic lateral sclerosis. Annals of neurology 57: 236–251 (2005).

87. Kamer, Kimberli J.; Mootha, Vamsi K.: MICU1 and MICU2 play nonredundant roles in the regulation of the mitochondrial calcium uniporter. EMBO reports 15: 299–307 (2014).

88. Kato, Shinsuke; Kato, Masako; Abe, Yasuko; Matsumura, Tomohiro; Nishino, Takeshi; Aoki, Masashi; Itoyama, Yasuto; Asayama, Kohtaro; Awaya, Akira; Hirano, Asao; Ohama, Eisaku: Redox system expression in the motor neurons in amyotrophic lateral sclerosis (ALS): immunohistochemical studies on sporadic ALS, superoxide dismutase 1 (SOD1)-mutated familial ALS, and SOD1-mutated ALS animal models. Acta Neuropathologica 110: 101–112 (2005).

89. Kawamata, Hibiki; Manfredi, Giovanni: Mitochondrial dysfunction and intracellular calcium dysregulation in ALS. Mechanisms of Ageing and Development 131: 517–526 (2010).

90. Keeney, Paula M.; Bennett, James P.: ALS spinal neurons show varied and reduced mtDNA gene copy numbers and increased mtDNA gene deletions. Molecular neurodegeneration 5: 21 (2010).

91. Khananshvili, Daniel: The SLC8 gene family of sodium-calcium exchangers (NCX) - structure, function, and regulation in health and disease. Molecular aspects of medicine 34: 220–235 (2013).

92. Kiernan, Matthew C.; Vucic, Steve; Cheah, Benjamin C.; Turner, Martin R.; Eisen, Andrew; Hardiman, Orla; Burrell, James R.; Zoing, Margaret C.: Amyotrophic lateral sclerosis. The Lancet 377: 942–955 (2011).

93. Kim, Bongju; Matsuoka, Satoshi: Cytoplasmic Na+-dependent modulation of mitochondrial Ca2+ via electrogenic mitochondrial Na+-Ca2+ exchange. The Journal of physiology 586: 1683–1697 (2008).

94. Kurnellas, Michael P.; Nicot, Arnaud; Shull, Gary E.; Elkabes, Stella: Plasma membrane calcium ATPase deficiency causes neuronal pathology in the spinal cord: a potential mechanism for neurodegeneration in multiple sclerosis and spinal cord injury. FASEB journal : official publication of the Federation of American Societies for Experimental Biology 19: 298–300 (2005).

95. Kwak, Shin; Kawahara, Yukio: Deficient RNA editing of GluR2 and neuronal death in amyotropic lateral sclerosis. Journal of molecular medicine (Berlin, Germany) 83: 110–120 (2005).

96. Lagier-Tourenne, Clotilde; Polymenidou, Magdalini; Cleveland, Don W.: TDP-43 and FUS/TLS: emerging roles in RNA processing and neurodegeneration. Human molecular genetics 19: R46-64 (2010).

97. Lamanauskas, Nerijus; Nistri, Andrea: Riluzole blocks persistent Na+ and Ca2+ currents and modulates release of glutamate via presynaptic NMDA receptors on neonatal rat hypoglossal motoneurons in vitro. The European journal of neuroscience 27: 2501–2514 (2008).

98. Leblond, Claire S.; Kaneb, Hannah M.; Dion, Patrick A.; Rouleau, Guy A.: Dissection of genetic factors associated with amyotrophic lateral sclerosis. Experimental Neurology (2014).

99. Leitner, M.; Menzies, S.; Lutz, C.: Working with ALS Mice. Available online at http://jaxmice.jax.org/literature /factsheet/working_with_ALS_mice.pdf, checked on 10/2011.

100. Levine, Timothy P.; Daniels, Rachel D.; Gatta, Alberto T.; Wong, Louise H.; Hayes, Matthew J.: The product of C9orf72, a gene strongly implicated in neurodegeneration, is structurally related to DENN Rab-GEFs. Bioinformatics (Oxford, England) 29: 499–503 (2013).

101. Lewinski, Friederike von; Keller, Bernhard U.: Ca2+, mitochondria and selective motoneuron vulnerability: implications for ALS. Trends in Neurosciences 28: 494–500 (2005).

102. Li, Quan; Vande Velde, Christine; Israelson, Adrian; Xie, Jing; Bailey, Aaron O.; Dong, Meng-Qui; Chun, Seung-Joo; Roy, Tamal; Winer, Leah; Yates, John R.; Capaldi, Roderick A.; Cleveland, Don W.; Miller, Timothy M.: ALS-linked mutant superoxide dismutase 1 (SOD1) alters mitochondrial protein composition and decreases protein import. Proceedings of the National Academy of Sciences of the United States of America 107: 21146–21151 (2010).

103. Lino, Maria Maddalena; Schneider, Corinna; Caroni, Pico: Accumulation of SOD1 mutants in postnatal motoneurons does not cause motoneuron pathology or

motoneuron disease. The Journal of neuroscience : the official journal of the Society for Neuroscience 22: 4825–4832 (2002).

104. Liss, Birgit: Improved quantitative real-time RT-PCR for expression profiling of individual cells. Nucleic acids research 30: e89 (2002).

105. Liss, Birgit; Haeckel, Olga; Wildmann, Johannes; Miki, Takashi; Seino, Susumu; Roeper, Jochen: K-ATP channels promote the differential degeneration of dopaminergic midbrain neurons. Nature neuroscience 8: 1742–1751 (2005).

106. Lloret, A.; Fuchsberger, T.; Giraldo, E.; Viña, J.: Molecular mechanisms linking amyloid β toxicity and Tau hyperphosphorylation in Alzheimer′s disease. Free radical biology & medicine 83: 186–191 (2015).

107. Lobsiger, Christian S.; Boillée, Séverine; Cleveland, Don W.: Toxicity from different SOD1 mutants dysregulates the complement system and the neuronal regenerative response in ALS motor neurons. Proceedings of the National Academy of Sciences of the United States of America 104: 7319–7326 (2007).

108. Logroscino, G.; Traynor, B. J.; Hardiman, O.; Chio, A.; Mitchell, D.; Swingler, R. J.; Millul, A.; Benn, E.; Beghi, E.: Incidence of amyotrophic lateral sclerosis in Europe. Journal of Neurology, Neurosurgery & Psychiatry 81: 385–390 (2010).

109. Lopreiato, Raffaele; Giacomello, Marta; Carafoli, Ernesto: The plasma membrane calcium pump: new ways to look at an old enzyme. The Journal of biological chemistry 289: 10261–10268 (2014).

110. Lytton, J.; Westlin, M.; Hanley, M. R.: Thapsigargin inhibits the sarcoplasmic or endoplasmic reticulum Ca-ATPase family of calcium pumps. The Journal of biological chemistry 266: 17067–17071 (1991).

111. Mackenzie, Ian; Bigio, Eileen H.; Ince, Paul G.; Geser, Felix; Neumann, Manuela; Cairns, Nigel J.; Kwong, Linda K.; Forman, Mark S.; Ravits, John; Stewart, Heather; Eisen, Andrew; McClusky, Leo; Kretzschmar, Hans A.; Monoranu, Camelia M.; Highley, J. Robin; Kirby, Janine; Siddique, Teepu; Shaw, Pamela J.; Lee, Virginia M-Y.; Trojanowski, John Q.: Pathological TDP-43 distinguishes sporadic amyotrophic lateral sclerosis from amyotrophic lateral sclerosis withSOD1 mutations. Annals of Neurology 61: 427–434 (2007).

112. Mackenzie, Ian; Feldman, Howard H.: Ubiquitin immunohistochemistry suggests classic motor neuron disease, motor neuron disease with dementia, and frontotemporal dementia of the motor neuron disease type represent a clinicopathologic spectrum. Journal of neuropathology and experimental neurology 64: 730–739 (2005).

113. Mackenzie, Ian; Frick, Petra; Neumann, Manuela: The neuropathology associated with repeat expansions in the C9ORF72 gene. Acta Neuropathologica 127: 347–357 (2014).

114. Magrané, Jordi; Manfredi, Giovanni: Mitochondrial function, morphology, and axonal transport in amyotrophic lateral sclerosis. Antioxidants & redox signaling 11: 1615–1626 (2009).

115. Mallilankaraman, Karthik; Cárdenas, César; Doonan, Patrick J.; Chandramoorthy, Harish C.; Irrinki, Krishna M.; Golenár, Tünde; Csordás, György; Madireddi, Priyanka; Yang, Jun; Müller, Marioly; Miller, Russell; Kolesar, Jill E.; Molgó, Jordi; Kaufman, Brett; Hajnóczky, György; Foskett, J. Kevin; Madesh,

Muniswamy: MCUR1 is an essential component of mitochondrial Ca2+ uptake that regulates cellular metabolism. Nature Cell Biology 14: 1336–1343 (2012a).

116. Mallilankaraman, Karthik; Doonan, Patrick; Cárdenas, César; Chandramoorthy, Harish C.; Müller, Marioly; Miller, Russell; Hoffman, Nicholas E.; Gandhirajan, Rajesh Kumar; Molgó, Jordi; Birnbaum, Morris J.; Rothberg, Brad S.; Mak, Don-On Daniel; Foskett, J. Kevin; Madesh, Muniswamy: MICU1 Is an Essential Gatekeeper for MCU-Mediated Mitochondrial Ca2+ Uptake that Regulates Cell Survival. Cell 151: 630–644 (2012b).

117. Mancuso, Renzo; Navarro, Xavier: Amyotrophic lateral sclerosis: Current perspectives from basic research to the clinic. Progress in neurobiology (2015).

118. Mannen, T.; Iwata, M.; Toyokura, Y.; Nagashima, K.: Preservation of a certain motoneurone group of the sacral cord in amyotrophic lateral sclerosis: its clinical significance. Journal of neurology, neurosurgery, and psychiatry 40: 464–469 (1977).

119. Marchi, Saverio; Pinton, Paolo: The mitochondrial calcium uniporter complex: molecular components, structure and physiopathological implications. The Journal of physiology 592: 829–839 (2014).

120. Martin, Lee J.: The mitochondrial permeability transition pore: a molecular target for amyotrophic lateral sclerosis therapy. Biochimica et biophysica acta 1802: 186–197 (2010).

121. Martin, Lee J.: Mitochondrial pathobiology in ALS. Journal of bioenergetics and biomembranes 43: 569–579 (2011).

122. Martins, Dorival; English, Ann M.: SOD1 oxidation and formation of soluble aggregates in yeast: Relevance to sporadic ALS development. Redox Biology 2: 632–639 (2014).

123. Mawrin, Christian; Kirches, Elmar; Dietzmann, Knut: Single-cell analysis of mtDNA in amyotrophic lateral sclerosis: towards the characterization of individual neurons in neurodegenerative disorders. Pathology, research and practice 199: 415–418 (2003).

124. Mawrin, Christian; Kirches, Elmar; Krause, Guido; Wiedemann, Falk R.; Vorwerk, Christian K.; Bogerts, Bernhard; Schildhaus, Hans-Ulrich; Dietzmann, Knut; Schneider-Stock, Regine: Single-cell analysis of mtDNA deletion levels in sporadic amyotrophic lateral sclerosis. Neuroreport 15: 939–943 (2004).

125. Maximino, Jessica R.; de Oliveira, Gabriela P; Alves, Chrystian J.; Chadi, Gerson: Deregulated expression of cytoskeleton related genes in the spinal cord and sciatic nerve of presymptomatic SOD1(G93A) Amyotrophic Lateral Sclerosis mouse model. Frontiers in cellular neuroscience 8: 148 (2014).

126. McCormack, J. G.; Denton, R. M.: The role of mitochondrial Ca2+ transport and matrix Ca2+ in signal transduction in mammalian tissues. Biochimica et biophysica acta 1018: 287–291 (1990).

127. McGoldrick, Philip; Joyce, Peter I.; Fisher, Elizabeth M C; Greensmith, Linda: Rodent models of amyotrophic lateral sclerosis. Biochimica et biophysica acta 1832: 1421–1436 (2013).

128. Miller, R. G.; Jackson, C. E.; Kasarskis, E. J.; England, J. D.; Forshew, D.; Johnston, W.; Kalra, S.; Katz, J. S.; Mitsumoto, H.; Rosenfeld, J.; Shoesmith, C.; Strong, M. J.; Woolley, S. C.: Practice parameter update: the care of the patient with

amyotrophic lateral sclerosis: multidisciplinary care, symptom management, and cognitive/behavioral impairment (an evidence-based review): report of the Quality Standards Subcommittee of the American Academy of Neurology. Neurology 73: 1227–1233 (2009).

129. Miller, Timothy M.; Kim, Soo H.; Yamanaka, Koji; Hester, Mark; Umapathi, Priya; Arnson, Hannah; Rizo, Liza; Mendell, Jerry R.; Gage, Fred H.; Cleveland, Don W.; Kaspar, Brian K.: Gene transfer demonstrates that muscle is not a primary target for non-cell-autonomous toxicity in familial amyotrophic lateral sclerosis. Proceedings of the National Academy of Sciences of the United States of America 103: 19546–19551 (2006).

130. Moisse, Katie; Volkening, Kathryn; Leystra-Lantz, Cheryl; Welch, Ian; Hill, Tracy; Strong, Michael J.: Divergent patterns of cytosolic TDP-43 and neuronal progranulin expression following axotomy: implications for TDP-43 in the physiological response to neuronal injury. Brain research 1249: 202–211 (2009).

131. Molinaro, Pasquale; Cuomo, Ornella; Pignataro, Giuseppe; Boscia, Francesca; Sirabella, Rossana; Pannaccione, Anna; Secondo, Agnese; Scorziello, Antonella; Adornetto, Annagrazia; Gala, Rosaria; Viggiano, Davide; Sokolow, Sophie; Herchuelz, Andre; Schurmans, Stèphane; Di Renzo, Gianfranco; Annunziato, Lucio: Targeted disruption of Na+/Ca2+ exchanger 3 (NCX3) gene leads to a worsening of ischemic brain damage. The Journal of neuroscience : the official journal of the Society for Neuroscience 28: 1179–1184 (2008).

132. Mühling, Tobias; Duda, Johanna; Weishaupt, Jochen H.; Ludolph, Albert C.; Liss, Birgit: Elevated mRNA-levels of distinct mitochondrial and plasma membrane Ca(2+) transporters in individual hypoglossal motor neurons of endstage SOD1 transgenic mice. Frontiers in cellular neuroscience 8: 353 (2014).

133. Murakami, Tetsuro; Nagai, Makiko; Miyazaki, Kazunori; Morimoto, Nobutoshi; Ohta, Yasuyuki; Kurata, Tomoko; Takehisa, Yasushi; Kamiya, Tatsushi; Abe, Koji: Early decrease of mitochondrial DNA repair enzymes in spinal motor neurons of presymptomatic transgenic mice carrying a mutant SOD1 gene. Brain research 1150: 182–189 (2007).

134. Nagai, Makiko; Re, Diane B.; Nagata, Tetsuya; Chalazonitis, Alcmène; Jessell, Thomas M.; Wichterle, Hynek; Przedborski, Serge: Astrocytes expressing ALS-linked mutated SOD1 release factors selectively toxic to motor neurons. Nature neuroscience 10: 615–622 (2007).

135. Neumann, Manuela; Igaz, Lionel M.; Kwong, Linda K.; Nakashima-Yasuda, Hanae; Kolb, Stephen J.; Dreyfuss, Gideon; Kretzschmar, Hans A.; Trojanowski, John Q.; Lee, Virginia M-Y: Absence of heterogeneous nuclear ribonucleoproteins and survival motor neuron protein in TDP-43 positive inclusions in frontotemporal lobar degeneration. Acta neuropathologica 113: 543–548 (2007).

136. Neumann, Manuela; Sampathu, Deepak M.; Kwong, Linda K.; Truax, Adam C.; Micsenyi, Matthew C.; Chou, Thomas T.; Bruce, Jennifer; Schuck, Theresa; Grossman, Murray; Clark, Christopher M.; McCluskey, Leo F.; Miller, Bruce L.; Masliah, Eliezer; Mackenzie, Ian R.; Feldman, Howard; Feiden, Wolfgang; Kretzschmar, Hans A.; Trojanowski, John Q.; Lee, Virginia M-Y: Ubiquitinated TDP-43 in frontotemporal lobar degeneration and amyotrophic lateral sclerosis. Science (New York, N.Y.) 314: 130–133 (2006).

137. Nimchinsky, E. A.; Young, W. G.; Yeung, G.; Shah, R. A.; Gordon, J. W.; Bloom, F. E.; Morrison, J. H.; Hof, P. R.: Differential vulnerability of oculomotor, facial, and hypoglossal nuclei in G86R superoxide dismutase transgenic mice. The Journal of comparative neurology 416: 112–125 (2000).

138. Noto, Yu-ichi; Misawa, Sonoko; Kanai, Kazuaki; Shibuya, Kazumoto; Isose, Sagiri; Nasu, Saiko; Sekiguchi, Yukari; Fujimaki, Yumi; Nakagawa, Masanori; Kuwabara, Satoshi: Awaji ALS criteria increase the diagnostic sensitivity in patients with bulbar onset. Clinical neurophysiology : official journal of the International Federation of Clinical Neurophysiology 123: 382–385 (2012).

139. Nowikovsky, K.; Pozzan, T.; Rizzuto, R.; Scorrano, L.; Bernardi, P.: Perspectives on: SGP Symposium on Mitochondrial Physiology and Medicine: The Pathophysiology of LETM1. The Journal of General Physiology 139: 445–454 (2012).

140. Nowikovsky, Karin; Froschauer, Elisabeth M.; Zsurka, Gabor; Samaj, Jozef; Reipert, Siegfried; Kolisek, Martin; Wiesenberger, Gerlinde; Schweyen, Rudolf J.: The LETM1/YOL027 gene family encodes a factor of the mitochondrial K+ homeostasis with a potential role in the Wolf-Hirschhorn syndrome. The Journal of biological chemistry 279: 30307–30315 (2004).

141. Ogawa, Mariko; Furukawa, Yoshiaki: A seeded propagation of Cu, Zn-superoxide dismutase aggregates in amyotrophic lateral sclerosis. Frontiers in cellular neuroscience 8: 83 (2014).

142. Oliveira, G. de; Alves, Chrystian J.; Chadi, Gerson: Early gene expression changes in spinal cord from SOD1(G93A) Amyotrophic Lateral Sclerosis animal model. Frontiers in cellular neuroscience 7: 216 (2013).

143. Palty, R.; Silverman, W. F.; Hershfinkel, M.; Caporale, T.; Sensi, S. L.; Parnis, J.; Nolte, C.; Fishman, D.; Shoshan-Barmatz, V.; Herrmann, S.; Khananshvili, D.; Sekler, I.: NCLX is an essential component of mitochondrial Na+/Ca2+ exchange. Proceedings of the National Academy of Sciences 107: 436–441 (2010).

144. Pan, Xin; Liu, Jie; Nguyen, Tiffany; Liu, Chengyu; Sun, Junhui; Teng, Yanjie; Fergusson, Maria M.; Rovira, Ilsa I.; Allen, Michele; Springer, Danielle A.; Aponte, Angel M.; Gucek, Marjan; Balaban, Robert S.; Murphy, Elizabeth; Finkel, Toren: The physiological role of mitochondrial calcium revealed by mice lacking the mitochondrial calcium uniporter. Nature cell biology 15: 1464–1472 (2013).

145. Parpura, Vladimir; Heneka, Michael T.; Montana, Vedrana; Oliet, Stéphane H R; Schousboe, Arne; Haydon, Philip G.; Stout, Randy F.; Spray, David C.; Reichenbach, Andreas; Pannicke, Thomas; Pekny, Milos; Pekna, Marcela; Zorec, Robert; Verkhratsky, Alexei: Glial cells in (patho)physiology. Journal of neurochemistry 121: 4–27 (2012).

146. Pedotti, Paola; 't Hoen, Peter A C; Vreugdenhil, Erno; Schenk, Geert J.; Vossen, Rolf Ham; Ariyurek, Yavuz; Hollander, Mattias de; Kuiper, Rowan; van Ommen, Gertjan J B; den Dunnen, Johan T; Boer, Judith M.; de Menezes, Renée X: Can subtle changes in gene expression be consistently detected with different microarray platforms? BMC Genomics 9: 124 (2008).

147. Peixoto, Pablo M.; Kim, Hyun-Jeong; Sider, Brittany; Starkov, Anatoly; Horvath, Tamas L.; Manfredi, Giovanni: UCP2 overexpression worsens mitochondrial dysfunction and accelerates disease progression in a mouse model of amyotrophic lateral sclerosis. Molecular and cellular neurosciences 57: 104–110 (2013).

148. Perocchi, Fabiana; Gohil, Vishal M.; Girgis, Hany S.; Bao, X. Robert; McCombs, Janet E.; Palmer, Amy E.; Mootha, Vamsi K.: MICU1 encodes a mitochondrial EF hand protein required for Ca2+ uptake. Nature 467: 291–296 (2010).

149. Perrin, Florence E.; Boisset, Gaelle; Docquier, Mylene; Schaad, Olivier; Descombes, Patrick; Kato, Ann C.: No widespread induction of cell death genes occurs in pure motoneurons in an amyotrophic lateral sclerosis mouse model. Human molecular genetics 14: 3309–3320 (2005).

150. Perrin, Florence E.; Boisset, Gaelle; Lathuilière, Aurélien; Kato, Ann C.: Cell death pathways differ in several mouse models with motoneurone disease: analysis of pure motoneurone populations at a presymptomatic age. Journal of neurochemistry 98: 1959–1972 (2006).

151. Philips, T.; Rothstein, J. D.: Glial cells in amyotrophic lateral sclerosis. Experimental Neurology 262 Pt B: 111–120 (2014).

152. Philipson, K. D.; Nicoll, D. A.: Sodium-calcium exchange: a molecular perspective. Annual review of physiology 62: 111–133 (2000).

153. Pignataro, Giuseppe; Boscia, Francesca; Esposito, Elga; Sirabella, Rossana; Cuomo, Ornella; Vinciguerra, Antonio; Di Renzo, Gianfranco; Annunziato, Lucio: NCX1 and NCX3: two new effectors of delayed preconditioning in brain ischemia. Neurobiology of disease 45: 616–623 (2012).

154. Pramatarova, A.; Laganière, J.; Roussel, J.; Brisebois, K.; Rouleau, G. A.: Neuron-specific expression of mutant superoxide dismutase 1 in transgenic mice does not lead to motor impairment. The Journal of neuroscience : the official journal of the Society for Neuroscience 21: 3369–3374 (2001).

155. Puri, Sapna; Hebrok, Matthias: Diabetic β Cells: To Be or Not To Be? Cell 150: 1103–1104 (2012).

156. Qiang, Liang; Fujita, Ryousuke; Abeliovich, Asa: Remodeling neurodegeneration: somatic cell reprogramming-based models of adult neurological disorders. Neuron 78: 957–969 (2013).

157. Ramirez, Alfredo; Heimbach, André; Gründemann, Jan; Stiller, Barbara; Hampshire, Dan; Cid, L. Pablo; Goebel, Ingrid; Mubaidin, Ammar F.; Wriekat, Abdul-Latif; Roeper, Jochen; Al-Din, Amir; Hillmer, Axel M.; Karsak, Meliha; Liss, Birgit; Woods, C. Geoffrey; Behrens, Maria I.; Kubisch, Christian: Hereditary parkinsonism with dementia is caused by mutations in ATP13A2, encoding a lysosomal type 5 P-type ATPase. Nature genetics 38: 1184–1191 (2006).

158. Redler, Rachel L.; Dokholyan, Nikolay V. (2012): The Complex Molecular Biology of Amyotrophic Lateral Sclerosis (ALS). In : Molecular Biology of Neurodegenerative Diseases, vol. 107: Elsevier (Progress in Molecular Biology and Translational Science): 215–262.

159. Renton, Alan E.; Chiò, Adriano; Traynor, Bryan J.: State of play in amyotrophic lateral sclerosis genetics. Nature Neuroscience 17: 17–23 (2013).

160. Renton, Alan E.; Majounie, Elisa; Waite, Adrian; Simón-Sánchez, Javier; Rollinson, Sara; Gibbs, J. Raphael; Schymick, Jennifer C.; Laaksovirta, Hannu; van Swieten, John C; Myllykangas, Liisa; Kalimo, Hannu; Paetau, Anders; Abramzon, Yevgeniya; Remes, Anne M.; Kaganovich, Alice; Scholz, Sonja W.; Duckworth, Jamie; Ding, Jinhui; Harmer, Daniel W.; Hernandez, Dena G.; Johnson, Janel O.;

Mok, Kin; Ryten, Mina; Trabzuni, Danyah; Guerreiro, Rita J.; Orrell, Richard W.; Neal, James; Murray, Alex; Pearson, Justin; Jansen, Iris E.; Sondervan, David; Seelaar, Harro; Blake, Derek; Young, Kate; Halliwell, Nicola; Callister, Janis Bennion; Toulson, Greg; Richardson, Anna; Gerhard, Alex; Snowden, Julie; Mann, David; Neary, David; Nalls, Michael A.; Peuralinna, Terhi; Jansson, Lilja; Isoviita, Veli-Matti; Kaivorinne, Anna-Lotta; Hölttä-Vuori, Maarit; Ikonen, Elina; Sulkava, Raimo; Benatar, Michael; Wuu, Joanne; Chiò, Adriano; Restagno, Gabriella; Borghero, Giuseppe; Sabatelli, Mario; Heckerman, David; Rogaeva, Ekaterina; Zinman, Lorne; Rothstein, Jeffrey D.; Sendtner, Michael; Drepper, Carsten; Eichler, Evan E.; Alkan, Can; Abdullaev, Ziedulla; Pack, Svetlana D.; Dutra, Amalia; Pak, Evgenia; Hardy, John; Singleton, Andrew; Williams, Nigel M.; Heutink, Peter; Pickering-Brown, Stuart; Morris, Huw R.; Tienari, Pentti J.; Traynor, Bryan J.: A hexanucleotide repeat expansion in C9ORF72 is the cause of chromosome 9p21-linked ALS-FTD. Neuron 72: 257–268 (2011).

161. Rizzuto, R.; Pinton, P.; Carrington, W.; Fay, F. S.; Fogarty, K. E.; Lifshitz, L. M.; Tuft, R. A.; Pozzan, T.: Close contacts with the endoplasmic reticulum as determinants of mitochondrial Ca2+ responses. Science (New York, N.Y.) 280: 1763–1766 (1998).

162. Rizzuto, Rosario; Pozzan, Tullio: Microdomains of intracellular Ca2+: molecular determinants and functional consequences. Physiological reviews 86: 369–408 (2006).

163. Robberecht, Wim; Philips, Thomas: The changing scene of amyotrophic lateral sclerosis. Nature reviews. Neuroscience 14: 248–264 (2013).

164. Rosen, D. R.; Siddique, T.; Patterson, D.; Figlewicz, D. A.; Sapp, P.; Hentati, A.; Donaldson, D.; Goto, J.; O'Regan, J. P.; Deng, H. X.: Mutations in Cu/Zn superoxide dismutase gene are associated with familial amyotrophic lateral sclerosis. Nature 362: 59–62 (1993).

165. Rothstein, J. D.; Dykes-Hoberg, M.; Pardo, C. A.; Bristol, L. A.; Jin, L.; Kuncl, R. W.; Kanai, Y.; Hediger, M. A.; Wang, Y.; Schielke, J. P.; Welty, D. F.: Knockout of glutamate transporters reveals a major role for astroglial transport in excitotoxicity and clearance of glutamate. Neuron 16: 675–686 (1996).

166. Rothstein, J. D.; Martin, L. J.; Kuncl, R. W.: Decreased glutamate transport by the brain and spinal cord in amyotrophic lateral sclerosis. The New England journal of medicine 326: 1464–1468 (1992).

167. Rotunno, Melissa S.; Bosco, Daryl A.: An emerging role for misfolded wild-type SOD1 in sporadic ALS pathogenesis. Frontiers in Cellular Neuroscience 7 (2013).

168. Sarthy, P. V.; Fu, M.; Huang, J.: Developmental expression of the glial fibrillary acidic protein (GFAP) gene in the mouse retina. Cellular and molecular neurobiology 11: 623–637 (1991).

169. Schiemann, Julia; Schlaudraff, Falk; Klose, Verena; Bingmer, Markus; Seino, Susumu; Magill, Peter J.; Zaghloul, Kareem A.; Schneider, Gaby; Liss, Birgit; Roeper, Jochen: K-ATP channels in dopamine substantia nigra neurons control bursting and novelty-induced exploration. Nature neuroscience 15: 1272–1280 (2012).

170. Schlaudraff, Falk; Gründemann, Jan; Fauler, Michael; Dragicevic, Elena; Hardy, John; Liss, Birgit: Orchestrated increase of dopamine and PARK mRNAs but

not miR-133b in dopamine neurons in Parkinson's disease. Neurobiology of aging 35: 2302–2315 (2014).

171. Sharma, Vishal; O'Halloran, Damien M.: Recent structural and functional insights into the family of sodium calcium exchangers. genesis 52: 93–109 (2014).

172. Shaw, P. J.; Eggett, C. J.: Molecular factors underlying selective vulnerability of motor neurons to neurodegeneration in amyotrophic lateral sclerosis. Journal of neurology 247 Suppl 1: I17-27 (2000).

173. Shibata, N.: Transgenic mouse model for familial amyotrophic lateral sclerosis with superoxide dismutase-1 mutation. Neuropathology : official journal of the Japanese Society of Neuropathology 21: 82–92 (2001).

174. Solomon, Jesse A.; Tarnopolsky, Mark A.; Hamadeh, Mazen J.; Dawson, Ted M.: One Universal Common Endpoint in Mouse Models of Amyotrophic Lateral Sclerosis. PLoS ONE 6: e20582 (2011).

175. Stefani, Diego de; Raffaello, Anna; Teardo, Enrico; Szabò, Ildikò; Rizzuto, Rosario: A forty-kilodalton protein of the inner membrane is the mitochondrial calcium uniporter. Nature 476: 336–340 (2011).

176. Strehler, Emanuel E.: Plasma membrane calcium ATPases as novel candidates for therapeutic agent development. Journal of pharmacy & pharmaceutical sciences : a publication of the Canadian Society for Pharmaceutical Sciences, Société canadienne des sciences pharmaceutiques 16: 190–206 (2013).

177. Tadic, Vedrana; Prell, Tino; Lautenschlaeger, Janin; Grosskreutz, Julian: The ER mitochondria calcium cycle and ER stress response as therapeutic targets in amyotrophic lateral sclerosis. Frontiers in cellular neuroscience 8: 147 (2014).

178. Taylor, Sean C.; Mrkusich, Eli M.: The state of RT-quantitative PCR: firsthand observations of implementation of minimum information for the publication of quantitative real-time PCR experiments (MIQE). Journal of molecular microbiology and biotechnology 24: 46–52 (2014).

179. Trenker, Michael; Malli, Roland; Fertschai, Ismene; Levak-Frank, Sanja; Graier, Wolfgang F.: Uncoupling proteins 2 and 3 are fundamental for mitochondrial Ca2+ uniport. Nature Cell Biology 9: 445–452 (2007).

180. Trias, Emiliano; Díaz-Amarilla, Pablo; Olivera-Bravo, Silvia; Isasi, Eugenia; Drechsel, Derek A.; Lopez, Nathan; Bradford, C. Samuel; Ireton, Kyle E.; Beckman, Joseph S.; Barbeito, Luis: Phenotypic transition of microglia into astrocyte-like cells associated with disease onset in a model of inherited ALS. Frontiers in cellular neuroscience 7: 274 (2013).

181. Tsai, Ming-Feng; Jiang, Dawei; Zhao, Linlin; Clapham, David; Miller, Christopher: Functional reconstitution of the mitochondrial Ca2+/H+ antiporter Letm1. The Journal of general physiology 143: 67–73 (2014).

182. Turner, Bradley J.; Talbot, Kevin: Transgenics, toxicity and therapeutics in rodent models of mutant SOD1-mediated familial ALS. Progress in neurobiology 85: 94–134 (2008).

183. Turner, Martin R.; Hardiman, Orla; Benatar, Michael; Brooks, Benjamin R.; Chio, Adriano; Carvalho, Mamede de; Ince, Paul G.; Lin, Cindy; Miller, Robert G.; Mitsumoto, Hiroshi; Nicholson, Garth; Ravits, John; Shaw, Pamela J.; Swash, Michael; Talbot, Kevin; Traynor, Bryan J.; van den Berg, Leonard H; Veldink, Jan H.;

Vucic, Steve; Kiernan, Matthew C.: Controversies and priorities in amyotrophic lateral sclerosis. The Lancet Neurology 12: 310–322 (2013).

184. Ukabam, C. U.: A Golgi-Cox study of the hypoglossal nucleus of 'wobbler' and normal mice. La Ricerca in clinica e in laboratorio 18: 313–318 (1988).

185. Valori, Chiara F.; Brambilla, Liliana; Martorana, Francesca; Rossi, Daniela: The multifaceted role of glial cells in amyotrophic lateral sclerosis. Cellular and molecular life sciences : CMLS 71: 287–297 (2014).

186. van Brederode, J.; Yanagawa, Y.; Berger, A. J.: GAD67-GFP+ Neurons in the Nucleus of Roller: A Possible Source of Inhibitory Input to Hypoglossal Motoneurons. I. Morphology and Firing Properties. Journal of Neurophysiology 105: 235–248 (2011).

187. van Den Bosch, L.; Schwaller, B.; Vleminckx, V.; Meijers, B.; Stork, S.; Ruehlicke, T.; van Houtte, E.; Klaassen, H.; Celio, M. R.; Missiaen, L.; Robberecht, W.; Berchtold, M. W.: Protective effect of parvalbumin on excitotoxic motor neuron death. Experimental neurology 174: 150–161 (2002).

188. Vance, Caroline; Rogelj, Boris; Hortobágyi, Tibor; De Vos, Kurt J; Nishimura, Agnes Lumi; Sreedharan, Jemeen; Hu, Xun; Smith, Bradley; Ruddy, Deborah; Wright, Paul; Ganesalingam, Jeban; Williams, Kelly L.; Tripathi, Vineeta; Al-Saraj, Safa; Al-Chalabi, Ammar; Leigh, P. Nigel; Blair, Ian P.; Nicholson, Garth; Belleroche, Jackie de; Gallo, Jean-Marc; Miller, Christopher C.; Shaw, Christopher E.: Mutations in FUS, an RNA processing protein, cause familial amyotrophic lateral sclerosis type 6. Science (New York, N.Y.) 323: 1208–1211 (2009).

189. Vangheluwe, Peter; Raeymaekers, Luc; Dode, Leonard; Wuytack, Frank: Modulating sarco(endo)plasmic reticulum Ca2+ ATPase 2 (SERCA2) activity: cell biological implications. Cell Calcium 38: 291–302 (2005).

190. Vanselow, Bodo K.; Keller, Bernhard U.: Calcium dynamics and buffering in oculomotor neurones from mouse that are particularly resistant during amyotrophic lateral sclerosis (ALS)-related motoneurone disease. The Journal of Physiology 525: 433–445 (2000).

191. Vehviläinen, Piia; Koistinaho, Jari; Gundars, Goldsteins: Mechanisms of mutant SOD1 induced mitochondrial toxicity in amyotrophic lateral sclerosis. Frontiers in cellular neuroscience 8: 126 (2014).

192. Verkhratsky, A.: Physiology and Pathophysiology of the Calcium Store in the Endoplasmic Reticulum of Neurons. Physiological Reviews 85: 201–279 (2005).

193. Vucic, Steve; Rothstein, Jeffrey D.; Kiernan, Matthew C.: Advances in treating amyotrophic lateral sclerosis: insights from pathophysiological studies. Trends in Neurosciences 37: 433–442 (2014).

194. Waldeck-Weiermair, M.; Jean-Quartier, C.; Rost, R.; Khan, M. J.; Vishnu, N.; Bondarenko, A. I.; Imamura, H.; Malli, R.; Graier, W. F.: Leucine Zipper EF Hand-containing Transmembrane Protein 1 (Letm1) and Uncoupling Proteins 2 and 3 (UCP2/3) Contribute to Two Distinct Mitochondrial Ca2+ Uptake Pathways. Journal of Biological Chemistry 286: 28444–28455 (2011).

195. Waldeck-Weiermair, Markus; Duan, Xiumei; Naghdi, Shamim; Khan, Muhammad Jadoon; Trenker, Michael; Malli, Roland; Graier, Wolfgang F.: Uncoupling protein 3 adjusts mitochondrial Ca(2+) uptake to high and low Ca(2+) signals. Cell Calcium 48: 288–301 (2010).

196. Wiederkehr, Andreas; Szanda, Gergo; Akhmedov, Dmitry; Mataki, Chikage; Heizmann, Claus W.; Schoonjans, Kristina; Pozzan, Tullio; Spät, András; Wollheim, Claes B.: Mitochondrial matrix calcium is an activating signal for hormone secretion. Cell metabolism 13: 601–611 (2011).

197. Wong, Margaret; Martin, Lee J.: Skeletal muscle-restricted expression of human SOD1 causes motor neuron degeneration in transgenic mice. Human molecular genetics 19: 2284–2302 (2010).

198. Xu, Lin; Renaud, Ludivine; Müller, Joachim G.; Baicu, Catalin F.; Bonnema, D. Dirk; Zhou, Hongming; Kappler, Christiana S.; Kubalak, Steven W.; Zile, Michael R.; Conway, Simon J.; Menick, Donald R.: Regulation of Ncx1 expression. Identification of regulatory elements mediating cardiac-specific expression and up-regulation. The Journal of biological chemistry 281: 34430–34440 (2006).

199. Yamamoto, Masahiko; Tanaka, Fumiaki; Sobue, Gen: [Gene expression profile of spinal ventral horn in ALS]. Brain and nerve = Shinkei kenkyū no shinpo 59: 1129–1139 (2007).

200. Yamanaka, Koji; Chun, Seung Joo; Boillee, Severine; Fujimori-Tonou, Noriko; Yamashita, Hirofumi; Gutmann, David H.; Takahashi, Ryosuke; Misawa, Hidemi; Cleveland, Don W.: Astrocytes as determinants of disease progression in inherited amyotrophic lateral sclerosis. Nature neuroscience 11: 251–253 (2008).

201. Yasuda, Kouichi; Nakayama, Yoko; Tanaka, Mizuho; Tanaka, Mikiko; Mori, Ryota; Furusawa, Kiyofumi: The distribution of respiration-related and swallowing-related motoneurons innervating the rat genioglossus muscle. Somatosensory & Motor Research 19: 30–35 (2002).

202. Zang, D. W.; Cheema, S. S.: Degeneration of corticospinal and bulbospinal systems in the superoxide dismutase 1(G93A G1H) transgenic mouse model of familial amyotrophic lateral sclerosis. Neuroscience letters 332: 99–102 (2002).

203. Zhao, Weihua; Xie, Wenjie; Le, Weidong; Beers, David R.; He, Yi; Henkel, Jenny S.; Simpson, Ericka P.; Yen, Albert A.; Xiao, Qin; Appel, Stanley H.: Activated microglia initiate motor neuron injury by a nitric oxide and glutamate-mediated mechanism. Journal of neuropathology and experimental neurology 63: 964–977 (2004).

Appendix

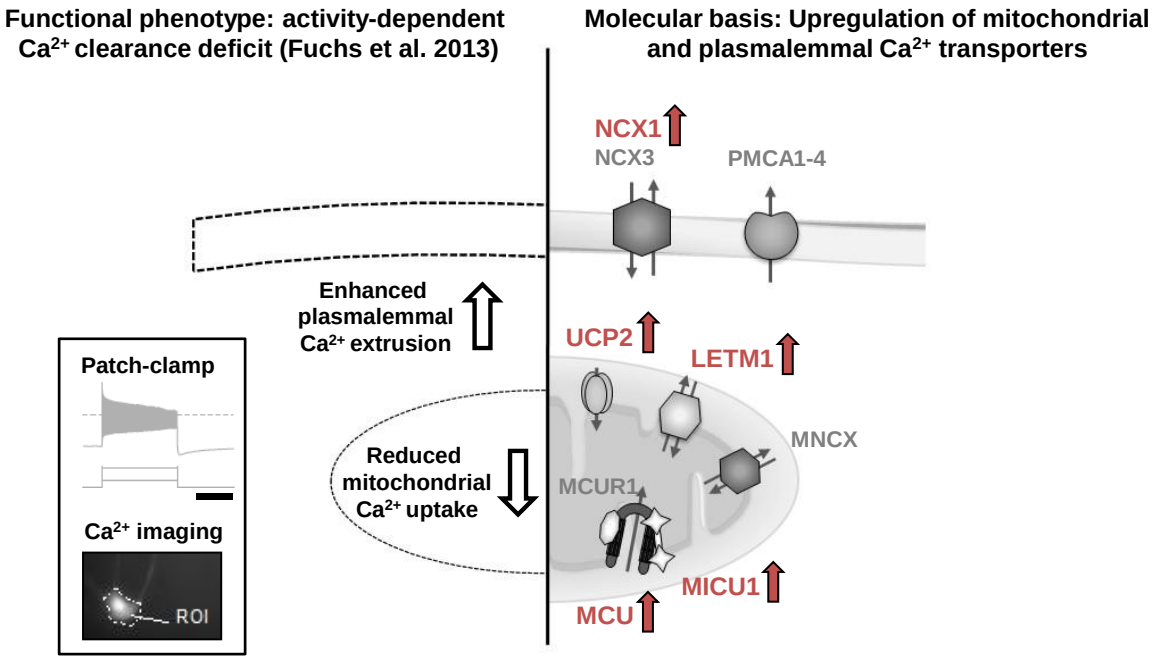

Appendix, Figure 1: Overview of functional and molecular alterations in calcium (Ca^{2+}) clearance of hypoglossal motor neurons (hMNs).
Right: Overview of concerted elevated Ca^{2+} transporter expression in individual hMNs from $SOD1^{G93A}$ mice compared to wildtype (WT) (marked in red: MCU/MICU1, LETM1, UCP2 and NCX1). Left: These findings can provide a molecular basis for the recently described, selective functional, activity-dependent Ca^{2+} homeostasis deficit in hMNs from endstage $SOD1^{G93A}$ mice. Insert shows stimulation protocol and resulting electrophysiological recordings (scale bar: 1s), combined with Ca^{2+} imaging (electrophysiologic stimulation protocol kindly provided by A. Fuchs). UCP: Uncoupling protein, LETM1: Leucine zipper EF hand-containing transmembrane protein 1, MNCX: Mitochondrial sodium-Ca^{2+} exchanger, MCU: Mitochondrial Ca^{2+} uniporter, MICU1: Mitochondrial Ca^{2+} uptake 1, MCUR1: Mitochondrial Ca^{2+} uniporter regulator 1, PMCA: plasmalemmal Ca^{2+} ATPase, NCX: plasmalemmal Na^{+}/Ca^{2+} exchanger

Appendix, Table 1: Studies on gene expression in amyotrophic lateral sclerosis (ALS) patients or animal models using UV-laser microdissection.
Given are the year of publication, first author, specimen characteristics (human or animal tissue, respective animal model, number of samples), examined time points with their cllinical significance, brain regions, tissue preparation and staining methods, performed type of expression analysis and normalization genes. ALDH1L1: aldehyde dehydrogenase 1 family, member L1, DAB: 3,3'-Diaminobenzidine, GAPDH: glyceraldehyde-3-phosphat-dehydrogenase, HE: hematoxylin-eosin, HSPB8: heat shock protein beta 8, NME1: nucleoside diphosphate kinase A, RPS9: ribosomal protein S9, VEGF: vascular endothelial growth factor, sALS: sporadic amyotrophic lateral sclerosis, fALS: familial amyotrophic lateral sclerosis, qPCR: quantitative polymerase chain reaction, ChAT: choline acetyltransferase, mtDNA: mitochondrial DNA

Date	Author	Human / animal	Time points	Brain region	Tissue specifications / staining	Expression Analysis
2003	**Mawrin et al.**	7 sALS patients, 3 controls	n.a.	spinal cord	5µm paraffin sections, HE	mtDNA common deletion
2004	**Mawrin et al.**	7 sALS patients, 7 controls	n.a.	motor cortex hypoglossal nucleus spinal cord	5µm paraffin sections, HE	mtDNA common deletion
2005	**Jiang et al.**	14 sALS patients, 13 controls	n.a.	spinal cord	10µm sections, hematoxylin MN identification via ChAT PCR	Microarray confirmation via qPCR
2005	**Perrin et al.**	$SOD1^{G93A}$ mice	60 days (pre) 90 days (onset) 120 days (endstage)	spinal cord	16µm sections, methylene blue MN identification via diameter (>25 µm)	Microarray confirmation via qPCR normalization to GAPDH/RPS9
2006	**Perrin et al.**	Wobbler mice	12 days (pre) 61 days (endstage)	spinal cord	16µm sections, methylene blue MN identification via diameter (>25 µm) and identifiable nucleus	Microarray confirmation via qPCR normalization to GAPDH/RPS9
2007	**Ferraiuolo et al.**	$SOD1^{G93A}$ mice	60 days (pre) 90 days (onset) 120 days (endstage)	spinal cord	10µm sections, toluidine blue	Microarray confirmation via qPCR normalization to GAPDH
2007	**Yamamoto et al.**	sALS patients	n.a.	spinal cord	[Full text in japanese only]	
2007	**Lobsiger et al.**	$SOD1^{G85R}$, $SOD1^{G37R}$, $SOD1^{WT(hu)}$ mice	(G37R) 8 weeks (pre) 15 weeks (onset)	spinal cord	20µm sections, cresyl violet MN identification via diameter (> 25µm)	Microarray
2010	**Brockington et al.**	$VEGF^{\delta/\delta}$ mice	3 months (pre) 5 months (onset) 14 months (endstage)	spinal cord	10µm sections, toluidine blue MN identification via size, location, morphology	Microarray confirmation via qPCR normalization to ß-actin, HspB8, Nme1
2010	**Hedlund et al.**	$SOD1^{G93A}$ rats	60 days (pre)	oculomotor nucleus hypoglossal nucleus spinal cord	12µm sections Anti-ChAT (MN marker)	Microarray confirmation via qPCR
2011	**Ferraiuolo et al.**	$SOD1^{G93A}$ mice $SOD1^{WT(OE)}$ mice	60 days (pre)	spinal cord **Astrocytes**	10µm sections, DAB, Anti-ALDH1L1 (astrocyte marker)	Microarray confirmation via qPCR
2013	**Oliveira et al.**	$SOD1^{G93A}$ mice	40 days (pre) 80 days (late pre)	spinal cord **Astrocytes**	5µm sections, Anti-GFAP (astrocyte marker)	Microarray confirmation via qPCR normalization to GAPDH
2014	**Maximino et al.**	$SOD1^{G93A}$ mice	40 days (pre) 80 days (late pre)	Spinal cord	5µm sections, Anti-ChAT (MN marker)	Microarray confirmation via qPCR normalization to GAPDH

List of Figures

Figure 1: The human pyramidal motor system is crucial for movement initiation and control. 2
Figure 2: Proposed pathogenic mechanisms of misfolded superoxide dismutase 1 (SOD1). 6
Figure 3: Overview on proposed converging pathophysiological mechanisms underlying neurodegeneration in amyotrophic lateral sclerosis. 9
Figure 4: Amyotrophic lateral sclerosis associated mechanisms of mitochondrial dysfunction: 11
Figure 5: Illustration of calcium (Ca^{2+}) transporter proteins for plasmalemmal, mitochondrial, and endoplasmic reticulum Ca^{2+} transport in motor neurons, that shape cytosolic Ca^{2+} after entry through glutamate receptors and voltage dependent Ca^{2+} channels (not shown). 16
Figure 6: Hypoglossal motor neurons (hMNs) from endstage $SOD1^{G93A}$ mice display activity dependent reduced cytosolic calcium (Ca^{2+}) clearance due to impaired mitochondrial Ca^{2+} buffering capacity. 23
Figure 7: Preparation of tissue blocks containing hypoglossal nucleus. 36
Figure 8: Cryotome and murine brain tissue fixed on cryostat holder. 37
Figure 9: Leica LMD7000 microscope used for UV-laser microdissection. 38
Figure 10: User-mask of the Laser Microdissection (LMD) software with the respective menu bars. 39
Figure 11: Beer's law. 42
Figure 12: Analysis of RNA integrity number (RIN) via Agilent Bioanalyzer 2100. 44
Figure 13: Agarose gel (2%) electrophoresis of genotyping-PCR products for murine tail tissue of wildtype (WT) and $SOD1^{G93A}$ transgenic animals. 51
Figure 14: Four phases of a a quantitiative PCR reaction. 53
Figure 15: Principles of TaqMan PCR. 54
Figure 16: Overview of Applied Biosystems SDS 2.3 software for realtime quantitative PCR data aquisition. 56
Figure 17: Formula for calculation of assay efficiency. 57
Figure 18: Formula for calculation of cDNA amounts based on obtained C_t-value and standard curve parameters from quantitative PCR results. 58
Figure 19: TaqMan realtime quantitative PCR of serial dilutions from 37.5 to 37500 pg of murine wildtype (WT) brainstem standard cDNA for performance test of the

TaqMan assays for an exemplary mitochondrial (MICU1), plasmalemmal (PMCA3) and normalization gene (ND1). 62
Figure 20: Mouse brainstem histology of the hypoglossal nucleus and illustration of UV laser microdissection (UV-LMD) of its motor neurons. 66
Figure 21: Estimated sizes of hypoglossal motor neurons (hMNs) from wildtype (WT) and SOD1^{G93A} transgenic animals analyzed via realtime quantitative PCR (RT-qPCR) in this study. 67
Figure 22: Evaluation of NADH dehydrogenase subunit 1 (ND1) and choline-acetyltransferase (ChAT) expression, used for normalization of cell-specific realtime quantitative PCR (RT-qPCR) data. 69
Figure 23: Evaluation of glial fibrillary acidic protein (GFAP) and glutamate decarboxylase (GAD) 65/67 in choline acetyltransferase (ChAT) positive hypoglossal motor neurons (hMNs) in SOD1^{G93A} transgenic and wildtype (WT) mice via multiplex-nested-PCR. 71
Figure 24: Evaluation of glial fibrillary acidic protein (GFAP) in choline acetyltransferase (ChAT) positive hypoglossal motor neurons (hMNs) in SOD1^{G93A} transgenic and wildtype (WT) mice via realtime quantitative PCR (RT-qPCR) (A) and influence of GFAP co-expression on expression levels of mitochondrial calcium uniporter (mCU) subunits mitochondrial calcium uniporter (MCU) and mitochondrial calcium uptake 1 (MICU1). 72
Figure 25: Expression of putative mitochondrial (left) and plasma membrane (right) calcium (Ca^{2+}) transporters in brainstem tissue derived cDNA (upper) as well as choline acetyltransferase (ChAT) and NADH dehydrogenase subunit 1 (ND1) positive hypoglossal motor neurons (hMNs) (lower). 74
Figure 26: Realtime quantitative (RT-qPCR) data of mitochondrial Ca^{2+} transporters mitochondrial calcium uniporter (MCU) and mitochondrial calcium uptake 1 (MICU1) (2011 dataset). 75
Figure 27: Realtime quantitative PCR data of mitochondrial calcium (Ca^{2+}) transporters in hypoglossal motor neurons of wildtype (WT, white) and SOD1^{G93A} (red) mice. 77
Figure 28: Realtime quantitative PCR data of plasma membrane calcium (Ca^{2+}) transporters in hypoglossal motor neurons of wildtype (WT, white) and SOD1^{G93A} (red) mice. 79

List of Tables

Table 1: Genes identified to carry amyotrophic lateral sclerosis (ALS) causing mutations, with their chromosomal location, inheritance, frequency among ALS patients and known function. 5
Table 2: List of used instruments and technical equipment. 26
Table 3: List of used software. 27
Table 4: List of used reagents and stock concentrations. 28
Table 5: List of used laboratory consumables. 29
Table 6: List of used master mixes and Kits. 30
Table 7: List of used mouse primers for qualitative multiplex- and nested-PCRs. 31
Table 8: Mouse primers for PCR-based genotyping of wildtype (SOD1 wildtype) and mutated ($SOD1^{G93A}$) SOD1 mice. 32
Table 9: Mouse TaqMan quantitative PCR assays that were used in this work for quantificaton of calcium (Ca^{2+}) transporter as well as marker genes. 33
Table 10: Laser control settings of the LMD7000 software for UV-LMD of individual hMNs used and held constant throughout the whole series of experiments. 40
Table 11: Reaction mix for cDNA synthesis of isolated total brainstem RNA. 40
Table 12: Combined lysis and cDNA synthesis mix 41
Table 13: Precipitation master mix components. 42
Table 14: Components for freshly prepared Lysis-Buffer of murine tail/ear tissue. 47
Table 15: Genotyping-PCR-Mix components. 47
Table 16: Genotyping-PCR cycling parameters. 48
Table 17: Multiplex-PCR-reaction components 49
Table 18: Multiplex-PCR conditions. 49
Table 19: Nested-PCR-Mix components 50
Table 20: Nested-PCR conditions. 50
Table 21: TaqMan PCR-Mix reaction components. 55
Table 22: TaqMan PCR conditions. 55
Table 23: Information on mouse TaqMan quantitative PCR assays that were used in this work for quantificaton of calcium (Ca^{2+}) transporter as well as marker genes. 63
Table 24: Informations about all individual $SOD1^{G93A}$ and wildtype (WT) mice of which hypoglossal motor neurons were analyzed within this study. 65

Table 25: Estimated sizes of hypoglossal motor neurons (hMNs) from wildtype (WT) and SOD1^{G93A} transgenic animals analyzed via realtime quantitative PCR in this study. 67
Table 26: Summarized expression levels and statistical analysis for marker genes choline acetyltransferase (ChAT) and NADH dehydrogenase subunit 1 (ND1). 70
Table 27: Summarized mRNA expression levels and statistical analysis for glial fibrillary acidic protein (GFAP). 73
Table 28: Expression of mitochondrial calcium uniporter (MCU) and mitochondrial calcium uptake 1 (MICU1) in glial fibrillary acidic protein (GFAP) positive (+) and negative (-) pools (2011 dataset). 73
Table 29: Summarized mRNA expression levels and statistical analysis for mitochondrial calcium uniporter (MCU) and mitochondrial calcium uptake 1 (MICU1) according to 2011 dataset. 75
Table 30: Summarized realtime quantitative PCR results and statistical analysis for expression profiling of mitochondrial and plasmalemmal calcium (Ca^{2+}) transporters in hypoglossal motor neurons (hMNs) from wildtype (WT) and SOD1^{G93A} mice. 80

Acknowledgements

Vielen Dank...

... **Prof. Birgit Liss**, anspruchsvoll und teilweise mit unerbittlicher Akribie, aber wenn es drauf ankam menschlich, fair und vor allem motivierend. Vielen Dank dass ich bei/von Ihnen lernen durfte. Dass Sie mich vollwertig mit aller Verantwortung und allen Möglichkeiten in Ihr Team eingebunden haben, hat mir viel bedeutet und mir ein ungeahnt tiefes Verständnis für Wissenschaft und Forschung eröffnet.

... **Johanna Duda** für die jahrelange selbstlose, geduldige und immer wieder aufbauende Betreuung und die unermüdliche Hilfe, vor allem auf der Zielgeraden. Ich wünsche allen Doktoranden eine Betreuerin wie Dich.

... dem restlichen (teils ehemaligen) AG-Liss-Team: **Elena Dragicevic, Andrea Holler, Michael Fauler, Christina Pötschke** für die netten Gespräche zwischendurch und die allgemeine Unterstützung und ganz besonders **Stefanie Schulz** und **Desiree Spaich** für den tollen Einsatz und die Hilfe bei technischen Problemen aller Art. Außerdem Dank an **Julia Benkert** fürs Korrekturlesen.

... unseren Kooperationspartnern **Prof. Ludolph** und **Prof. Weishaupt** für die Hilfe insbesondere bei der Bereitstellung der Ulmer Tier-Kohorte. **Tanja Wipp** für die freundliche technische Unterstützung.

... **Andrea Fuchs** für die Einführung in das interessante Thema und die schnelle und freundliche Hilfe und Beantwortung von Fragen.

... meinen **lieben Eltern**, die mir Studium und Doktorarbeit (inkl. Freisemester) ermöglicht, mich in den schwierigen Zeiten bestärkt und mir in meinen Entscheidungen immer vertraut haben.

... **Hanni,** dafür dass Du diesen langen Weg mit mir gegangen bist und mir alle Freiräume gelassen hast, die ich für dieses Projekt gebraucht habe. Das hat die verbliebene Zeit mit Dir umso schöner und intensiver gemacht.

Curriculum vitae

Personal details

Name and surname:	Tobias Mühling
Adress:	Landfriedstraße 9
	81547 München
Date/place of birth:	28th of September 1985, Schrobenhausen
Nationality:	German

Education

1992 - 1995	Grundschule Lochham
1995 - 2004	Kurt-Huber-Gymnasium Gräfelfing
2004 - 2005	Civilian service, Privatklinik Fritz Wolfart, Gräfelfing
2005 - 2006	Rettungsdienstschule München
2006 - 2007	Medical University of Innsbruck
2007 - 2013	Medical faculty of Ulm University
2011 - 2015	Doctoral researcher, Institute of Applied Physiology, Ulm University
2013 - 2014	Medical faculty of University of Marburg Internship at Städtisches Klinikum Kassel
May 2014	Second part of German medical exam, Grade: 1.16

Parts of this thesis have found their way into the following publications:

Conferences:

Poster Presentation at the Neuroscience meeting (SfN) 2012, New Orleans (USA), Title: Selective mitochondrial Ca^{2+} uptake deficit in vulnerable hypoglossal motoneurons of endstage SOD1 ALS mice (**Mühling, Tobias**, Fuchs, Andrea; Duda, Johanna; Roeper, Jochen; Liss, Birgit)

Publications:

(*equally contributing authors)

Fuchs, Andrea; Kutterer, Sylvie; **Mühling, Tobias**; Duda, Johanna; Schütz, Burkhard; Liss, Birgit; Keller, Bernhard U.; Roeper, Jochen: Selective mitochondrial Ca 2+ uptake deficit in disease endstage vulnerable motoneurons of the SOD1 G93A mouse model of amyotrophic lateral sclerosis. The Journal of Physiology 591, pp. 2723–2745 (2013).

Mühling, Tobias*; Duda, Johanna*; Weishaupt, Jochen H.; Ludolph, Albert C.; Liss, Birgit: Elevated mRNA-levels of distinct mitochondrial and plasma membrane Ca(2+) transporters in individual hypoglossal motor neurons of endstage SOD1 transgenic mice. Frontiers in cellular neuroscience 8, p. 353 (2014).